JAERI-Research
96-040

HETC-3STEP CALCULATIONS OF PROTON INDUCED NUCLIDE PRODUCTION CROSS SECTIONS AT INCIDENT ENERGIES BETWEEN 20 MEV AND 5 GEV

August 1996

Hiroshi TAKADA, Nobuaki YOSHIZAWA* and Kenji ISHIBASHI**

日本原子力研究所
Japan Atomic Energy Research Institute

本レポートは，日本原子力研究所が不定期に公刊している研究報告書です。
入手の問合わせは，日本原子力研究所研究情報部研究情報課（〒319-11 茨城県那珂郡東海村）あて，お申し越しください。なお，このほかに財団法人原子力弘済会資料センター（〒319-11 茨城県那珂郡東海村日本原子力研究所内）で複写による実費頒布をおこなっております。

This report is issued irregularly.
Inquiries about availability of the reports should be addressed to Research Information Division, Department of Intellectual Resources, Japan Atomic Energy Research Institute, Tokai-mura, Naka-gun, Ibaraki-ken, 319-11, Japan.

© Japan Atomic Energy Research Institute, 1996

編集兼発行　日本原子力研究所
印　　刷　いばらき印刷㈱

JAERI-Research 96-040

HETC-3STEP Calculations of Proton Induced Nuclide Production Cross Sections at Incident Energies between 20 MeV and 5 GeV

Hiroshi TAKADA, Nobuaki YOSHIZAWA* and Kenji ISHIBASHI**

Department of Reactor Engineering
Tokai Research Establishment
Japan Atomic Energy Research Institute
Tokai-mura, Naka-gun, Ibaraki-ken

(Received July 1, 1996)

For the OECD/NEA code intercomparison, nuclide production cross sections of ^{16}O, ^{27}Al, ^{nat}Fe, ^{59}Co, ^{nat}Zr and ^{197}Au for the proton incidence with energies of 20 MeV to 5 GeV are calculated with the HETC-3STEP code based on the intranuclear cascade evaporation model including the preequilibrium and high energy fission processes. In the code, the level density parameter derived by Ignatyuk, the atomic mass table of Audi and Wapstra and the mass formula derived by Tachibana et al. are newly employed in the evaporation calculation part.

The calculated results are compared with the experimental ones. It is confirmed that HETC-3STEP reproduces the production of the nuclides having the mass number close to that of the target nucleus with an accuracy of a factor of two to three at incident proton energies above 100 MeV for ^{nat}Zr and ^{197}Au. However, the HETC-3STEP code has poor accuracy on the nuclide production at low incident energies and the light nuclide production through the fragmentation process induced by protons with energies above hundreds of MeV. Therefore, further improvement is required.

Keywords: HETC-3STEP, Proton-induced Nuclide Production, Cross Section, Code Intercomparison, 20 MeV to 5 GeV, Intranuclear Cascade, Preequilibrium, Evaporation, High Energy Fission

---

* Mitsubishi Research Institute, Inc.
** Kyushu University

20MeV から 5GeV の陽子入射による核種生成断面積に関する ＨＥＴＣ－３ＳＴＥＰ計算

日本原子力研究所東海研究所原子炉工学部
高田　　弘・義澤　宣明*・石橋　健二**

(1996年７月１日受理)

ＯＥＣＤ／ＮＥＡ国際コード比較のために、^{16}O, ^{27}Al, ^{nat}Fe, ^{59}Co, ^{nat}Zr及び^{197}Auに20MeVから5GeVの陽子を入射した場合の核種生成断面積を、前平衡過程及び高エネルギー核分裂過程を考慮した核内カスケード・蒸発モデルに基づくＨＥＴＣ－３ＳＴＥＰコードを用いて計算した。コードでは、Ignatyukによる準位密度パラメータ、AudiとWapstraの質量表及びTachibanaらにより導出された質量公式が蒸発計算部で新規に用いられた。

計算結果は実験結果と比較された。ＨＥＴＣ－３ＳＴＥＰコードは^{nat}Zr及び^{197}Au標的核において、標的核に近い質量数の核種生成について100MeV以上の入射エネルギー領域でファクター２～３の精度で予測できることが確認された。しかしながら、低い入射エネルギーにおける核種生成、数百MeV以上の陽子入射により引き起こされるフラグメンテーション過程からの軽い核種の生成の予測精度は良くない。したがって、一層のモデルの改良が必要である。

東海研究所：〒319－11　茨城県那珂郡東海村白方白根２－４
＊　㈱三菱総合研究所
＊＊　九州大学

Contents

目　　次

1. Introduction

Recently, the interest has increased in applications of a high energy intense proton accelerator to such facilities as spallation neutron sources for basic sciences and an accelerator-based nuclear transmutation system for nuclear engineering. In the neutronics design study of the facilities, neutron yield and neutron energy spectra in a spallation target are important factors to determine the neutronic performance of the facilities. Moreover, it is necessary to estimate the amount of the radioactivity of the various nuclides produced in the spallation target from the viewpoints of the neutronics and the radiation safety. For these demands, nuclear data are required in the intermediate energy region of 20 to 1600 MeV. Since there are scarce experimental data especially for the neutron incidence, the evaluation of the nuclear data in the intermediate energy region relies upon the theoretical calculations.

As for the calculation code, the nucleon-meson transport codes such as LAHET[1], HETC-KFA2[2] have generally been utilized for the neutronics calculation of the spallation target because they can simulate both the nuclear reactions and the particle transport in a thick medium based on the Monte Carlo method within acceptable computation time. In JAERI, the NMTC/JAERI code[3] has been employed. The code is essentially the same as LAHET and HETC-KFA2 except for the treatment of the high energy fission process[4,5] in the nuclear reaction. These codes assumes that the nuclear reaction consists of the intranuclear cascade (INC) process and the evaporation one. The high energy fission process is treated as the competitive one with the evaporation. The model developed by Bertini[6] and that made by Dresner[7] are employed for the simulation of the INC process and the evaporation one, respectively.

The intermediate energy nuclear data has been also concerned with the recent development of the preequilibrium reaction analysis models[8] in the energy region below 200 MeV. With these growing interests, a benchmark calculation was conducted by OECD/NEA for investigating the accuracy of various calculation models and codes on the nucleon emission cross section of the (p, xp') and (p, xn) reactions at incident energies of 25 to 1600 MeV.[9] The authors carried out benchmark calculations with the two codes of NUCLEUS[10] and HETC-3STEP[11] which are both based on the INC model of Bertini. The former has been implemented for the nuclear reaction calculation part in the NMTC/JAERI and the latter has been developed from HETC-KFA2 to take account for the preequilibrium process. It was confirmed through the benchmark calculation that HETC-3STEP gave better prediction than

NUCLEUS on the neutron emission cross sections.[12]

As the next step of the intercomparison, a benchmark problem was proposed[13] by OECD/NEA for the proton-induced nuclide production cross sections on the targets of ^{16}O, ^{27}Al, ^{nat}Fe, ^{59}Co, ^{nat}Zr and ^{197}Au at incident energies of 20 MeV to 5 GeV. In this work, calculations were carried out using the HETC-3STEP code to investigate its accuracy on the nuclide production cross section. The calculated results were compared with the experimental data.

2. Calculation Procedure

2.1 Intranuclear Cascade Process

HETC-3STEP is a Monte Carlo code modified from HETC-KFA2 to treat the preequilibrium process using a closed form exciton model[14], and consists of three processes of the INC, preequilibrium and evaporation. For the INC calculation, the revised version of the INC calculation code developed by Bertini, MECC-7[15], was implemented. In MECC-7, the target nucleus is divided into concentric three regions. The nucleon densities having the fractions of 0.9, 0.2 and 0.01 to the central one are given in the order from inner to outer region. The values of outer radii of those regions are given in a data file. For i-th region, the nucleon density is given by $\rho_i^n = \rho_i\ (A\text{-}Z)$ for neutron and $\rho_i^p = \rho_i\ Z$ for proton, where A and Z are the mass and atomic number, respectively. The density parameter of ρ_i is also supplied by the data file. The Fermi energy E_i^n of i-th region is given as $E_i^n = U_i\ (A\text{-}Z)$ for neutron and $E_i^p = U_i\ Z$ for proton. The parameter U_i is also given in the data file.

In MECC-7, the nucleon-nucleon collisions in the target nucleus are treated as a sequence of two-body collision between free nucleons. The free nucleon-nucleon cross sections compiled by Bertini[6] are used. The cross sections are given for nucleons in the energy region below 3.5 GeV, while they are given for charged pions up to 2.5 GeV. For the nucleon-nucleon and pion-nucleon non-elastic collisions in the higher energy region, the cross sections at 3.5 and 2.5 GeV are used as the input to scaling routines that employ the extrapolation method of Gabriel et al.[16]. The mean free path of a travelling particle and the collision probability of the particle with intranuclear nucleons are determined using the nucleon-nucleon and pion-nucleon scattering cross sections.

NUCLEUS on the neutron emission cross sections.[12]

As the next step of the intercomparison, a benchmark problem was proposed[13] by OECD/NEA for the proton-induced nuclide production cross sections on the targets of ^{16}O, ^{27}Al, ^{nat}Fe, ^{59}Co, ^{nat}Zr and ^{197}Au at incident energies of 20 MeV to 5 GeV. In this work, calculations were carried out using the HETC-3STEP code to investigate its accuracy on the nuclide production cross section. The calculated results were compared with the experimental data.

2. Calculation Procedure

2.1 Intranuclear Cascade Process

HETC-3STEP is a Monte Carlo code modified from HETC-KFA2 to treat the preequilibrium process using a closed form exciton model[14], and consists of three processes of the INC, preequilibrium and evaporation. For the INC calculation, the revised version of the INC calculation code developed by Bertini, MECC-7[15], was implemented. In MECC-7, the target nucleus is divided into concentric three regions. The nucleon densities having the fractions of 0.9, 0.2 and 0.01 to the central one are given in the order from inner to outer region. The values of outer radii of those regions are given in a data file. For i-th region, the nucleon density is given by $\rho_i^n = \rho_i\ (A\text{-}Z)$ for neutron and $\rho_i^p = \rho_i\ Z$ for proton, where A and Z are the mass and atomic number, respectively. The density parameter of ρ_i is also supplied by the data file. The Fermi energy E_i^n of i-th region is given as $E_i^n = U_i\ (A\text{-}Z)$ for neutron and $E_i^p = U_i\ Z$ for proton. The parameter U_i is also given in the data file.

In MECC-7, the nucleon-nucleon collisions in the target nucleus are treated as a sequence of two-body collision between free nucleons. The free nucleon-nucleon cross sections compiled by Bertini[6] are used. The cross sections are given for nucleons in the energy region below 3.5 GeV, while they are given for charged pions up to 2.5 GeV. For the nucleon-nucleon and pion-nucleon non-elastic collisions in the higher energy region, the cross sections at 3.5 and 2.5 GeV are used as the input to scaling routines that employ the extrapolation method of Gabriel et al.[16]. The mean free path of a travelling particle and the collision probability of the particle with intranuclear nucleons are determined using the nucleon-nucleon and pion-nucleon scattering cross sections.

When the travelling particle collides non-elastically with the intranuclear nucleon, the Pauli exclusion principle is treated as follows: The nucleons in a nucleus are assumed to occupy all the energy levels up to Fermi energy. When the nucleon-nucleon collision is simulated, the energies of two nucleons after the collision are compared with the Fermi energy, individually. If both of the nucleon energies are higher than Fermi energy, the collision is allowed and the directions of motion of the nucleons are determined based on the differential cross section compiled by Bertini[6]. If the energy of one nucleon is lower than the Fermi energy, the collision is prohibited and a new collision point is sampled again. This procedure is applied to all the moving particles until either their energy decreases down to a termination energy or the particles goes out of the nucleus.

In the INC calculation, the value of 7 MeV is given as the binding energy to all nuclides everywhere inside nucleus. A correlated two nucleon cluster is not taken into consideration in the code. The optical feature of the nucleus of the surface reflection and refraction is treated neither.

2.2 Preequilibrium Process

The next phase of the calculation is the preequilibrium process. The INC process is terminated when energies of all the travelling particles lower down to a cutoff energy, E_c. This cutoff energy was introduced in the code for suppressing low-energy particle emission and given by the use of a probability function. The probability function is expressed as

$$f(E_c)=\frac{2}{E_0}(1-\frac{E_c}{E_0}), \tag{1}$$

where the value of Eo is determined as 40 MeV. For the preequilibrium calculation, a closed form exciton model proposed by Gudima et al.[14] is adopted. The number of particles in the exciton state, p_0, at an initial stage of the preequilibrium process is that of allowed collisions during the INC process. The number of holes, h_0, is p_0-1. The preequilibrium calculation is carried out in the framework of a Monte Carlo algorithm formulated by Nakahara and Nishida[17]. In the exciton model, the reaction rate is obtained by summing three kinds of transition rates concerning to the exciton states $\lambda_+(p,h,E)$, $\lambda_o(p,h,E)$ and $\lambda_-(p,h,E)$, and the particle emission rate. Here, the emission rate $\lambda_c j(p,h,E,T)$ of a nucleon j is expressed as[14]:

$$\lambda_c^j(p, h, E, T)=\frac{2S_j+1}{\pi^2\hbar^3}\mu_j R_j(p, h)\frac{\omega(p-1, h, E-B_j-T)}{\omega(p, h, E)}T\sigma_{inv}(T), \quad (2)$$

where p = number of particles,

h = number of holes,

E = excitation energy,

T = the kinetic energy of an emitted nucleon,

$\sigma_{inv}(T)$ = the inverse cross section for the emission of nucleon,

S_j = the spin of emitted nucleon j,

B_j = the binding energy of emitted nucleon j,

μ_j = the reduced mass of emitted nucleon j.

Here, $\omega(p, h, E)$ indicates the level density of the n-exciton state, which is obtained on the basis of the equidistant level scheme with the single-particle density, and $R_j(p, h)$ the condition for the exciton chosen to be the nucleon j.

In comparison with the result of a moving source analysis[18], it was found that the transition rate on the interaction between excitons should adjust to some extent. Therefore, the transition rates are multiplied by a factor of F represented as F=max(0.2, 3.4-12/A$^{1/2}$), where A is the mass number of a target nucleus. The six particles of neutron, proton, deuteron, triton, helium-3 and alpha are taken into account as the emitted particles. Here, the emission rate of cluster is obtained by replacing the term of $\omega(p\text{-}1, h, E\text{-}B_j\text{-}T)/\omega(p, h, E)$ in Eq.(2) with

$$\gamma_j \cdot \frac{\omega(p-p_j, h, E-B_j-T)}{\omega(p, h, E)} \cdot \frac{\omega(p_j, 0, B_j+T)}{g_j} \quad . \quad (3)$$

Here,

$$\gamma_j=p_j^3\left(\frac{p_j}{A}\right)^{p_j-1}, \quad (4)$$

and

$$g_j(T)=\frac{V(2S_j+1)(2\mu_j)^{\frac{3}{2}}}{4\pi^2\hbar^3}(T+B_j)^{\frac{1}{2}}, \quad (5)$$

where V stands for the nuclear volume.

The angular distribution of an emitted particle is assumed to be isotropic. It was confirmed through the analysis[8] of double differential cross section of the (p,xn) reaction that the calculated results were in good agreement with experimental ones.

2.3 Evaporation Process

The final phase of the calculation is the statistical decay process of an excited residual nucleus. The EVAP program based on the evaporation model of Weisskopf-Ewing[19] is employed in the code. It is noted that the fission process is treated as a competitive process with the evaporation one. In HETC-3STEP, the high energy fission model proposed by Atchison[5] is implemented. The fission process is chosen by a sampling with the uniform random number according to fraction of the fission probability Γ_f to the summation of the fission width Γ_f and the neutron emission width Γ_n:

$$P_f = \frac{\Gamma_f}{\Gamma_f + \Gamma_n} \quad . \tag{6}$$

It should be noted that the fission probability of the sub-actinide nuclides with the atomic number less than 89 is also taken into account because a highly excited nucleus makes fission reaction for the intermediate energy nucleon incidence. The fission probability was determined on the basis of the experimental data.

When an excited nucleus makes the particle evaporation, the emission probability of a particle j from the evaporation process, P_j, is represented as

$$P_j = (2S_j + 1)\, m_j\, \varepsilon\, \sigma_{cj}(\varepsilon)\, \omega(E) \quad , \tag{7}$$

with

$$E = U - Q_j - \varepsilon \quad , \tag{8}$$

where S_j, m_j, σ_j, and Q_j are the spin, mass, inverse reaction cross section and binding energy for the emission of the particle j. As for the inverse cross section, the value obtained by the empirical formula derived by Dostrovsky[20] is employed. In Eqs. (7) and (8), ε and U are the kinetic energy of an emitted particle and the excitation energy of a compound nucleus,

respectively. The value of $\omega(E)$ stands for the energy level density of a residual nucleus. It is given as

$$\omega(E)=\omega_0 \exp\left[2\sqrt{a(E-\delta)}\right] , \tag{9}$$

with

$$a=\frac{A}{B}\left(1+Y\frac{\Delta^2}{A^2}\right) , \tag{10}$$

where δ is the pairing energy and a is the level density parameter, in which B is treated as the parameter in the code. Here, Δ is given as A-2Z by the use of the mass number and the atomic number of a residual nucleus. A value of 1.5 is given to Y.

For the level density parameter, either the values derived by Baba[21] or mass dependent value of $A/8$ have been employed so far. In this calculation, however, the values derived by Ignatyuk[22] with the parameters proposed by Mengoni et al.[23] were used. The Ignatyuk formula takes account for the excitation energy dependence in the level density. The level density parameters for individual nuclides are shown in Figs. 1 to 4.

In the evaporation process, the mass formula and the mass table are used to determine the binding energy of an emitted nucleon. The binding energy of a particle j is obtined on the basis of the mass excess as:

$$Q_j=M(A-FLA(j),Z-FLZ(j)) + M(FLA(j),FLZ(j))-M(A,Z) , \tag{11}$$

where $M(A,Z)$ indicates the mass excess of the nucleus having the mass number A and the atomic one Z. $FLA(j)$ and $FLZ(j)$ stand for the mass and atomic number of an emitted particle j. The value of mass excess is obtained by the mass table evaluated by Wapstra[24]. The mass formula derived by Cameron[25] is also employed to calculate the mass excess value of the nucleus which is not included in the mass table. In this calculation, we employed the mass table compiled by Audi and Wapstra[26] which supplemented more data to the preceding Wapstra's mass table. The mass formula was also replaced by the one derived by Tachibana et al..[27]

2.4 Benchmark Calculation

The combination of the target nucleus and the produced nuclides for the benchmark calculation is summarized in Table 1. The calculation was performed at the following incident energies: 15, 20, 25, 30, 35, 40, 45, 50, 60, 70, 80, 90, 100, 120, 140, 160, 180, 200, 250, 300, 350, 400, 450, 500, 600, 700, 800, 900, 1000, 1200, 1400, 1600, 1800, 2000, 2600, 3000, 4000 and 5000 MeV. Supplemental calculation was also made for different incident energies to investigate the energy dependence of the nuclide production cross section in detail. In the calculation, the number of incident protons was chosen as 250,000 for ^{16}O, ^{27}Al, and ^{nat}Fe, 200,000 for ^{nat}Zr and ^{197}Au, and 50,000 for ^{59}Co, respectively. It should be noted that the INC model cannot estimate the production of the isomer because the level structure of a nucleus is not considered in the model. Consequently, the isomer production was not calculated.

The calculated results were compared with the experimental data not only for the nuclide production cross section but for the reaction cross sections. The numerical data of the experiments were taken from the Refs. 28 to 32, and an abbreviation was attached to each datum in the Figs. 5 to 122. The sources corresponding to each abbreviation are listed in Appendix I for the reaction cross sections and Appendix II for the nuclide production ones, respectively. In the case that the experimental datum was given as cumulative cross section, the calculated cross section was obtained by adding the yields of all the parent nuclides to those of the produced nuclide. The parent nuclides are shown in the parentheses in Table 1.

3. Results and Discussion

3.1 Reaction Cross Section

In Figs. 5 to 10, the calculated reaction cross sections are compared with the experimental data[28]. It is observed that the calculated reaction cross section agrees with the experimental ones for the incident proton energy range between 20 and 50 MeV for the $^{16}O(p,x)$ reaction. Satisfactory agreement is obtained between the calculated and experimental results above 50 MeV for the $^{27}Al(p,x)$ reaction, while the calculated results are lower than the experimental ones between 20 and 50 MeV. HETC-3STEP also reproduces quite well the experimental results of the $^{nat}Fe(p,x)$ reaction except for those of Me60. Since the data of Me60 is apart from the

2.4 Benchmark Calculation

The combination of the target nucleus and the produced nuclides for the benchmark calculation is summarized in Table 1. The calculation was performed at the following incident energies: 15, 20, 25, 30, 35, 40, 45, 50, 60, 70, 80, 90, 100, 120, 140, 160, 180, 200, 250, 300, 350, 400, 450, 500, 600, 700, 800, 900, 1000, 1200, 1400, 1600, 1800, 2000, 2600, 3000, 4000 and 5000 MeV. Supplemental calculation was also made for different incident energies to investigate the energy dependence of the nuclide production cross section in detail. In the calculation, the number of incident protons was chosen as 250,000 for ^{16}O, ^{27}Al, and ^{nat}Fe, 200,000 for ^{nat}Zr and ^{197}Au, and 50,000 for ^{59}Co, respectively. It should be noted that the INC model cannot estimate the production of the isomer because the level structure of a nucleus is not considered in the model. Consequently, the isomer production was not calculated.

The calculated results were compared with the experimental data not only for the nuclide production cross section but for the reaction cross sections. The numerical data of the experiments were taken from the Refs. 28 to 32, and an abbreviation was attached to each datum in the Figs. 5 to 122. The sources corresponding to each abbreviation are listed in Appendix I for the reaction cross sections and Appendix II for the nuclide production ones, respectively. In the case that the experimental datum was given as cumulative cross section, the calculated cross section was obtained by adding the yields of all the parent nuclides to those of the produced nuclide. The parent nuclides are shown in the parentheses in Table 1.

3. Results and Discussion

3.1 Reaction Cross Section

In Figs. 5 to 10, the calculated reaction cross sections are compared with the experimental data[28]. It is observed that the calculated reaction cross section agrees with the experimental ones for the incident proton energy range between 20 and 50 MeV for the $^{16}O(p,x)$ reaction. Satisfactory agreement is obtained between the calculated and experimental results above 50 MeV for the $^{27}Al(p,x)$ reaction, while the calculated results are lower than the experimental ones between 20 and 50 MeV. HETC-3STEP also reproduces quite well the experimental results of the $^{nat}Fe(p,x)$ reaction except for those of Me60. Since the data of Me60 is apart from the

others, it seems that some error might be included in the data. As for the $^{59}Co(p,x)$ and $^{nat}Zr(p,x)$ reactions, it is possible to say that the calculated reaction cross sections are in good agreement with the experimental ones although the experimental data is quite few for the $^{nat}Zr(p,x)$ reaction. The calculated result of the $^{197}Au(p,x)$ reaction is larger than the experimental ones of Ab79 below 30 MeV, while it is consistent to the average of Ma64 and Ab79 at 30 MeV. Judging from the results shown in Figs. 5 to 10, the HETC-3STEP code can estimate the proton induced reaction cross sections well although some disagreement is observed below 30 MeV. The calculation reproduces the experimental results with an accuracy of 20% in the range from 50 MeV to 1 GeV.

3.2 Parameter Dependence

As described in the previous section, the level density parameter and the mass formula were revised in HETC-3STEP. In order to understand the effects of the parameter on the evaporation calculation quantitatively, some calculations were carried out. Figures 11 and 12 show the calculated results of neutron differential cross sections for the 80 and 256 MeV proton incidence on ^{90}Zr, respectively. It is observed in both figures that the neutron cross section increases in the energy region below 10 MeV when the level density parameters derived with the Ignatyuk formula are used. As shown in Figs. 1 to 4, the level density parameters obtained with the Ignatyuk formula are larger than those derived by Baba. Consequently, the cross section of the neutron emission in the evaporation process increases according to Eqs. (7) and (9). As for the mass table and mass formula, significant difference is not observed even after they were revised. The supplemented data in the mass table of Audi and Wapstra are for the nuclides which are mainly neutron rich ones. Most of data are the same as for the preceding Wapstra's mass table. The yield of nuclides supplemented in the mass table is too low so that the resultant mass yield is naturally almost the same as for the one obtained by the use of Wapstra's mass table. Therefore, the dot-dashed line lies upon the solid line. Figures 13 and 14 show the calculated proton differential cross sections for the 80 and 256 MeV proton incidence on ^{90}Zr, respectively. It is confirmed that the proton yield also increases by 10 to 20 % as well as the neutron yield when the level density parameters derived with the Ignatyuk formula are used.

Figures 15 to 18 show the calculated results of the neutron and proton emission differential cross sections for ^{208}Pb at incident proton energies of 80 and 256 MeV,

respectively. For ^{208}Pb, the level density parameter derived by Baba is extremely low because ^{208}Pb is the double magic nucleus. On the contrary, the values obtained by Ignatyuk formula become larger with the increase of the excitation energy of a residual nucleus. This leads to the increase of the particle emission in the evaporation process. As seen in Fig. 18, the proton emission cross section in the evaporation process significantly increases for the 256 MeV proton incidence.

The calculated mass yields of the ^{90}Zr target are shown in Figs. 19 and 20 for incident proton energies of 80 and 256 MeV, respectively. It is observed in Fig. 19 that the calculation with the Baba's level density parameter estimates the yield of the produced nuclides with the mass numbers of 84 and 85 extremely low for the 80 MeV proton incidence. This tendency appears also in Fig. 20. The calculation with the Ignatyuk's level density parameter, on the other hand, gives higher yield of nuclides having the mass numbers of 85 and 86 for the 80 MeV proton incidence, while the production with the mass number below 84 decreases. The resultant mass yield distribution shows a peak at the mass number of 86. For the 256 MeV proton incidence, the calculation increases the yield of the nuclides having the mass numbers between 83 and 85 so that the gaps observed in the calculation using the level density parameter of Baba are flattened.

The calculated mass yields of ^{208}Pb are shown in Figs. 21 and 22 for incident proton energies of 80 and 256 MeV, respectively. It is observed in both figures that the qualitatively the same shifts as for the ^{90}Zr target are obtained in the mass yield distributions for the 80 and 256 MeV proton incidence by changing the level density parameter of Baba to that of Ignatyuk. Judging form the mass yield distribution for the 256 MeV proton incidence, the Ignatyuk's parameter seems to give better mass yield than Baba's parameter because the former makes smooth mass yield distribution than the latter.

3.3 Nuclide Production via $^{16}O(p,x)$ Reaction

The nuclide production cross sections calculated with HETC-3STEP for ^{16}O are shown in Figs. 23 to 26. The experimental data of the $^{16}O(p,x)^{7}Be$ reaction gradually increase with the incident energy above 100 MeV. The calculated result, however, shows a peak around 70 MeV and decreases with incident energy and so deviates from the experimental result by one order of magnitude or more in the energy region of hundreds of MeV to 5 GeV. It is observed in Fig. 24 that HETC-3STEP cannot reproduce the experimental cross sections of the $^{16}O(p,x)^{10}Be$

reaction in the energy range between 50 and 100 MeV. It is also obvious that HETC-3STEP allows the ^{10}Be production below the threshold energy. This indicates that the present INC model does not treat the threshold of nuclear reaction correctly. In the energy region between 600 and 1600 MeV, the calculated result agrees with the experimental one of Yiou et al. which is six to seven times lower than the other data.

Figure 25 shows that HETC-3STEP reproduces the experimental results of the ^{16}O(p,x) ^{11}C reaction near the threshold energy. The experimental result comes to 18 mb at incident energy of 50 MeV and slightly decreases down to 10 mb with the increase of the incident energy. On the other hand, the calculated result increases up to 6 mb and gradually decreases as a function of the incident energy and so gives one-third lower cross section of the experimental data. For the ^{16}O(p,x)^{14}C reaction exhibited in Fig. 26, the calculated result shows quite different behavior from the experimental ones in the whole energy region.

It is concluded from these results that HETC-3STEP has poor accuracy on the nuclide production cross sections of ^{16}O for the proton incidence. This deficiency rises mainly from the approximation used in the INC model that treats the interaction between a projectile and a target nucleus as a sequence of two-body collisions between free nucleons. It is predicted[33] that the ^{16}O nucleus consists of four alpha clusters in the ground state so that the alpha clusters are emitted by a direct reaction. This process, however, is not included in the INC model yet so that the nucleon emission might be enhanced. This leads to the underestimation of the nuclide production of ^{7}Be and ^{10}Be which are apart from the target nucleus in the mass number.

3.4 Nuclide Production via ^{27}Al(p,x) Reaction

The nuclide production cross sections calculated with HETC-3STEP for ^{27}Al are shown in Figs. 27 to 31. The experimental data of the ^{27}Al(p,x)^{7}Be reaction rise up at 30 MeV and increase up to 10 mb with incident energy. HETC-3STEP produces ^{7}Be in the energy region above 50 MeV. The calculated cross section increases steeply at 50 MeV and then gradually decreases. In consequence, the calculated result deviates from the experimental data with the increase of incident energy above 300 MeV. In the GeV region, the disagreement over one order of magnitude is observed between the calculated and experimental results. For the ^{10}Be production, there are only four experimental results between 20 MeV and 5 GeV. In comparison with these data, HETC-3STEP gives about one order of magnitude lower cross

section in the energy region above 600 MeV. The significant underestimation of the productions of ^{7}Be and ^{10}Be by the HETC-3STEP calculation seems to come from the lack of the fragmentation process. This underestimation is commonly obtained in the calculated results of the ^{16}O (p,x) reactions. Moreover, there is a large discrepancy between the calculated and experimental result in the several tens of MeV region. This poor estimation is ascribed to the inadequate description of the cluster emission via the preequilibrium process rather than the lack of the fragmentation process.

It is observed in Fig. 29 that HETC-3STEP gives better agreement with the experimental data for the ^{27}Al(p,x)^{22}Na reaction than for the production of the Be isotopes. The calculated cross section agrees with the experimental ones with the accuracy of a factor of two in the energy region between 35 and 100 MeV. The agreement between the calculation and experiment becomes better with the increase of incident energy. In the energy region above 200 MeV, in particular, the agreement is excellent.

As seen in Fig. 30, HETC-3STEP also reproduces the ^{24}Na production fairly well in the energy region above 80 MeV. The agreement becomes little worse with the increase of incident energy. In the energy region between 20 and 60 MeV, on the other hand, the calculated cross section is much higher than the experimental data. The cause of this discrepancy can be ascribed to the fact that the binding energy of the nuclear reaction is not correctly taken into account in the present INC model.

In Fig. 31, it is observed that HETC-3STEP reproduces the production cross section of ^{26}Al qualitatively well above 30 MeV. Quantitatively, however, the calculation gives the cross section about twice as large as the experimental ones. The poor accuracy of the HETC-3STEP calculation on the nuclide production near the threshold energy is found in this reaction, too. Judging from these comparisons of the nuclide productions on ^{27}Al, HETC-3STEP estimates the production cross section of the nuclides having near mass number to the target nucleus with the accuracy of about a factor of two in the energy region above 100 MeV.

3.5 Nuclide Production via ^{nat}Fe(p,x) Reaction

The nuclide production cross sections calculated with HETC-3STEP for ^{nat}Fe are shown in Figs. 32 to 45. It is clearly observed in Figs. 32 and 33 that HETC-3STEP cannot predict well the productions of ^{7}Be and ^{10}Be at all due to the lack of the fragmentation process. The experimental cross section of the ^{7}Be production reaches relatively large values of 6 to 10 mb

in the GeV region in comparison with the other nuclide production on ^{nat}Fe.

HETC-3STEP gives the ^{22}Na production cross section value only in the energy region above 500 MeV, while the experimental data are measured even in the energy region between 100 and 500 MeV. As far as the energy region above 500 MeV is concerned, the calculated result agrees with the experimental data by a factor of two to three. Similar result is observed in Fig. 36 for the ^{26}Al production although the agreement between the calculated and experimental results is worse.

For the $^{nat}Fe(p,x)^{24}Na$ reaction, HETC-3STEP calculates the ^{24}Na production only in the energy region above 600 MeV as well as for the productions of ^{22}Na and ^{26}Al. The calculated cross section, however, is one-third of the experimental data. It is found from these results that the problem of the lack of the fragmentation process in the calculation model is serious for estimating production of light nuclides, especially the Be isotopes. The recent study(34) taking account of the cross section of the fragmentation process by a semi-empirical formula may be useful for further improvement of HETC-3STEP.

It is observed in Fig. 37 that the HETC-3STEP result agrees with the experimental ones very well for the ^{46}Sc production although there are only a few data available. For the ^{48}V production, HETC-3STEP gives lower cross section than the experiments in the energy region above 40 MeV. It approaches about one-sixth to one-eighth of the experimental data in the GeV region. On the contrary, a significant overestimation is observed in the calculated result for the $^{nat}Fe(p,x)^{48}Cr$ reaction in Fig. 39. It is of interest that the degree of agreement between the calculated and experimental results is quite different on the production of ^{48}V and ^{48}Cr in spite of the same mass number. Since the atomic numbers of ^{48}V and ^{48}Cr are 23 and 24, respectively, this indicates that the production of ^{48}Cr might be enhanced because the yields of charged particles such as proton, deuteron and alpha particle are not estimated correctly in HETC-3STEP. Therefore, it is necessary to check the treatment of the charged particle emission in the HETC-3STEP code.

As for the ^{51}Cr production cross section, it is observed in Fig. 40 that the HETC-3STEP results agree with the experimental data quite well in the energy region above 60 MeV although the calculation gives noticeably lower cross section than the experimental data in the energy region between 30 and 50 MeV.

As seen in Fig. 41, HETC-3STEP cannot reproduce the cross section of the $^{nat}Fe(p,x)^{52m+g}Mn$ reaction. The overestimation of a factor of about six is observed in the calculated

result in the energy region between 50 and 500 MeV. Since the present evaporation model cannot treat the production of the meta-stable isotopes, the lack of the ^{52m}Mg production in the calculation seems to cause the disagreement. As described in section 2, the particle emission in the statistical decay process depends only upon the excitation energy of a residual nuclide. Neither the spin nor the angular momentum of a residual nuclide is taken into account in the present evaporation model. The inclusion of the Hauser-Feshbach model[35] which can treat those physical characteristics may enable the HETC-3STEP code to simulate the particle emission in the evaporation process more precisely.

It is observed in Fig. 42 that the HETC-3STEP result achieves excellent agreement with the experimental results for the ^{nat}Fe(p,x)^{54}Mn reaction almost in the whole incident energy range. As shown in Fig. 43, a large extent of overestimation is observed in the calculated result in the energy range between 20 and 50 MeV for the ^{nat}Fe(p,x)^{52}Fe reaction, while fairly good agreement is obtained between the calculated and experimental results at 600 MeV. Figures 44 and 45 show that the HETC-3STEP calculation qualitatively reproduces the variation of the production cross sections of ^{55}Co and ^{56}Co as a function of the incident energy. However, the calculated result is larger than the experimental data by a factor of two to three for both cases. The nuclides of ^{55}Co and ^{56}Co are produced mainly by the charge exchange reactions of ^{56}Fe(p,2n)^{55}Co and ^{56}Fe(p,n)^{56}Co, respectively. Judging from the analysis of the neutron emission cross section[12], HETC-3STEP predicts the neutron emission reasonably well. The discrepancy in the productions of ^{55}Co and ^{56}Co seems to come from the following aspect: Proton emission is estimated too low in the present INC model so that the cross sections of the (p,n) and (p, 2n) reactions are enhanced.

3.6 Nuclide Production via ^{59}Co(p,x) Reaction

The nuclide production cross sections calculated with HETC-3STEP for ^{59}Co are shown in Figs. 46 to 50. It is observed in Fig. 46 that HETC-3STEP gives a factor of two to three larger cross section than the experimental ones for the ^{56}Co production in the energy region above 40 MeV. The disagreement between the calculated and experimental result below 30 MeV comes from the lack of the treatment of threshold energy in the INC model. As seen in Fig. 47, on the other hand, HETC-3STEP reproduces well the experimental results for the ^{57}Co production at incident proton energies above 35 MeV, while the calculated cross section is much

lower than the experimental ones in the energy range between 20 and 35 MeV. Figure 48 exhibits that HETC-3STEP result agrees fairly well with the experimental data of Meadows et al. between 20 and 50 MeV for the ^{58}Co production. The code, however, gives twice as large cross section as the experimental ones in the hundreds of MeV region.

It is observed in Fig. 49 that HETC-3STEP cannot reproduce the experimental results of the ^{59}Co(p,4n)^{56}Ni reaction at all. The calculated result is larger than the experimental ones over an order of magnitude in the energy range between 40 and 100 MeV. The similar tendency is observed in the calculated result for the ^{57}Ni production as seen in Fig. 50. In this case, HETC-3STEP gives about four times larger cross section than the experimental ones in the tens of MeV region. This overestimation becomes more significant with increase of the incident proton energy. The similar overestimation is observed in the results of ^{nat}Fe(p,n)^{56}Co and ^{nat}Fe(p,2n)^{55}Co. However, the degree of disagreement between the calculated and experimental results is worse for the ^{59}Co(p,4n)^{56}Ni and ^{59}Co(p,3n)^{57}Ni reactions than for the ^{nat}Fe(p,n)^{56}Co and ^{nat}Fe(p,2n)^{55}Co ones. Moreover, HETC-3STEP cannot reproduce the production cross sections near threshold energy for both the ^{56}Ni and ^{57}Ni production. This is attributed to the lack of the threshold energy in the INC calculation as mentioned above.

3.7 Nuclide Production via ^{nat}Zr(p,x) Reaction

The nuclide production cross sections calculated with HETC-3STEP for ^{nat}Zr are shown in Figs. 51 to 72. It is evident in Fig. 51 that HETC-3STEP cannot predict the ^{7}Be production at all. This is the same result as for the calculation of the ^{nat}Fe (p,x)^{7}Be reaction because the fragmentation process is not treated in the code. It is observed in Figs. 52 to 58 that the calculated results rise up rapidly from the threshold energy and become almost constant in the GeV region for the productions of ^{22}Na, ^{48}V, ^{51}Cr, ^{54}Mn, ^{56}Co, ^{58}Co and ^{65}Zn, respectively. For those reactions, the calculated results are larger than the experimental ones by a factor of two or more. In particular, the significant overestimation is observed in the HETC-3STEP calculations of the ^{48}V and ^{56}Co productions (see Figs. 53 and 56). The disagreement is attributed to the aspect that the amount of the light fragment emission is estimated too low. This is consistent with the significant underestimation of the ^{7}Be production shown in Fig. 51. With more light fragment emission, a large amount of energy is carried away from the residual nuclide so that the number of emitted nucleons could decrease. This may improve the

disagreement in the nuclide productions of ^{22}Na to ^{65}Zn.

Judging from the results shown in Figs. 59 to 62, the HETC-3STEP calculation reproduces the experimental data for the ^{74}As and ^{81}Kr productions qualitatively better than the lighter nuclides from ^{22}Na to ^{65}Zn shown in Figs. 52 to 58. There exists, however, the disagreement of about a factor of three between the calculated and experimental results. As far as the ^{85}Kr production is concerned, HETC-3STEP gives extremely larger cross section than the experimental ones in the energy region below 200 MeV. Though the calculated result approaches to the experimental one with increase of the incident energy, it oscillates unreasonably as seen in Fig. 62. The nuclide of ^{85}Kr is not produced independently but cumulatively by the decay of ^{85}Se and ^{85}Br. The resultant cross section is as small as in the order of mb. Therefore, the oscillation may be attributed to the statistical error of the cross sections of ^{85}Se and ^{85}Br .

It is observed in Figs. 63 and 64 that HETC-3STEP gives larger cross sections for the productions of ^{83}Rb and ^{84}Rb in the whole energy region. The disagreement observed near the threshold energy is significant, particularly in the case of the ^{84}Rb production. The calculated results are larger than the experimental ones in the energy region below 100 MeV. On the other hand, HETC-3STEP agrees well with experimental results of ^{86}Rb although there are only two data.

For the ^{nat}Zr(p,x)^{85}Sr reaction, HETC-3STEP again gives larger cross section than the experimental ones as seen in Fig. 65. As far as the data of Michel are concerned, however, the agreement between the calculated and experimental result is fair. One can see in Figs. 66 and 67 that the cross sections of the ^{86}Y and ^{87}Y productions have been measured only in the energy region below 80 MeV. The experimental result shows a peak at 26 MeV for ^{86}Y, and at 20 MeV for ^{87}Y, respectively. Such peaks, however, do not appear in the calculated results in both cases. Since the threshold energy is not treated correctly, HETC-3STEP cannot reproduce the experimental data below 80 MeV.

For the ^{nat}Zr(p,x)^{88}Y reaction, it is observed in Fig. 68 that HETC-3STEP agrees fairly well with the experimental data in the energy region between 180 and 600 MeV. With increase of the incident energy, the agreement comes worse to be a factor of two or more. It is observed in Fig. 70 that HETC-3STEP gives several times larger cross sections than the experimental results in the energy region above 60 MeV for the ^{nat}Zr(p,x)^{88}Zr reaction. As seen in Fig. 71, the tendency of the calculated result for the ^{nat}Zr(p,x)^{95}Zr reaction is quite different from that of

the experimental ones in the energy range below 80 MeV. Even above 80 MeV, the underestimation of one order of magnitude is observed in the HETC-3STEP result. On the contrary, the code gives larger cross sections for the ^{90}Nb production by one order of magnitude (see Fig. 72). The main reaction for the ^{90}Nb production is ^{90}Zr(p,n)^{90}Nb because ^{90}Zr occupies the fraction of 0.51 among the natural isotopes which compose ^{nat}Zr. The overestimation of the calculated cross section of the ^{90}Zr(p,n)^{90}Nb reaction is attributed to the enhancement of the (p,n) reaction by the insufficient estimation of the proton emission as well as the case of ^{nat}Fe(p,n)^{60}Co.

3.8 Nuclide Production via ^{197}Au(p,x) Reaction

The nuclide production cross sections calculated with HETC-3STEP for ^{197}Au are shown in Figs. 73 to 122. Figure 73 proves that HETC-3STEP cannot estimate the ^{197}Au(p,x)^{7}Be reaction at all as well as for the ^{nat}Fe(p,x)^{7}Be and ^{nat}Zr(p,x)^{7}Be reactions. It is observed in Fig. 74 that HETC-3STEP reproduces the ^{24}Na production quite well. Fairly good agreement is also obtained between the calculated and experimental results for the productions of ^{24}Ne and ^{46}Sc (see Figs. 75 and 76). For the ^{197}Au(p,x)^{59}Fe and ^{197}Au(p,x)^{58}Co reactions, on the other hand, the disagreement of a factor of three to five is observed in the GeV region as seen in Figs. 77 and 78. Satisfactory agreement is obtained in Figs. 79 to 82 between the HETC-3STEP results and experimental data for the nuclide productions of ^{65}Zn, ^{75}Se, ^{87}Y and ^{89}Zr in the energy region above 200 MeV. It should be noted that HETC-3STEP reproduces the nuclide production of the medium-mass nuclides having the mass numbers of 24 to 95 in contrast with the fact that the code can not predict the production of those medium-mass nuclides for the ^{nat}Zr target. Since the high energy fission process of the sub-actinide nuclide is included in the HETC-3STEP code, the medium-mass nuclides are produced as a fission fragment through the high energy fission process in the calculation. The cross section of the proton induced fission reaction increases with the incident energy so that those medium mass nuclides are produced via the fission process rather than the fragmentation one.

It is observed in Figs. 83 and 84 that the experimental cross sections of ^{95}Zr and ^{103}Ru are constant or decrease with the incident energy range between 200 MeV and 3 GeV, respectively. This is the different tendency from the experimental data of ^{87}Y and ^{89}Zr which have close mass numbers to ^{95}Zr and ^{103}Ru. The calculated result of HETC-3STEP, on the

other hand, increases monotonously with the incident energy. In consequence, the calculated results do not agree with the experimental ones at all.

As for the nuclide productions of ^{121}Te to ^{149}Tb, it is observed in Figs. 85 to 92 that the experimental cross sections increase rapidly in the GeV region. The calculated results of HETC-3STEP show the similar tendency with the experimental results in the GeV region for the productions of those nuclides. The agreement within a factor of two is obtained between the calculation and experiments for the productions of ^{121}Te, ^{127}Xe, ^{131}Ba and ^{139}Ce. It is noted that the HETC-3STEP calculation gives extremely large cross section by about one order of magnitude at 400 MeV in comparison with the neighboring incident energies. From the physical point of view, it seems natural that the nuclide production cross section itself increases smoothly with the incident energy in the hundreds of MeV region because there is not any peculiar reaction channel such as the resonance reaction. Therefore, there might be some error in the computation procedure. Such peak does not appear in the nuclide production whose cross section becomes over 10 mb in the energy region above 100 MeV.

As seen in Figs. 93 and 94, the HETC-3STEP calculations reproduce the experimental data of ^{167}Tm and ^{166}Yb at 500 MeV, but they give one-forth or one-fifth lower cross sections than the experimental results in the GeV region. The similar results are obtained in the calculations of ^{197}Au(p,x)^{170}Lu and ^{197}Au(p,x)^{171}Lu (see Figs. 95 and 96). Here, the agreement between the calculated and experimental results is improved to be a factor of two in the GeV region. As seen in Figs. 100, 101 and 103, fairly good agreement is obtained in the productions of ^{172}Hf, ^{173}Hf and ^{175}Ta in the energy range between 490 MeV and 3 GeV. It is observed in Figs. 97, 98 and 102, on the other hand, that the calculated production cross sections of ^{172}Lu, ^{173}Lu and ^{175}Hf are too low to reproduce the experimental ones. The mass numbers of ^{167}Tm to ^{175}Hf are apart from that of the target nuclide of ^{197}Au by 20 to 30, and they are produced via the de-excitation of a highly excited nucleus rather than the fission process. Therefore, the disagreement in the GeV region indicates that the excitation energy at the evaporation stage is not estimated correctly in the HETC-3STEP code. The rough treatment of the cluster emission, which was pointed out in the previous sub-section, may be one of causes.

It is observed in Figs. 104 to 106 that the calculated results of HETC-3STEP are in satisfactory agreement with the experimental ones for the productions of ^{181}Re, ^{183}Re and ^{182}Os in the energy region above 500 MeV. The disagreement at 200 MeV seems to come from the crude treatment of the threshold energy in the code. Satisfactory agreement within a

factor of two is also achieved in the calculation of $^{197}Au(p,x)^{185}Os$ above 200 MeV as seen Fig. 108. Fairly good agreement is observed in Fig. 109 between the calculated and experimental results in the energy region between 500 MeV and 3 GeV for the production of ^{186}Ir although there are only two data. The similar result is obtained in the calculation of the ^{183}Os production as seen in Fig. 107. For the ^{187}Ir production, on the other hand, the HETC-3STEP result gives extremely lower cross sections than the experimental ones as shown in Fig. 110.

Figures 111 to 114 show that HETC-3STEP reproduces quite well the experimental production cross sections of the other Ir isotopes of ^{188}Ir, ^{189}Ir, ^{190}Ir and ^{192}Ir in the energy region above 200 MeV. It is observed in Figs. 115 and 116 that HETC-3STEP results are also in good agreement with the experimental ones for both the ^{188}Pt and ^{191}Pt productions. As seen in Figs. 117 to 120, the calculated result agrees fairly well with the experimental ones for the productions of ^{193}Au, ^{194}Au, ^{195}Au and ^{196}Au in the energy range above 200 MeV. For these nuclides, HETC-3STEP gives much lower cross sections than the experimental ones in the energy region below 100 MeV.

The disagreement between the calculated and experimental result in the energy region below 100 MeV is commonly observed in almost all the results. As the mass number of the produced nuclide becomes closer to that of the target nuclide of ^{197}Au, on the other hand, the agreement becomes quite better with increase of the incident energy above 200 MeV. As seen in Figs. 121 and 122, exceptionally, significant overestimation is observed in the calculated results for the ^{197}Au $(p,3n)^{195}Hg$ and $^{197}Au(p,n)^{197}Hg$ reactions.

4. Concluding Remarks

The nuclide production cross sections by the proton incidence on the targets of ^{16}O, ^{27}Al, ^{nat}Fe, ^{59}Co, ^{nat}Zr and ^{197}Au were calculated with the HETC-3STEP code at incident energies between 20 MeV to 5 GeV. The code simulates the nuclear reaction with the intranuclear cascade and evaporation model including the preequilibrium and high energy fission processes. In the calculation, the level density parameter derived with the Ignatyuk formula, the mass table of Audi and Wapstra and the mass formula of Tachibana et al. were newly employed in the evaporation calculation part.

It was confirmed that the HETC-3STEP calculation reproduces the experimental reaction cross sections for those target nuclides with the accuracy of 20 % in the energy region from 50

factor of two is also achieved in the calculation of $^{197}Au(p,x)^{185}Os$ above 200 MeV as seen Fig. 108. Fairly good agreement is observed in Fig. 109 between the calculated and experimental results in the energy region between 500 MeV and 3 GeV for the production of ^{186}Ir although there are only two data. The similar result is obtained in the calculation of the ^{183}Os production as seen in Fig. 107. For the ^{187}Ir production, on the other hand, the HETC-3STEP result gives extremely lower cross sections than the experimental ones as shown in Fig. 110.

Figures 111 to 114 show that HETC-3STEP reproduces quite well the experimental production cross sections of the other Ir isotopes of ^{188}Ir, ^{189}Ir, ^{190}Ir and ^{192}Ir in the energy region above 200 MeV. It is observed in Figs. 115 and 116 that HETC-3STEP results are also in good agreement with the experimental ones for both the ^{188}Pt and ^{191}Pt productions. As seen in Figs. 117 to 120, the calculated result agrees fairly well with the experimental ones for the productions of ^{193}Au, ^{194}Au, ^{195}Au and ^{196}Au in the energy range above 200 MeV. For these nuclides, HETC-3STEP gives much lower cross sections than the experimental ones in the energy region below 100 MeV.

The disagreement between the calculated and experimental result in the energy region below 100 MeV is commonly observed in almost all the results. As the mass number of the produced nuclide becomes closer to that of the target nuclide of ^{197}Au, on the other hand, the agreement becomes quite better with increase of the incident energy above 200 MeV. As seen in Figs. 121 and 122, exceptionally, significant overestimation is observed in the calculated results for the ^{197}Au $(p,3n)^{195}Hg$ and $^{197}Au(p,n)^{197}Hg$ reactions.

4. Concluding Remarks

The nuclide production cross sections by the proton incidence on the targets of ^{16}O, ^{27}Al, ^{nat}Fe, ^{59}Co, ^{nat}Zr and ^{197}Au were calculated with the HETC-3STEP code at incident energies between 20 MeV to 5 GeV. The code simulates the nuclear reaction with the intranuclear cascade and evaporation model including the preequilibrium and high energy fission processes. In the calculation, the level density parameter derived with the Ignatyuk formula, the mass table of Audi and Wapstra and the mass formula of Tachibana et al. were newly employed in the evaporation calculation part.

It was confirmed that the HETC-3STEP calculation reproduces the experimental reaction cross sections for those target nuclides with the accuracy of 20 % in the energy region from 50

MeV to 1 GeV. For the nuclide production cross sections, it was concluded from the comparisons with the experimental data that HETC-3STEP could estimate the production of the nuclide close to the target nucleus with the accuracy of a factor of two to three at the incident energies of 100 MeV to GeV for heavy nuclides of ^{nat}Zr and ^{197}Au. For the ^{197}Au target, HETC-3STEP also predicted reasonably well the nuclide production via the high energy fission process. The accuracy was kept for the production of the nuclides apart from the target by about 20 in mass number. Lighter the mass of produced nuclides becomes, worse the agreement between the calculated and experimental results becomes. In particular, the production of light fragment such as ^{7}Be and ^{10}Be were not estimated at all by the HETC-3STEP calculation. For lighter target nuclides, the accuracy of the HETC-3STEP calculation was poorer than for ^{nat}Zr and ^{197}Au even in the production of the nuclide close to the target nucleus.

The nuclide production itself depends upon the excited state of a residual nuclide. In fact, the mass yield distribution drastically changed due to the level density parameter. A very sophisticated calculation model is required to predict the nuclide production accurately. Considering that the present intranuclear cascade evaporation model treats the nuclear reaction in a very classical manner, the resultant accuracy of a factor of two to three seems to be acceptable.

In order to improve the accuracy of the nuclide production cross section in the framework of the intranuclear cascade evaporation model, the following physical aspects should be taken into account: (i) The accurate treatment of the threshold energy of the nuclear reaction, (ii) The inclusion of the fragmentation reaction, (iii) More accurate estimation of the charged particle emission in both the INC and preequilibrium processes, (iv) More precise simulation of the statistical decay process by the use of the Hauser Feshbach model[35]. Recent studies for including those physical aspects in terms of the nuclear medium effects[36], the fragmentation reaction cross section with a semi-empirical formula[34], and the pick-up reactions[37,38] for cluster formation may be useful to improve the HETC-3STEP code.

From an experimental point of view, on the other hand, the data are very few yet except for the production of nuclides having the mass number close to that of a target nucleus. The accumulation of experimental data are also important not only for analyzing the nuclide production mechanism through the spallation reaction but for establishing the systematic estimation of the nuclide production cross section.

Acknowledgments

The authors would like to thank Drs. Y. Nakahara and T. Nishida for their useful discussions on the intranuclear cascade evaporation model calculations. They are also indebted to Dr. H. Yasuda for his valuable comments and encouragement on this work.

References

1) Prael R. E., Lichtenstein H.: LA-UR-89-3014, "Users Guide to LCS: The LAHET Code System", (1989).
2) Cloth P., Filges D., Neef R. D., Sterzenbach G., Reul Ch., Armstrong T. W., Colborn B. L., Anders B., Brückmann H.: Jül-2203, "HERMES A Monte Carlo Program System for Beam Materials Interaction Studies", (1988).
3) Nakahara Y., Tsutsui T.: JAERI-M 82-198, "NMTC/JAERI A Code System for High Energy Nuclear Reactions and Nucleon-Meson Transport Code", (1982), [in Japanese].
4) Nakahara Y.: J. Nucl. Sci. Technol., 20, 511 (1983).
5) Atchison F.: Jül-Conf 34, "Proc. of Mtg. on Targets for Neutron Beam Spallation Source", KFA-Jülich, Germany, June 11-12, 1979, p17 (1980).
6) Bertini H. W.: Phys. Rev., 188, 1711 (1969).
7) Dresner L. W.: ORNL-TM-196, "EVAP - A Fortran Program for Calculating the Evaporation of Various Particles from Excited Compound Nuclei", (1962).
8) Gadioli E., Hodgson P. E.: "Pre-Equilibrium Nuclear Reactions", Oxford University Press (1992).
9) OECD/NEA: "Proc. of Specialists' Mtg. on Intermediate Energy Nucl. Data: Models and Codes", May 31 - June 1, Issy-les-Moulineaux, OECD Publications, Paris, (1994).
10) Nishida T., Nakahara Y., Tsutsui T.: JAERI-M 86-116, "Development of A Nuclear Spallation Simulation Code and Calculations of Primary Spallation Products", (1986), [in Japanese].
11) Yoshizawa N., Ishibashi K., Takada H.: J. Nucl. Sci. Technol., 32, 601 (1995).
12) Takada H., Nakahara Y., Nishida T., Ishibashi K., Yoshizawa N.: p121 in Ref. (9), (1994).
13) Michel R., Nagel P.: NEA/NSC/DOC(95) 8, "Specifications for An International Codes and Model Intercomparison for Intermediate Energy Activation Yields", (1995).
14) Gudima K. K., Mashnik S. G., Toneev V.D.: Nucl. Phys. A, 401, 329 (1983).
15) Bertini H. W., Guthrie M. P.: Nucl. Phys. A, 169, 670 (1971).
16) Gabriel T. A., Alsmiller Jr. R. G., Guthrie M. P.: ORNL-4542, "An Extrapolation Method for Predicting Nucleon and Pion Differential Production Cross Sections from High-Energy (> 3 GeV) Nucleon-Nucleon Collisions", (1970).
17) Nakahara Y., Nishida T.: JAERI-M 86-074, "Monte Carlo Algorithms for Simulating

Particle Emissions from Pre-equilibrium States during Nuclear Spallation Reactions", (1986).

18) Ishibashi K., Higo K., Sakaguchi S., Matsumoto Y., Wakuta Y., Takada H., Nishida T., Nakahara Y., Kaneko Y.: J. Nucl. Sci. Technol., 29, 499 (1992).

19) Weisskopf V. F., Ewing P. H.: Phys. Rev., 57, 472 (1940).

20) Dostrovsky I., Rabinowitz P., Bivinx R.: Phys. Rev., 111, 1659 (1958).

21) Baba H.: Nucl. Phys. A, 159, 625 (1970).

22) Ignatyuk A. V., Smirenkin G. N., Tishin A. S.: Sov. J. Nucl. Phys., 21, 256 (1975).

23) Mengoni A., Nakajima Y.: J. Nucl. Sci. Technol., 31, 151 (1994).

24) Cameron A. G. W.: Can. J. Phys., 35, 1021 (1957).

25) Wapstra A. M.: Physica, 21, 367 (1955).

26) Audi G., Wapstra A. M.: Nucl. Phys. A, 565, 1 (1993).

27) Tachibana T., Uno M., Yamada M., Yamada S.: At. Data Nucl. Data Tables, 39, 251 (1988).

28) Bauhoff W.: At. Data Nucl. Data Tables, 35, 429 (1986).

29) Schopper H. (Ed.): "LANDORT-BÖRNSTEIN, Numerical Data and Functional Relation ships in Science and Technology, New Series, Group I: Nuclear and Particle Physics, Vol. 13, Production of Radionuclides at Intermediate Energies, Subvol. a, Interactions of Protons with Targets from He to Br", Springer-Verlag, Berlin Heidelberg, (1991).

30) Schopper H. (Ed.): *ibid.*, "subvol. b, Interactions of Protons with Targets from Kr to Te", Springer-Verlag, Berlin Heidelberg, (1992).

31) Schopper H. (Ed.): *ibid.*, "subvol. c, Interactions of Protons with Targets from I to Am", Springer-Verlag, Berlin Heidelberg, (1993).

32) Schopper H. (Ed.): *ibid.*, "subvol. d, Interactions of Protons with Nuclei (Supplement to I/13a. b, c)", Springer-Verlag, Berlin Heidelberg, (1994).

33) Kanada-En'yo Y., Horiuchi A.: JAERI-CONF 95-012, "Proc. of the 2nd Symp. on Simulation of Hadronic Many-Body System", Nov. 30- Dec. 2, 1994, JAERI, Tokai, Japan, pp.76-80 (1995).

34) Shigyo N., Nakamoto T., Ishibashi K.: JAERI-CONF 96-008, "Proc. of the 1995 Symp. on Nucl. Data", Nov. 16-17, 1995, JAERI, Tokai, Japan, pp.272-277 (1996).

35) Hauser W., Feshbach H.: Phys. Rev., 87, 366 (1952).

36) Takada H.: J. Nucl. Sci. Technol., 33, 275 (1996).

37) Iwamoto A., Harada K.: Phys. Rev. C, 26, 1821 (1982).

38) Sato K., Iwamoto A., Harada K.: Phys. Rev. C, 28, 1527 (1983).

Appendix I: References for Experimental Reaction Cross Sections.

Ab79 Abegg R., Birchall J., Davison N. E., de Jong M. S., Ginther D. L., Hasell D. K., Nasr T., van Oers W. T. H., Carlson R. F., Cox J.: Nucl. Phys. A, 324, 109 (1979).

Be65 Bearpark K., Graham W. R., Jones G.: Nucl. Phys., 73, 206 (1965).

Bu65 Bulman P. J., Greenlees G. W., Sametband M. J.: Nucl. Phys., 69, 536 (1965).

Bu68 Bulman P. J., Griffith J. A. R.: Nucl. Phys. A, 111, 315 (1968).

Ca54a Cassels J. M., Lawson D.: Proc. Phys. Soc. A, 67, 125 (1954).

Ca75 Carlson R. F., Cox A. J., Nimmo J. R., Davison N. E., Elbakr S. A., Horton K. L., Houdayer A., Sourkes A. M., van Oers W. T. H., Margaziotis D. J.: Phys. Rev. C, 12, 1167 (1975).

Ch55 Chen F. F., Leavitt C. P., Shapiro A. M.: Phys. Rev., 99, 857 (1955).

Go59 Gooding T. J.: Nucl. Phys. 12, 241, (1959).

Go62 Goloskie R., Strauch K.: Nucl. Phys., 29, 474 (1962).

Jo61 Johansson A., Svandberg U., Sundberg O.: Arkiv Fysik, 19, 1957 (1961).

Ki54 Kirschbaum A. J.: PhD. Thesis, UCLA (1954).

Ki66 Kirby P, Link W. T.: Can. J. Phys., 44, 1847 (1966).

Ma64 Makino M. Q., Waddell C. N., Eisberg R. M.: Nucl. Phys., 50, 145 (1964).

Ma64a Makino M. Q., Waddell C. N., Eisberg R. M., Hestenes J.: Phys. Lett., 9, 178 (1964).

Mc74 McGill W. F., Carlson R. F., Short T. H., Cameron J. M., Richardson J. R., Slaus I., van Oers W. T. H., Verba J. W., Margaziotis D. J., Doherty, P.: Phys. Rev. C, 10, 2237 (1974).

Me60 Meyer V., Eisberg R. M., Carlson R. F.: Phys. Rev., 117, 1334 (1960).

Me60a Meyer V., Hintz N. M.: Phys. Rev. Lett., 5, 207 (1960).

Me71 Menet J. J. H., Gross E. E., Malanify J. J., Zucker A.: Phys. Rev. C, 4, 1114 (1971).

Mi54 Millburn G. P., Birnbaum W., Crandall W. E., Schecter L.: Phys. Rev., 95, 1268 (1954).

Po65 Pollock R. E., Schrank G.: Phys. Rev., 140B, 575 (1965).

Re72 Renberg P. U., Measday D. F., Pepin M., Schwaller P., Favier B., Richard-Serre C.: Nucl. Phys. A, 183, 81 (1972).

Tu64 Turner J. F., Ridley B. W., Cavanagh P. E., Gard G. A., Hardacre A. G.: Nucl. Phys., 58, 509 (1964).

Wi63 Wilkins B. D., Igo G.: Phys. Rev., 129, 2198 (1963).

Appendix II. References for Experimental Nuclide Production Cross Sections.

Alb62 Albouy M. G., Cohen J. P., Gisakov M., et al.: Phys. Lett., 2, 306 (1962).

Ale84 Alekseev E. G., Guselnikov V. S., Zaitsev V. M., et al.: Radiokhimiya, 26, 667 (1984).

Ale88 Aleksandrov W. N., Semenova M. P., Semenov V. G.: At. Energ., 64, 445 (1988).

Ale90 Aleksandrov W. N., Semenova M. P., Semenov V. G.: "Cross Sections for Production of ^{7}Be by Intermediate Energy Proton Bombardment of Light-Weight Elements", VANT, (to be published).

Ale90a Aleksandrov Yu. V., Bogdanov A. I., Vasil'ev S. K., et al.: Izv. Akad. Nauk SSSR, Ser. Fiz., 54, 2249 (1990).

Ami72 Amin B. S., Biswas S., Lal D., Somayajulu B. L. K.: Nucl. Phys. A, 195, 311 (1972).

Asa85 Asano Y., Mori S., Noguchi M., et al.: J. Phys. Soc. Jpn., 54, 3734 (1985).

Asa88 Asano Y., Kariya H., Mori S., et al.: J. Phys. Soc. Jpn., 57, 2995 (1988).

Asa91 Asano Y., Mori S., Sakano M., et al.: J. Phys. Soc. Jpn., 60, 107 (1991).

Bak58 Baker E., Friedlander G., Hudis J.: Phys. Rev., 112, 1319 (1958).

Bar75 Barrandon J. N., Debrun J. L., Kohn A., Spear R. H.: Nucl. Instrum. Methods., 127, 269 (1975).

Bel54 Belmont E., Miller J. M.: Phys. Rev., 95, 54 (1954).

Ben60 Benioff P. A.: Phys. Rev., 119, 316 (1960).

Ber65 Bernas R., Epherre M., Gradsztajn E., et al.: Phys. Lett., 15, 147 (1967).

Bim71 Bimbot R., Gauvin H.: Compt. Rend., 273, 1054 (1971).

Bog76 Bogatin V. I., Litvin V. F., Lozhkin O. V., et al.: Nucl. Phys. A, 260, 446 (1976).

Bon84 Bonardi M., Birattapi C.: Int. J. Appl. Radiat. Isot., 35, 564 (1984).

Bro71 Brodzinski R. L., Wogman N. A.: Phys. Rev. C, 1, 1955 (1970).

Bro71b Brodzinski R. L., Ramcitelli L. A., Cooper J. A., Wogman N. A.: Phys. Rev. C, 4, 1257 (1971).

Car58 Caretto A. A., Wiig E. O.: Phys. Rev., 103, 236 (1958).

Cli71 Cline J. E., Nieschmidt E. B.: Nucl. Phys. A, 169, 437 (1971).

Cre63 Crespo V. P., Alexander J. M., Hyde E. K.: Phys. Rev., 131, 1765 (1963).

Cum58 Cumming J. B., Friedlander G., Swarz C. A.: Phys. Rev., 111, 1386 (1958).

Cum63c Cumming J. B.: Ann. Rev. Nucl. Part. Sci., 13 , 417 (1963).

Cum81 Cumming J. B., Agoritsas V., Witkover R.: Nucl. Instrum. Methods, 180, 37 (1981).

Dit90 Dittrich B., Herpers U., Lupke M. et al.: Radiochem. Acta, 50, 11 (1990).

Dit90a Dittrich B., Herpers U., Hoffmann H. J., et al.: Nucl. Instrum. Methods. Phys. Res. B, 52, 588 (1990).

Dos61 Dostrovsky I., Fraenkel Z., Hudis J.: Phys. Rev., 123, 1452 (1961).

Dye81 Dyer P., Bodansky D., Seamster A. G., et al.: Phys. Rev. C, 23, 1865 (1981).

Fol62 Foley K. J., Salmon G. L., Clegg A. B.: Nucl. Phys. A, 165, 405 (1971).

Fra66 Franz E. M., Freidlander G.: Nucl. Phys., 76, 123 (1966).

Fri55 Friedlander G., Hudis J., Wolfgang R. L.: Phys. Rev., 99, 263 (1955).

Fur65 Furukawa M., Kume S., Ogawa M.: Nucl. Phys., 69, 362 (1965).

Fur71 Furukawa M., Shizuri K., Komura L. A.: Nucl. Phys. A, 174, 539 (1971).

Gad74 Gadioli E., Grassistrini A. M., Lobianco G., et al.: Nuovo Cimento A, 22, 547 (1974).

Gau62 Gauvin H., Lefort M., Tarrago X.: Nucl. Phys., 39, 447 (1962).

Gru82 Grutter A.: Int. J. Appl. Radiat. Isot., 33, 725 (1982).

Gru82a Grutter A.: Nucl. Phys. A, 383, 98 (1982).

Gus62 Susakow M.: Ann. Phys., 7, 67 (1962).

Han62a Hansen L. F., Jopson R. C., Mark H., Swift C. D.: Nucl. Phys., 30, 389 (1962).

Hey76 Heydegger H. R., Garrett C. K., van Ginneken A.: Phys. Rev. C, 6, 1235 (1972).

Hic56 Hicks H. G., Stevenson P. C., Nervik W. E.: Phys. Rev., 102, 1390 (1956).

Hin52 Hintz N. W., Ramsey N. F.: Phys. Rev., 88, 19 (1952).

Hir82 Hirabayshi H., Ikeda H., Ishii H., et al.: J. Phys. Soc. Jpn., 51, 3098 (1982).

Hog78 Hogan J. J., Gadioli E.: Nuovo Cimento A, 45, 341 (1978).

Hol77 Holub R., Fowler M., Laffe L., Zellere A.: Nucl. Phys. A, 288, 291 (1977).

Hon64 Honda M., Lai D.: Nucl. Phys., 51, 363 (1964).

Hud68 Hudis J.: Phys. Rev., 171, 1301 (1968).

Hud70 Hudis J., Kristen T., Stoenner R. W., Schaeffer O. A.: Phys. Rev. C, 1, 2019 (1970).

Joh84 Johnson P. C., Lagnas-Solar M. C., Avila M. J.: Int. J. Appl. Radiat. Isot., 35, 371 (1984).

Jun87 Jung P.: J. Nucl. Matter, 144, 43 (1987).

Kau79 Kaufman S. B., Weisfield M. W., Steinberg E. P., et al.: Phys. Rev. C, 19, 962 (1979).

Kau80 Kaufman S. B., Steinberg E. P.: Phys. Rev. C, 22, 167 (1980).

Kav61 Kavanagh T. M., Bell R. E.: Can. J. Phys., 39, 1172 (1961).

Kon91 Kondratiev C. H., Kuzumenko B. A., Lobach Yu. N., et al.: At. Energ. 71, 325 (1991).

Kor67 Korteling R. G., Caretto A. A.: J. Inorg. Nucl. Chem., 29, 2863 (1967).

Kor70b Korteling R. G., Caretto A. A.: Phys. Rev. C, 1, 1960 (1970).

Kor90a Kosma P., Kliman J.: J. Phys. G, 16, 45 (1990).

Koz90b Kozma P., Damdinsuren C.: Czech. J. Phys., 40, 38 (1990).

Kru55 Kruger P., Sugarman N.: Phys. Rev., 99, 1459 (1955).

Laf66 Lafleu M. S., Porile N. T., Yaffe L.: Can. J. Chem., 44, 2749 (1966).

Lag79 Lagnas-Solar M. C., Jungermann J. A.: Int. J. Appl. Radiat. Isot., 30, 25 (1975).

Lag88 Lagnas-Solar M. C., Carvacho O. F., Cima, R. R.: Appl. Radiat. Isot., 39, 41 (1988).

Lav63 Lavrukhina A. K., Revina L. D., Malishev V. V., Satarova L. M.: JETP, 44, 1429 (1963).

Lev91 Levkovskii V. N.: "Middle Mass Nuclides (A=40 - 100) Activation Cross Sections by Medium Energy (E=10 - 50 MeV) Protons and α-Particles (Experiment and Systematics)", Inter-Vesi, Moscow, (1991).

Lig64 Ligonniere M., Vassent B., Bernas R.: Compt. Rend. B, 259, 1406 (1964).

Lup91 Lüpke M., Michel R., Dirttrich B., et al.: "Proc. Int. Conf. "Nuclear Data for Science and Technology", Jülich, 13-17 May 1991, Qaim, S., M. (ed.) , Berlin-Heidelberg-New York: Springer-Verlag, p702 (1991).

Mcc56 McCormick G. H., Blosser H. G., Cohen B. L., Newman E.: J. Inorg. Nucl. Chem., 2, 269 (1956).

Mea56 Meadows J. W., Diamond R. M., Sharp R. A.: Phys. Rev., 102, 190 (1956).

Mic79 Michel R., Brinkmann G., Weigel H., Herr W.: Nucl. Phys. A, 322, 40 (1979).

Mic80 Michel R., Brinkmann G.: J. Rad. Chem., 59, 467 (1980).

Mic85 Michel R., Peiffer F., Stück R.: Nucl. Phys. A, 441, 617 (1985).

Mic89 Michel R., Dittrich B., Herpers U.: Analyst 114, 287 (1989).

Mic95 Michel R., Gloris M., Lange H.-J., Leya I., Lüpke M., Herpers U., Dittrich-Hannen B., Rösel R., Shiekel Th., Filges D., Dragovitsch P., Suter M., Hofmann H.-J., Wölfi W., Kubik P. W., Baur H., Wieler R.: Nucl. Instr. Methods. Phys. Res. B, 103, 183 (1995).

Miy73 Miyano K.: J. Phys. Soc. Jpn., 34, 853 (1973).

Mos70 Moskalev L. P., Fedoseev G. A., Khalemsky A. N.: Yad. Fiz., 12, 871 (1970).

Moy79 Moyle R. A., Glagola B.G., Matheus G. J.: Phys. Rev. C, 19, 631 (1979).

Nag90 Nagame Y., Sueki K., Baba S., Nakahara H.: Phys. Rev. C, 41, 889 (1990).

Neu63 Neuzil E. F., Lindsay R. H.: Phys. Rev., 131, 1697 (1963).

Ort 76 Orth C. J., O'Brien H. A., Chillaci M. E., et al.: J. Inorg. Nucl. Chem., 38, 13 (1976).

Par60 Perfilov H. A., Lozhkin O. V., Shamov V. P.: Usp. Fiz. Nauk, 60, 3 (1960).

Per76 Perron C.: Phys. Rev. C14, 1108 (1976).

Por78 Porlie N. T., Dropesky B. J., Williams, R. A.: Phys. Rev. C, 18, 2231 (1978).

Pos71 Poskanzer A. M., Butler G. W., Hyde, E. K.: Phys. Rev. C, 3, 882 (1971).

Rai75b Raisbeck G. M., Yiou F.: Phys. Rev. C, 12, 915 (1975).

Rai77 Reisbeck G. M., Yiou F.: Phys. Rev. Lett., 27, 875 (1971).

Ray64 Rayudu G. V. S.: Can. J. Chem., 42, 1149 (1964).

Ray68 Rayudu G. V. S.: J. Inorg. Nucl. Chem., 30, 2311 (1968).

Ree65 Reeder P. L.: J. Inorg. Nucl. Chem., 27, 1879 (1965).

Reg82 Regnier S., Lavielle B., Simonoff F., Simonoff G. N.: Phys. Rev. C, 26, 931 (1982).

Rem63 Remsberg I. P., Miller J. M.: Phys. Rev., 130, 2069 (1963).

Rud52 Rudstam G., Stevenson P. C., Folger R. L.: Phys. Rev., 87, 358 (1952).

Rud56 Rudstam G., Thesis, University of Uppsala, 1956.

Sch79 Schoen N. C., Orlov G., Mcdonald R. J.: Phys. Rev. C, 20, 88 (1979).

Sch87 Schneider A. J., Sisterson J. M., Koehler A. M.: Nucl. Instrum. Metheods. Phys. Res. B, 29, 271 (1987).

Sha56 Sharp R. A., Diamond R. M., Wilkinson G.: Phys. Rev., 101, 1493 (1956).

Ste90 Steyn G. F., Mills S. J., Nortier F. M., et al.: Appl. Radiat. Isot., 41, 315 (1990).

Sum90 Summerer K., Bruchle W., Morrissey D. J., et al.: Phys. Rev. C, 42, 2546 (1990).

Sym57 Symonds J., Warren J., Young J.: Proc. Phys. Soc. A, 70, 824 (1957).

Tam61 Tamers M. A., Delibrias G.: Compt. Rend. B, 253, 1202 (1961).

Tan59 Tanaka S., Furukawa M.: J. Phys. Soc. Jpn., 14, 1269 (1959).

Til63 Tilbury R. S., Yaffe L.: Can. J. Chem., 41, 2634 (1963).

Val63 Valentin L., Albouy G., Cohen J. P.: Phys. Lett., 7, 163 (1963).

Val64 Valentin L.: Thesis, Institude de Physique Nucleaire, Orsay 1964.

Van60 Vandenbosch R., Huizenga J. R.: Phys. Rev., 120, 1313 (1960).

Wal73 Walton J. R., Yaniv A., Heymann D., et al.: J. Geophys. Res., 78, 6428 (1973).

Wal76 Walton J. R., Heymann D., Yaniv A., et al.: J. Geophys. Res., 81, 5689 (1976).

Yio68 Yiou F., Baril N., Citeres D., et al.: Phys. Rev., 166, 968 (1968).

Yio69 Yiou F., Seide C., Nernas R.: J. Geophys. Res., 74, 2447 (1969).

Yul60 Yule H. P., Turkevick A.: Phys. Rev., 118, 1591 (1960).

Table 1. Target nucleus and prodcued nuclides for OECD/NEA code intercomparison[13] of intermediate energy activation yields. The nuclides in parentheses are radioactive progenitors for estimating the cumulative cross sections of their daughter nuclides.

Target Nucleus	Produced Nuclides
^{16}O	^{7}Be, ^{10}Be, ^{11}C, ^{14}C
^{27}Al	^{3}H, ^{3}He, ^{4}He, ^{7}Be, ^{10}Be, ^{22}Na, ^{24}Na, ^{26}Al
^{nat}Fe	^{3}H, ^{3}He, ^{4}He, ^{7}Be, ^{10}Be, ^{20}Ne, ^{21}Ne, ^{22}Ne, ^{22}Na, ^{24}Na, ^{28}Mg, ^{26}Al, ^{36}Ar, ^{38}Ar, ^{46}Sc, ^{48}V, ^{51}Cr, $^{52m+g}Mn$, ^{53}Mn, ^{54}Mn, ^{55}Fe, ^{56}Co
^{59}Co	^{56}Co, ^{57}Co, ^{58}Co, ^{56}Ni, ^{57}Ni
^{nat}Zr	^{7}Be, ^{22}Na (^{22}Mg), ^{46}Sc, ^{48}V (^{48}Cr), ^{51}Cr (^{51}Mn, ^{51}Fe), ^{54}Mn, ^{56}Co (^{56}Ni), ^{58}Co, ^{60}Co, ^{65}Zn (^{65}Ga, ^{65}Ge), ^{67}Ga (^{67}Ge, ^{67}As), ^{69}Ge (^{69}As, ^{69}Se), ^{71}As (^{71}Se, ^{71}Br, ^{71}Kr), ^{74}As, ^{75}Se (^{75}Br, ^{75}Kr, ^{75}Rb), ^{77}Br (^{77}Kr, ^{77}Rb, ^{77}Sr), ^{78}Kr (^{78}Br, ^{78}Rb), ^{79}Kr (^{79}Rb, ^{78}Sr), ^{80}Kr (^{80}Br, ^{80}Rb, ^{80}Sr, ^{80}Y), ^{81}Kr (^{81}Rb, ^{81}Sr, ^{81}Y, ^{81}Zr), ^{82}Kr (^{82}Br, ^{82}Rb, ^{82}Sr, ^{82}Y, ^{82}Zr), ^{83}Kr (All mass 83 nuclides), ^{84}Kr (^{84}Br, ^{84}Se, ^{84}Rb), ^{85}Kr (^{85}Br, ^{85}Se), ^{86}Kr (^{86}Br, ^{86}Se, ^{86}Rb), ^{83}Rb (^{83}Sr, ^{83}Y, ^{83}Zr), ^{84}Rb, ^{86}Rb, ^{82}Sr (^{82}Y, ^{82}Zr), ^{83}Sr (^{83}Y, ^{83}Zr), ^{85}Sr (^{85}Y, ^{85}Zr, ^{85}Nb), ^{86}Y (^{86}Zr, ^{86}Nb), ^{86m}Y, ^{87}Y (^{87}Zr, ^{87}Nb), ^{87m}Y, ^{88}Y (^{88}Zr, ^{88}Nb), ^{86}Zr (^{86}Nb), ^{88}Zr (^{88}Nb), ^{89}Zr (^{89}Nb), ^{95}Zr (^{95}Y), ^{90}Nb, ^{92m}Nb, ^{95}Nb, ^{95m}Nb, ^{96}Nb

Table 1. (Continued)

Target Nucleus	Produced Nuclides
^{197}Au	^{7}Be, ^{22}Na (^{22}Mg), ^{24}Na (^{24}Ne), ^{46}Sc, ^{48}V (^{48}Cr), ^{54}Mn,^{59}Fe (^{59}Mn), ^{56}Co (^{56}Ni), ^{58}Co, ^{60}Co, ^{65}Zn (^{65}Ga, ^{65}Ge), ^{74}As, ^{75}Se (^{75}Br, ^{75}Kr, ^{75}Rb), ^{83}Rb (^{83}Sr, ^{83}Y, ^{83}Zr), ^{84}Rb, ^{86}Rb, ^{85}Sr (^{85}Y, ^{85}Zr, ^{85}Nb), ^{87}Y (^{87}Zr, ^{87}Nb), ^{88}Y (^{88}Zr, ^{88}Nb), ^{88}Zr (^{88}Nb), ^{89}Zr (^{89}Nb), ^{95}Zr (^{95}Y), ^{95}Nb (^{95}Rb, ^{95}Sr, ^{95}Y, ^{95}Zr), ^{96}Tc, ^{103}Ru (^{103}Nb, ^{103}Mo, ^{103}Tc), ^{102}Rh, ^{105}Ag (^{105}Cd, ^{105}In), ^{110m}Ag, ^{110}Ag, ^{113}Sn (^{113}Sb, ^{113}Te, ^{113}I, ^{113}Xe), ^{121}Te (^{121}I, ^{121}Xe, ^{121}Cs, ^{121}Ba), ^{121m}Te, $^{121m+g}$Te, ^{127}Xe (^{127}Cs, ^{127}Ba, ^{127}La), ^{131}Ba (^{131}La, ^{131}Ce), ^{139}Ce (^{139}Pr, ^{139}Nd, ^{139}Pm,^{139}Sm), ^{145}Eu (^{145}Gd), ^{147}Eu (^{147}Gd, ^{147}Tb), ^{148}Eu, ^{149}Eu (^{149}Gd, ^{149}Tb, ^{149}Dy, ^{149}Ho), ^{149}Gd (^{149}Tb, ^{149}Dy, ^{149}Ho), ^{151}Gd, (^{151}Tb, ^{151}Dy, ^{151}Ho), ^{153}Gd, (^{153}Tb, ^{153}Dy, ^{153}Ho), ^{149}Tb (^{149}Dy, ^{149}Ho), ^{151}Tb (^{151}Dy, ^{151}Ho), ^{153}Tb (^{153}Dy, ^{153}Ho), ^{165}Tm (^{165}Yb, ^{165}Lu, ^{165}Hf), ^{166}Tm (^{166}Yb, ^{166}Lu, ^{166}Hf, ^{166}Ta, ^{166}W), ^{167}Tm (^{167}Yb, ^{167}Hf, ^{167}Ta), ^{168}Tm, ^{166}Yb (^{166}Lu, ^{166}Hf, ^{166}Ta), ^{169}Yb (^{169}Lu, ^{169}Hf, ^{169}Ta), ^{169}Lu (^{169}Hf, ^{169}Ta), ^{170}Lu (^{170}Hf, ^{170}Ta), ^{171}Lu (^{171}Hf, ^{171}Ta), ^{172}Lu (^{172}Hf, ^{172}Ta), ^{173}Lu (^{173}Hf, ^{173}Ta), ^{172}Hf (^{172}Ta, ^{172}W, ^{172}Re), ^{173}Hf (^{173}Ta, ^{173}W), ^{175}Hf (^{175}Ta, ^{175}Re, ^{175}Qs), ^{181}Re (^{181}Qs, ^{181}Ir), ^{182}Re (^{182}Qs, ^{182}Ir, ^{182}Pt), ^{183}Re (^{183}Qs, ^{183}Ir, ^{183}Pt, ^{183}Au), ^{182}Qs (^{182}Ir, ^{182}Pt, ^{182}Au, ^{182}Hg), ^{185}Qs (^{185}Ir, ^{185}Pt, ^{185}Au, ^{185}Hg), ^{191}Qs (^{191}Re), ^{185}Ir (^{185}Pt, ^{185}Au, ^{185}Hg), ^{186}Ir (^{186}Pt, ^{186}Au, ^{186}Hg), ^{187}Ir (^{187}Pt, ^{187}Au, ^{187}Hg), ^{188}Ir (^{188}Pt, ^{188}Au, ^{188}Hg), ^{189}Ir (^{189}Pt, ^{189}Au, ^{189}Hg), ^{190}Ir, ^{192}Ir, ^{188}Pt (^{188}Au, ^{188}Hg), ^{191}Pt (^{191}Au, ^{191}Hg), ^{193}Au (^{193}Hg), ^{194}Au (^{194}Hg), ^{195}Au (^{195}Hg), ^{196}Au, ^{193}Hg, ^{194}Hg, ^{195}Hg, ^{195m}Hg, ^{197}Hg, ^{197m}Hg

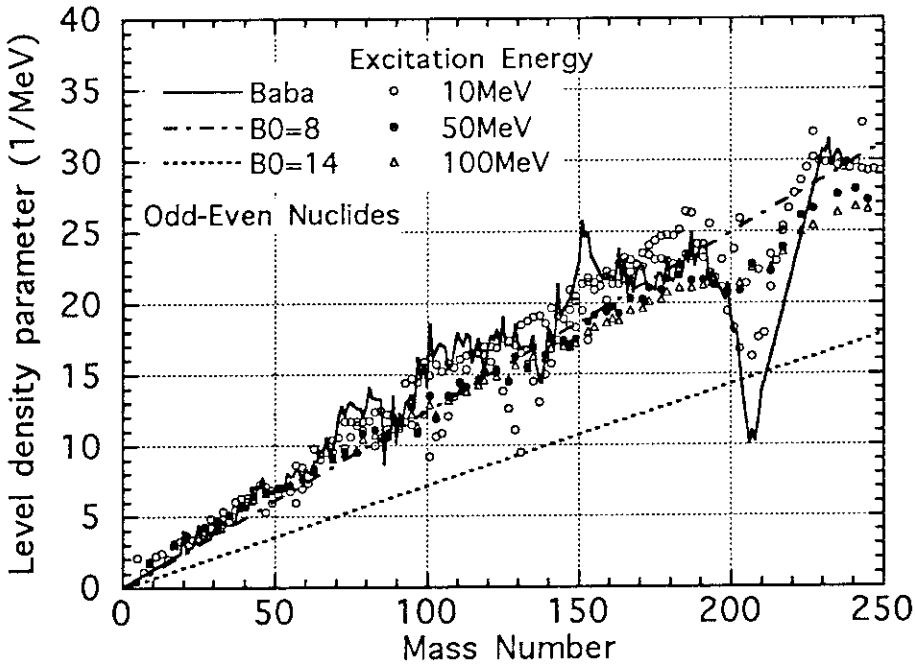

Fig. 1 Level density parameters for odd-even nuclides. The open circle, solid circle and open triangle represent the level density parameters of Ignatyuk[22] for the excitation energies of 10, 50 and 100 MeV, respectively. The solid line indicates the level density parameter derived by Baba[21]. The dot-dashed and dotted lines stand for those obtained by the function of the mass number, A, as A/8 and A/14, respectively.

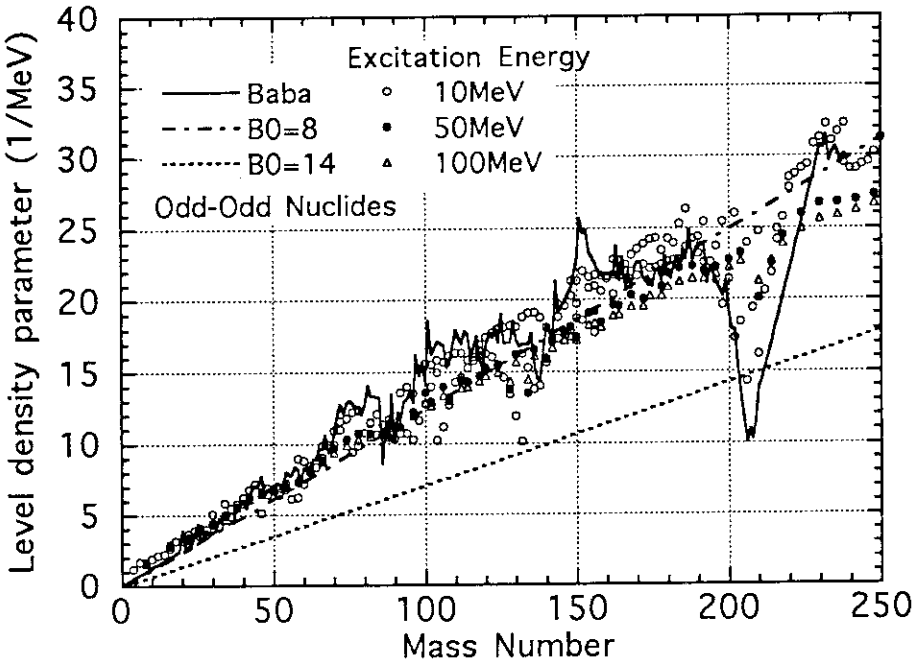

Fig. 2 Level density parameters for odd-odd nuclides. The notes to the marks and lines are the same as for Fig. 1.

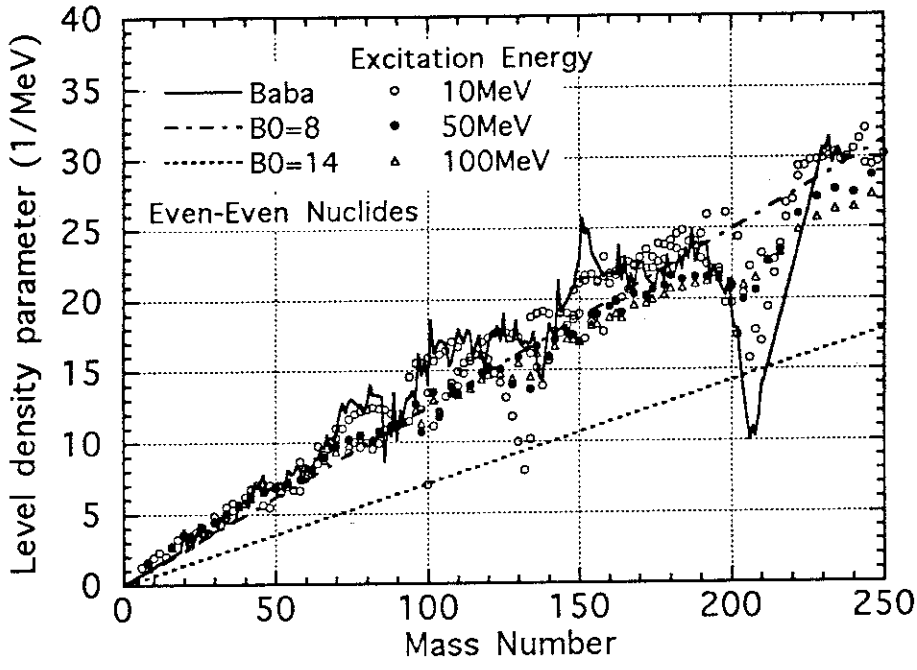

Fig. 3 Level density parameters for even-even nuclides. The notes to the marks and lines are the same as for Fig. 1.

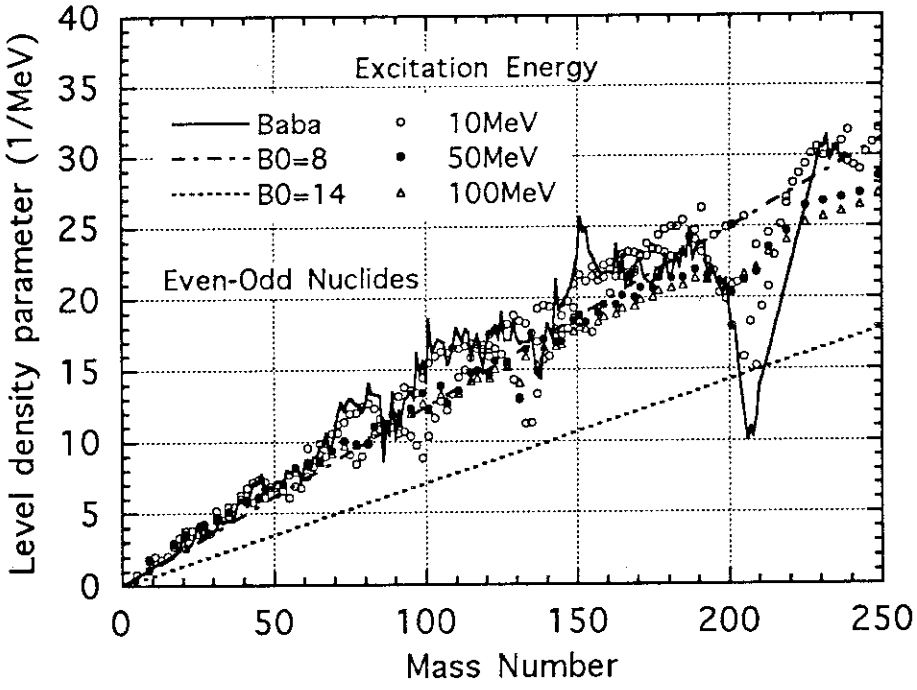

Fig. 4 Level density parameters for even-odd nuclides. The notes to the marks and lines are the same as for Fig. 1.

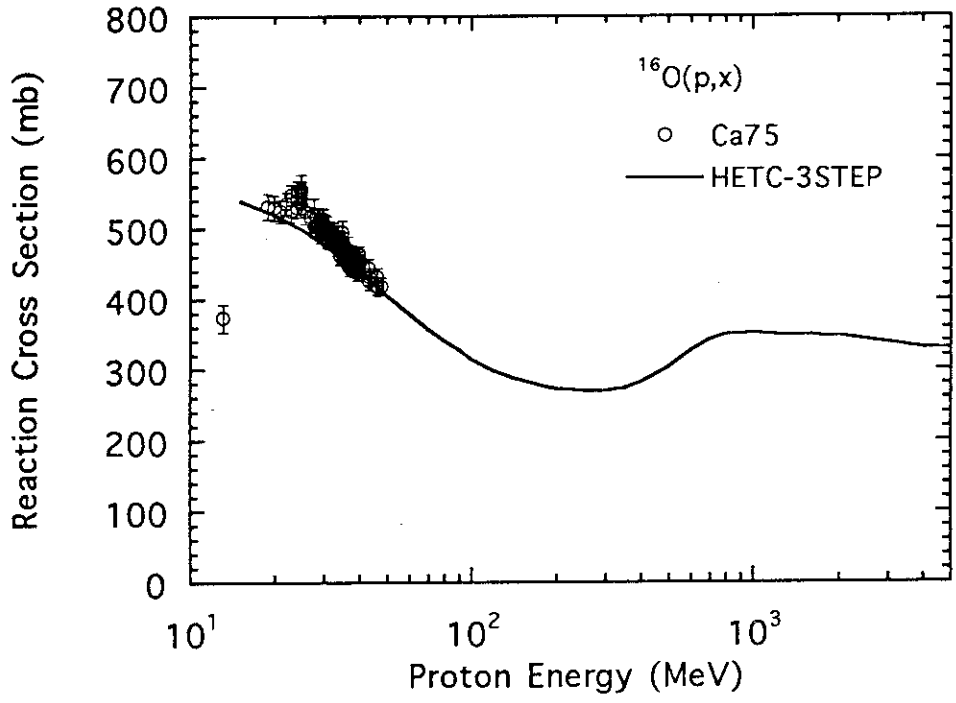

Fig. 5 Reaction cross section of the $^{16}O(p,x)$ reaction. The marks represent the experimental data[28]. The solid line indicates the calculated result of HETC-3STEP. The sources of the experimental data are listed in Appendix I.

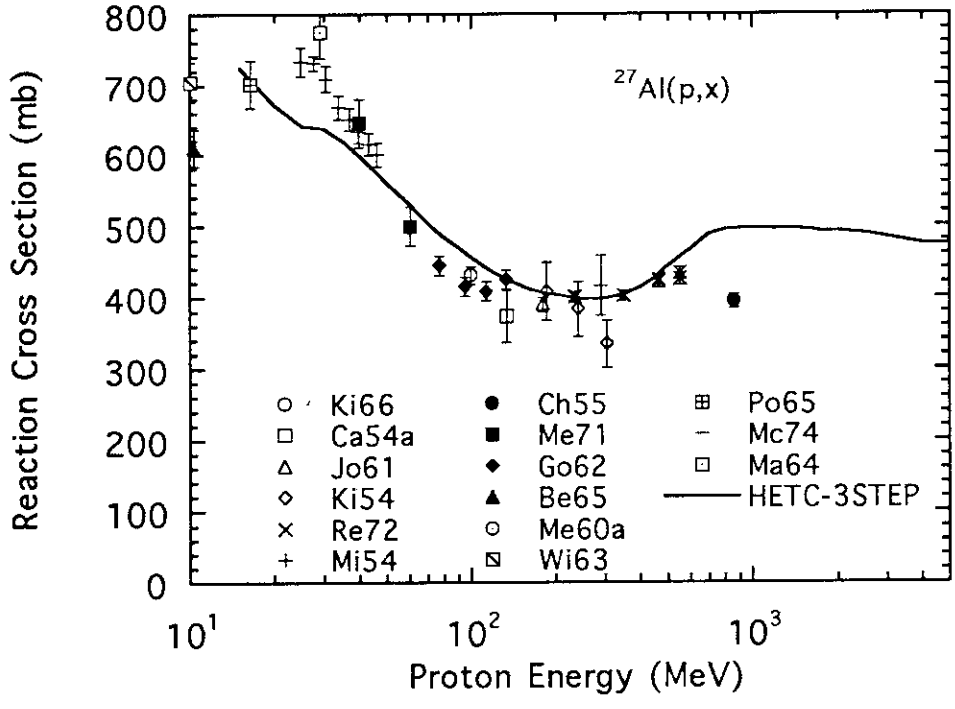

Fig. 6 Reaction cross section of the $^{27}Al(p,x)$ reaction. The notes to the marks and line are the same as for Fig. 5.

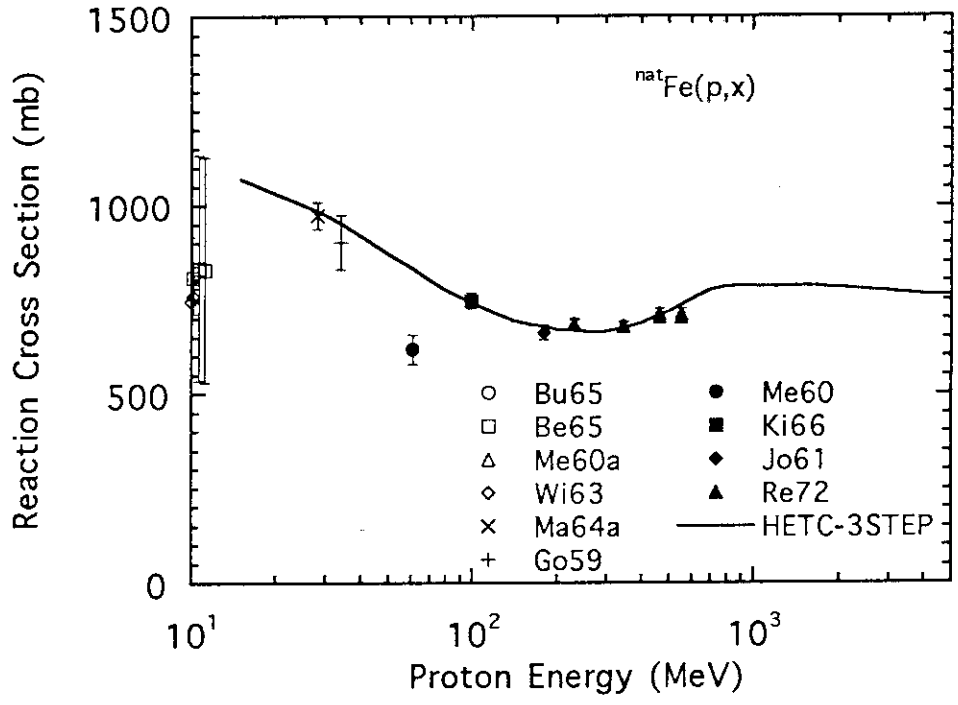

Fig. 7 Reaction cross section of the ^{nat}Fe(p, x) reaction. The notes to the marks and line are the same as for Fig. 5.

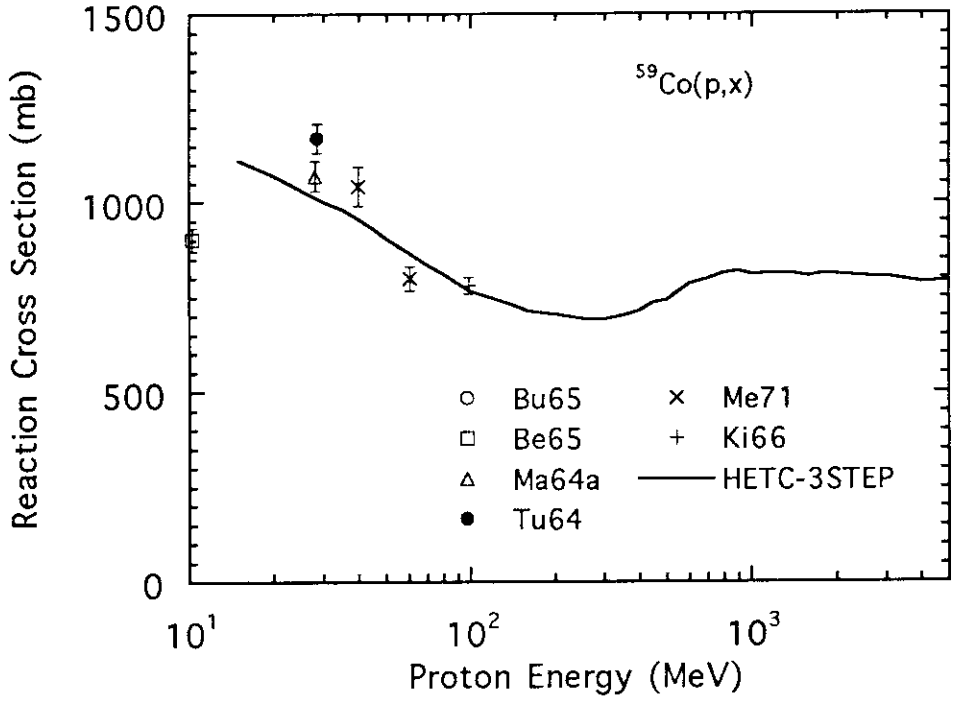

Fig. 8 Reaction cross section of the ^{59}Co(p, x) reaction. The notes to the marks and line are the same as for Fig. 5.

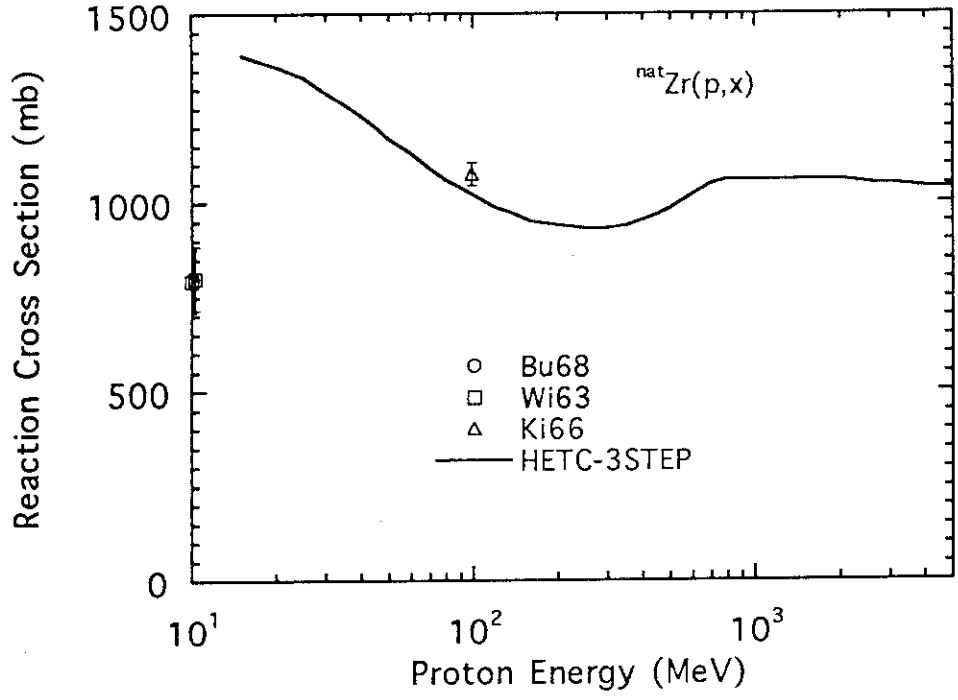

Fig. 9 Reaction cross section of the ^{nat}Zr(p, x) reaction. The notes to the marks and line are the same as for Fig. 5.

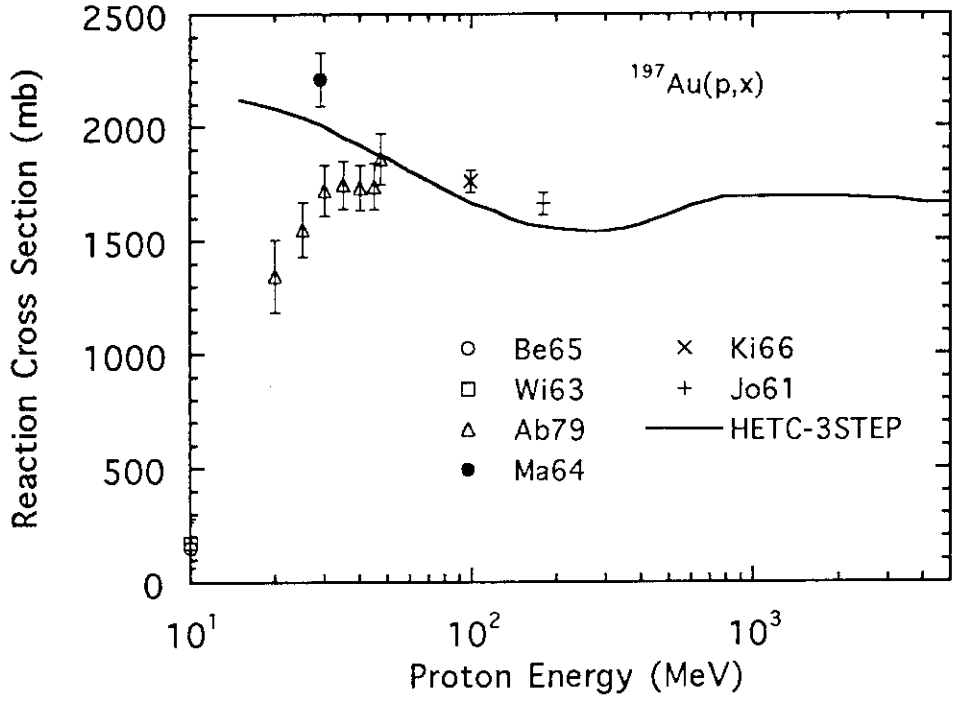

Fig. 10 Reaction cross section of the ^{197}Au(p, x) reaction. The notes to the marks and line are the same as for Fig. 5.

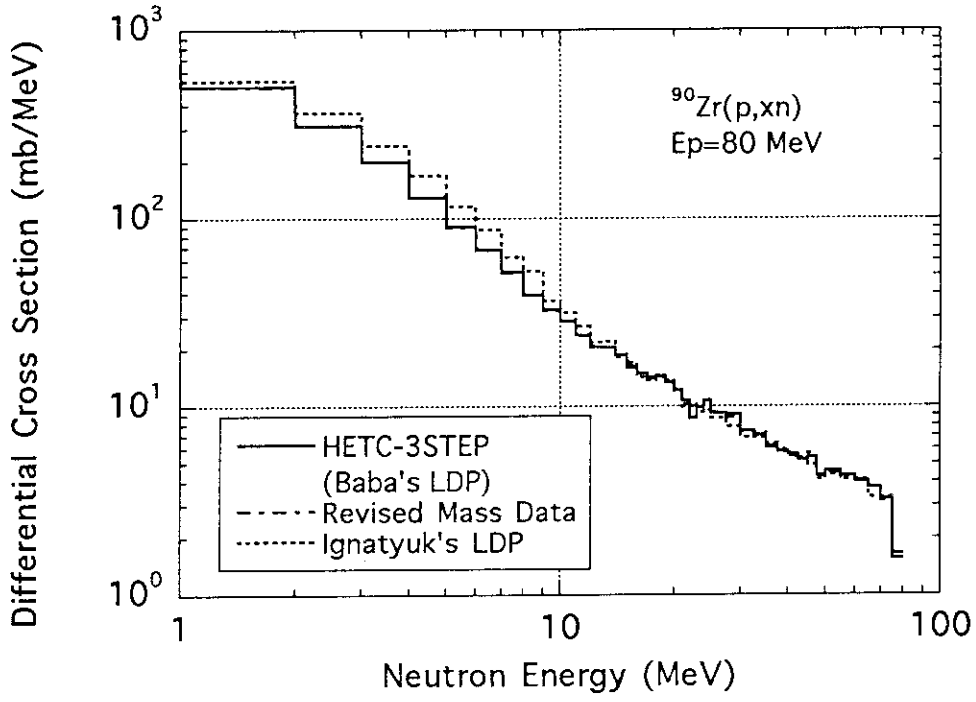

Fig. 11 Differential cross section of the ^{90}Zr(p, xn) reaction for the 80 MeV proton incidence. The solid line indicates the calculated result of HETC-3STEP using the level density parameter derived by Baba[21]. The dot-dashed line represents the one using revised mass data of Audi and Wapstra[26] with the level density parameter of Baba. The dotted line stands for the one using the level density parameter derived by Ignatyuk[22].

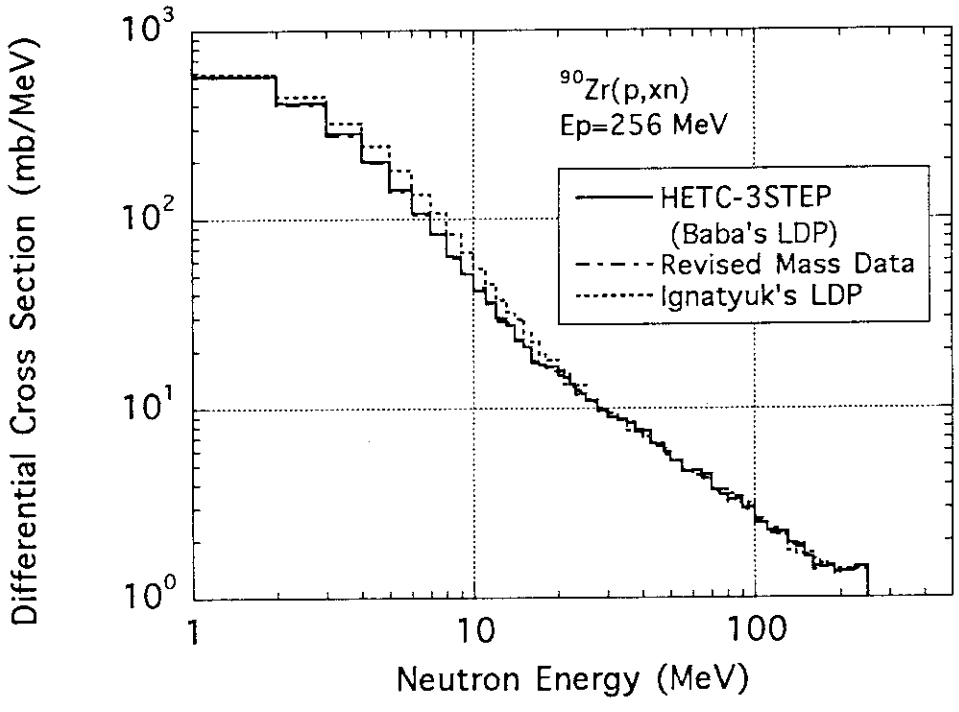

Fig. 12 Differential cross section of the ^{90}Zr(p, xn) reaction for the 256 MeV proton incidence. The notes to the lines are the same as for Fig. 11.

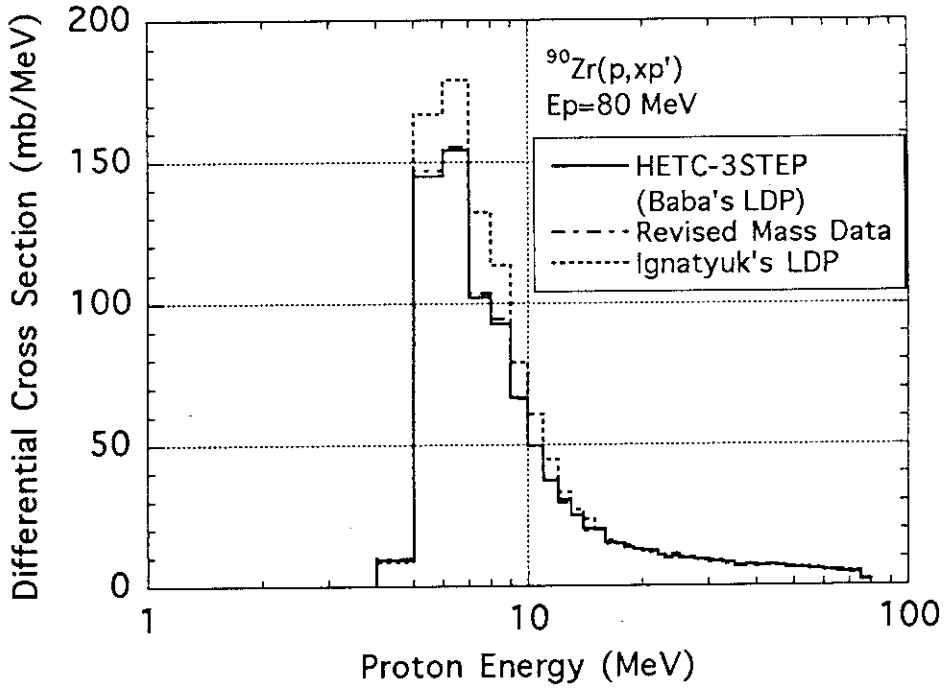

Fig. 13 Differential cross section of the ^{90}Zr(p, xp') reaction for the 80 MeV proton incidence. The notes to the lines are the same as for Fig. 11.

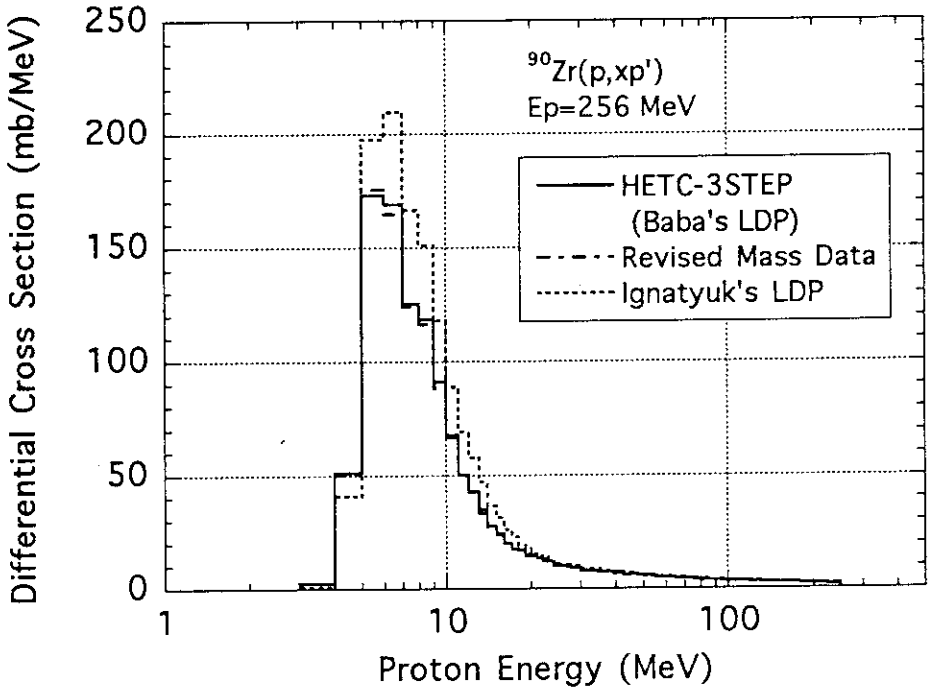

Fig. 14 Differential cross section of the ^{90}Zr(p, xp') reaction for the 256 MeV proton incidence. The notes to the lines are the same as for Fig. 11.

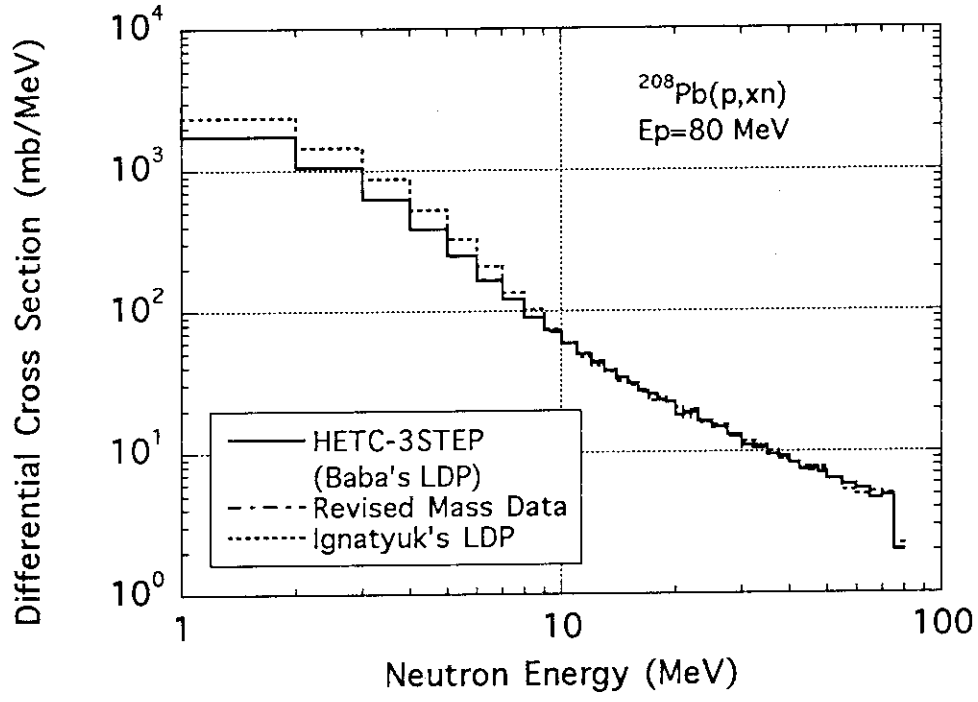

Fig. 15 Differential cross section of the ^{208}Pb(p, xn) reaction for the 80 MeV proton incidence. The notes to the lines are the same as for Fig. 11.

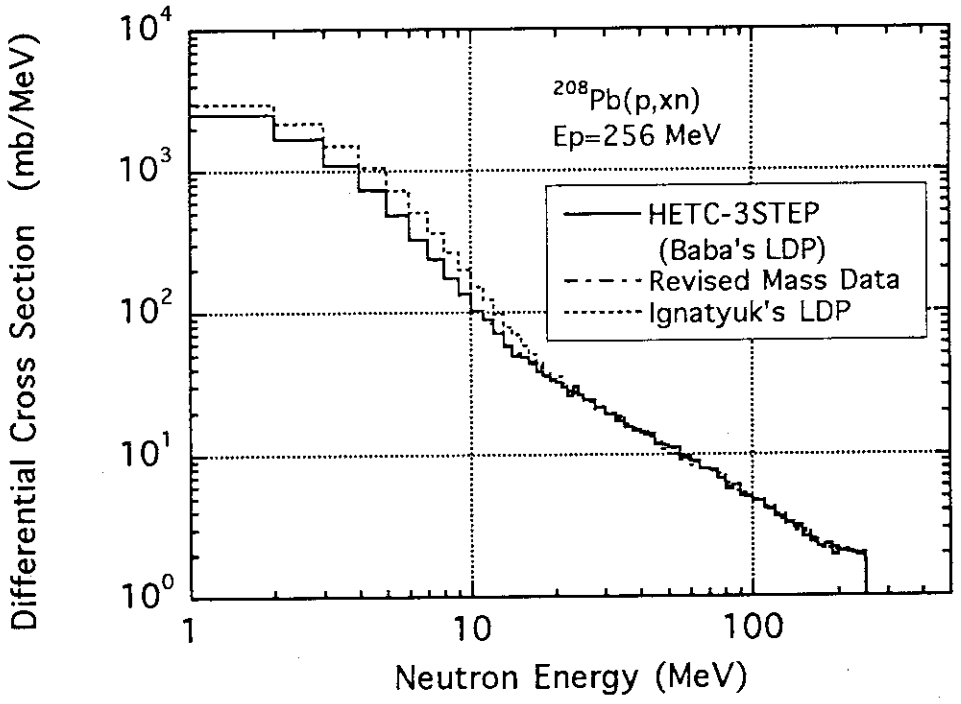

Fig. 16 Differential cross section of the ^{208}Pb(p, xn) reaction for the 256 MeV proton incidence. The notes to the lines are the same as for Fig. 11.

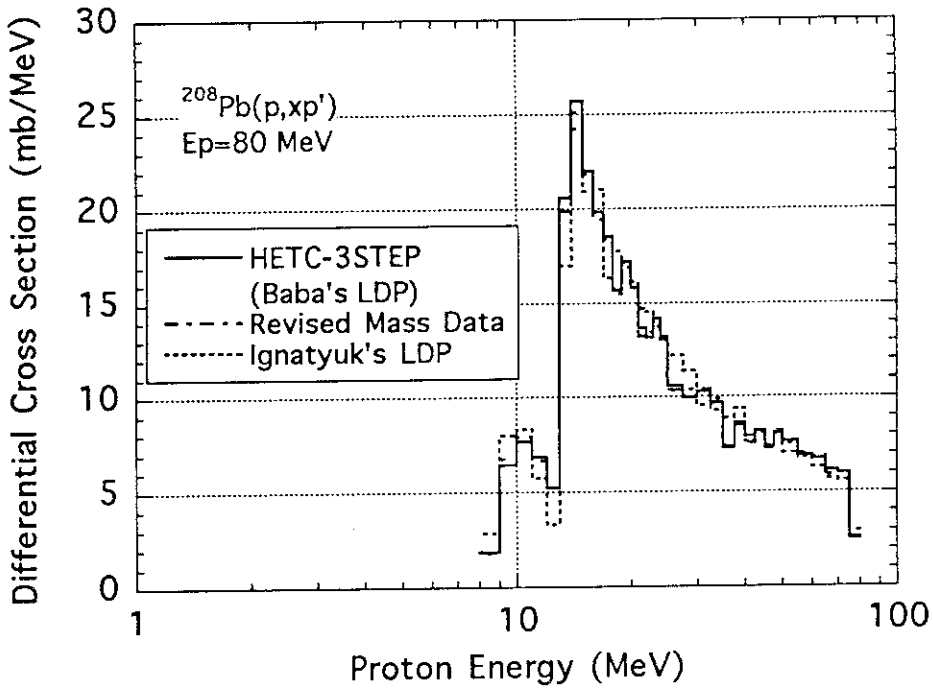

Fig. 17 Differential cross section of the ^{208}Pb(p, xp') reaction for the 80 MeV proton incidence. The notes to the lines are the same as for Fig. 11.

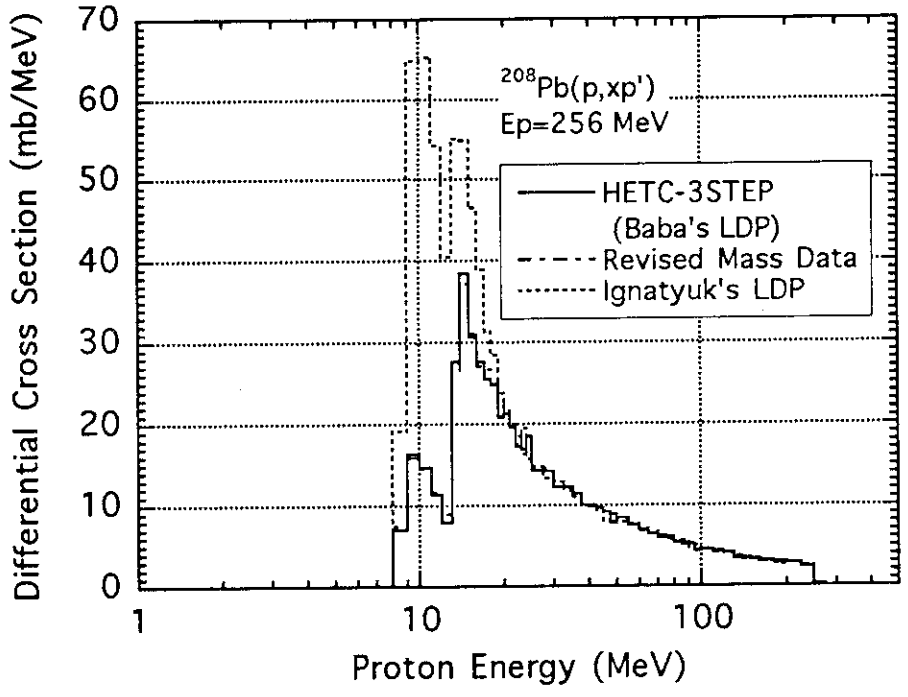

Fig. 18 Differential cross section of the ^{208}Pb(p, xp') reaction for the 256 MeV proton incidence. The notes to the lines are the same as for Fig. 11.

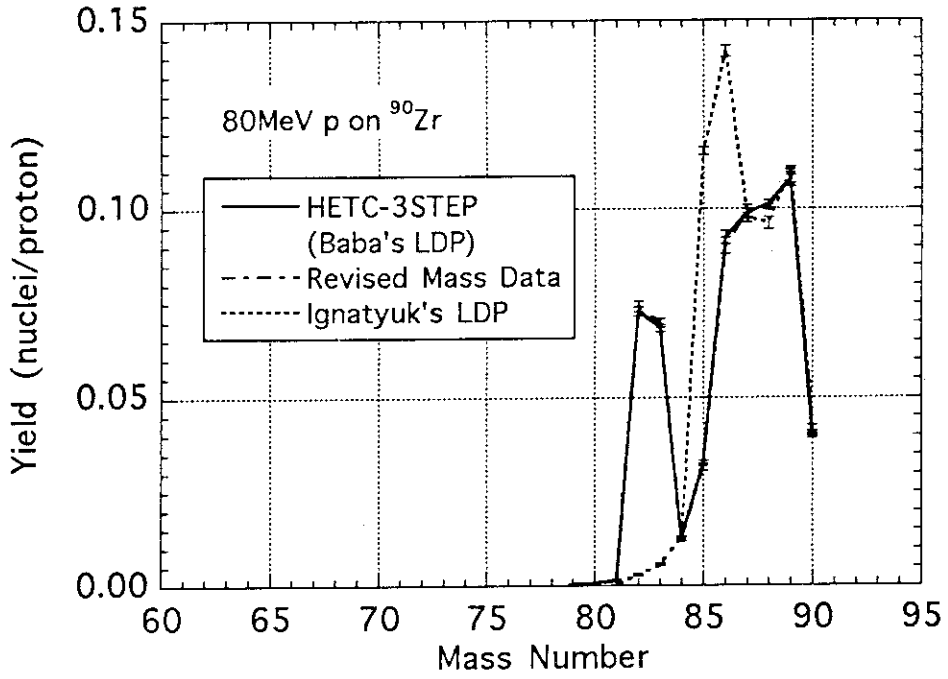

Fig. 19 Mass yield distribution on the ^{90}Zr target for the 80 MeV proton incidence. The notes to the lines are the same as for Fig. 11.

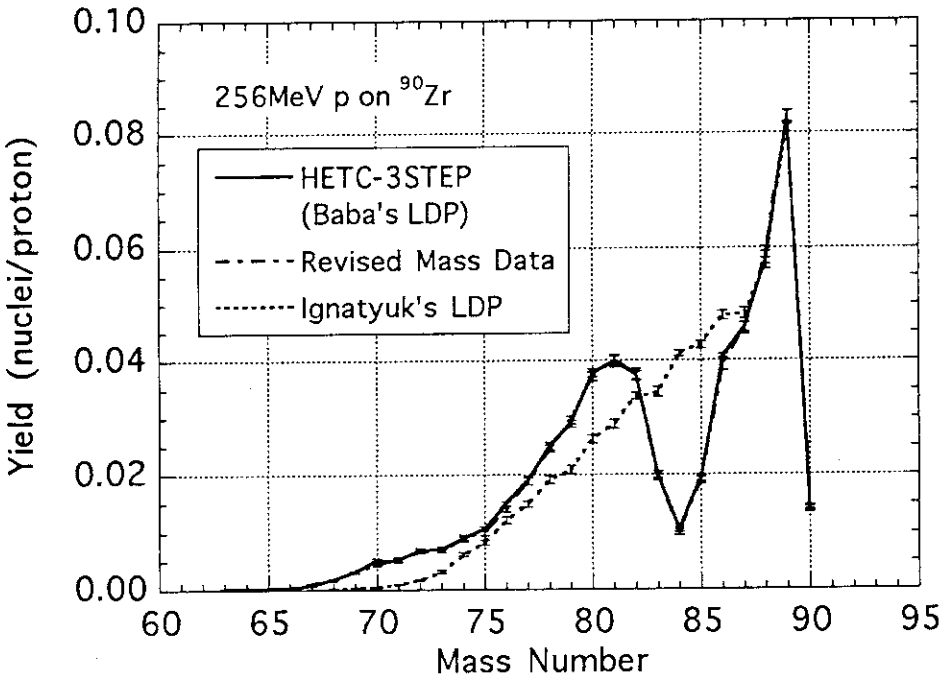

Fig. 20 Mass yield distribution on the ^{90}Zr target for the 256 MeV proton incidence. The notes to the lines are the same as for Fig. 11.

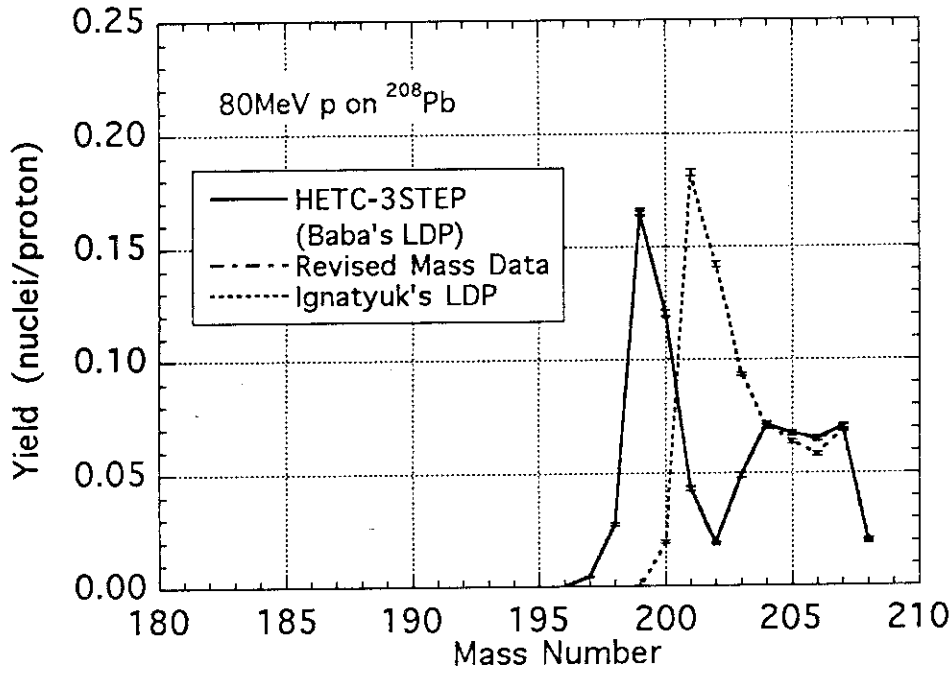

Fig. 21 Mass yield distribution on the ^{208}Pb target for the 80 MeV proton incidence. The notes to the lines are the same as for Fig. 11.

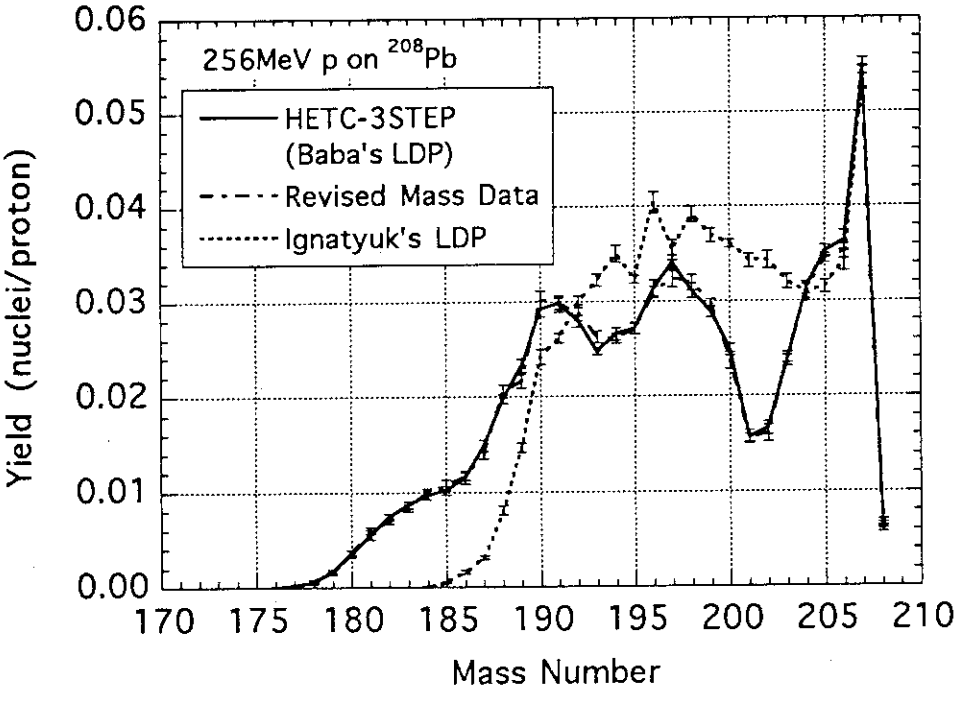

Fig. 22 Mass yield distribution on the ^{208}Pb target for the 256 MeV proton incidence. The notes to the lines are the same as for Fig. 11.

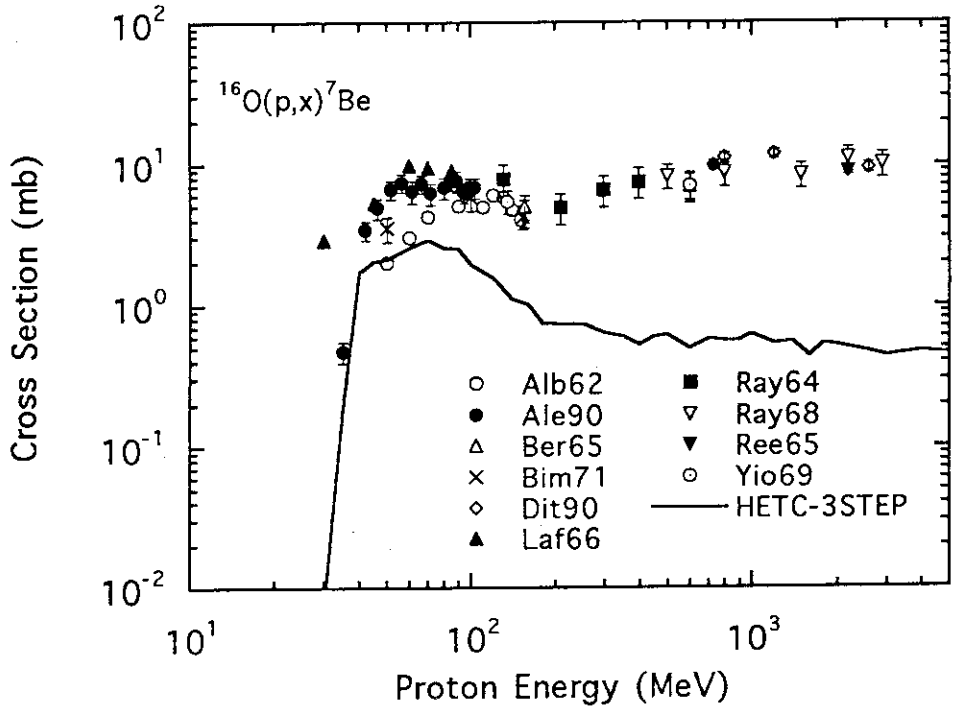

Fig. 23 Cross section of the $^{16}O(p, x)^{7}Be$ reaction. The marks represent the experimental data[29-32]. The solid line indicates the calculated result of HETC-3STEP. The sources of the experimental data are listed in Appendix II.

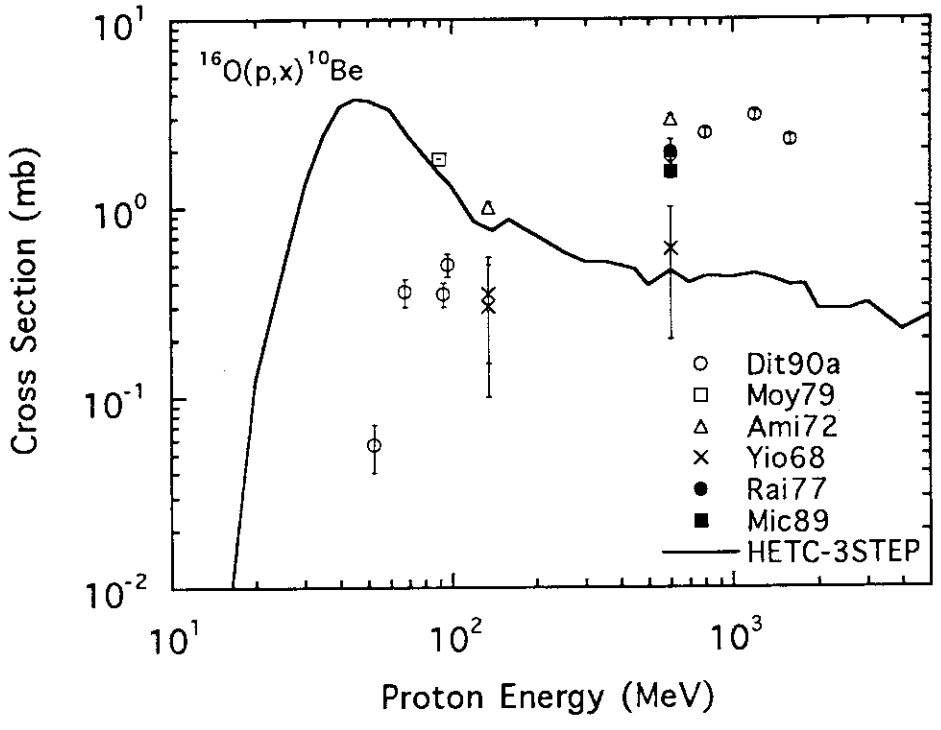

Fig. 24 Cross section of the $^{16}O(p, x)^{10}Be$ reaction. The notes to the marks and line are the same as for Fig. 23.

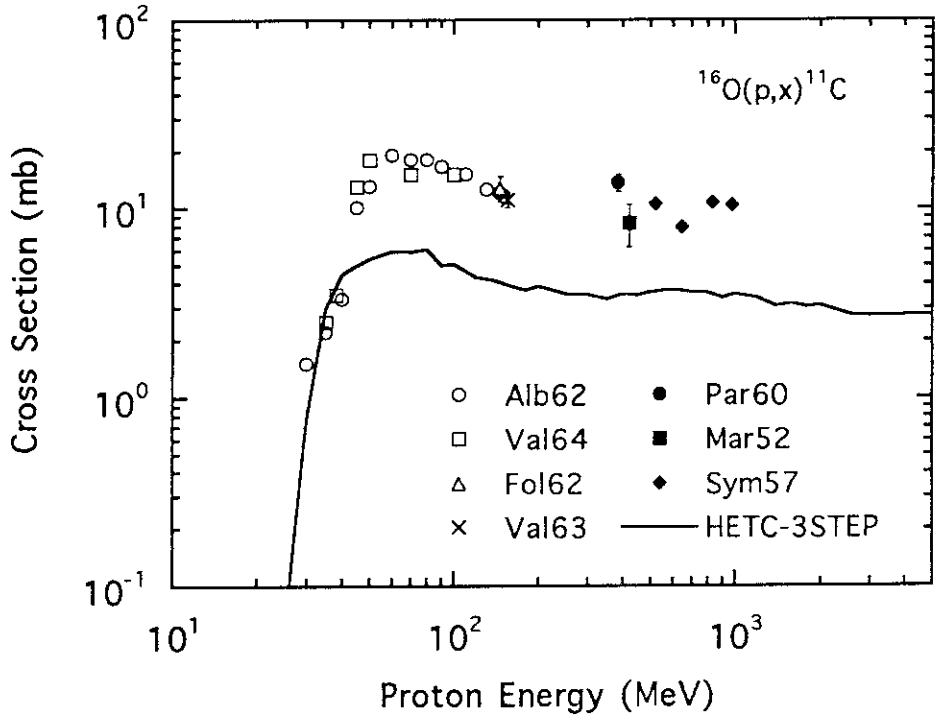

Fig. 25 Cross section of the $^{16}O(p, x)^{11}C$ reaction. The notes to the marks and line are the same as for Fig. 23.

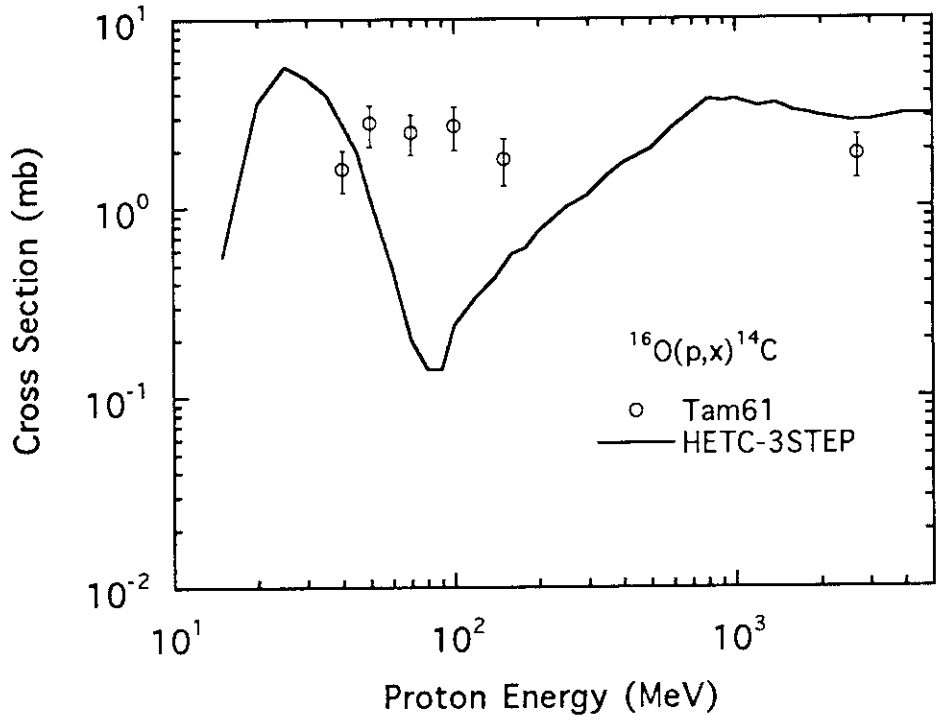

Fig. 26 Cross section of the $^{16}O(p, x)^{14}C$ reaction. The notes to the marks and line are the same as for Fig. 23.

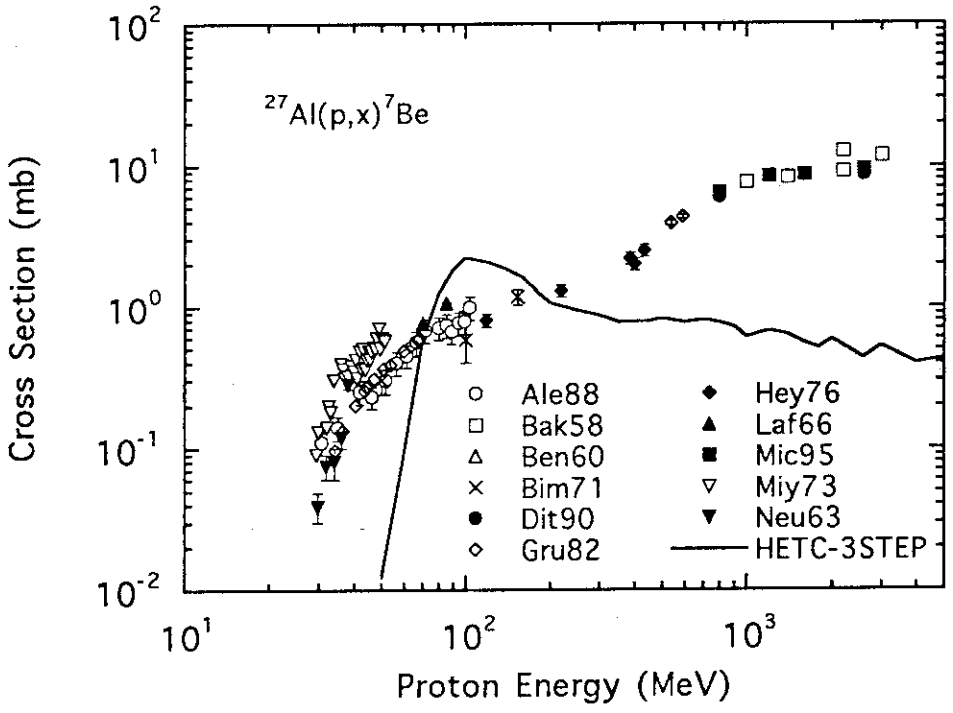

Fig. 27 Cross section of the ^{27}Al(p, x)^{7}Be reaction. The notes to the marks and line are the same as for Fig. 23.

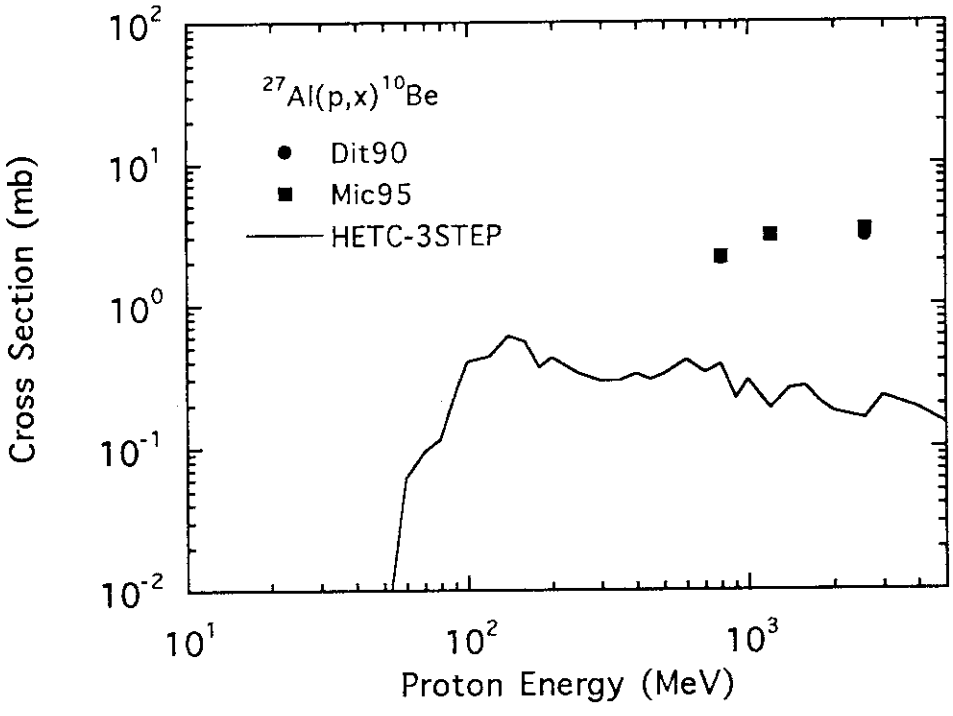

Fig. 28 Cross section of the ^{27}Al(p, x)^{10}Be reaction. The notes to the marks and line are the same as for Fig. 23.

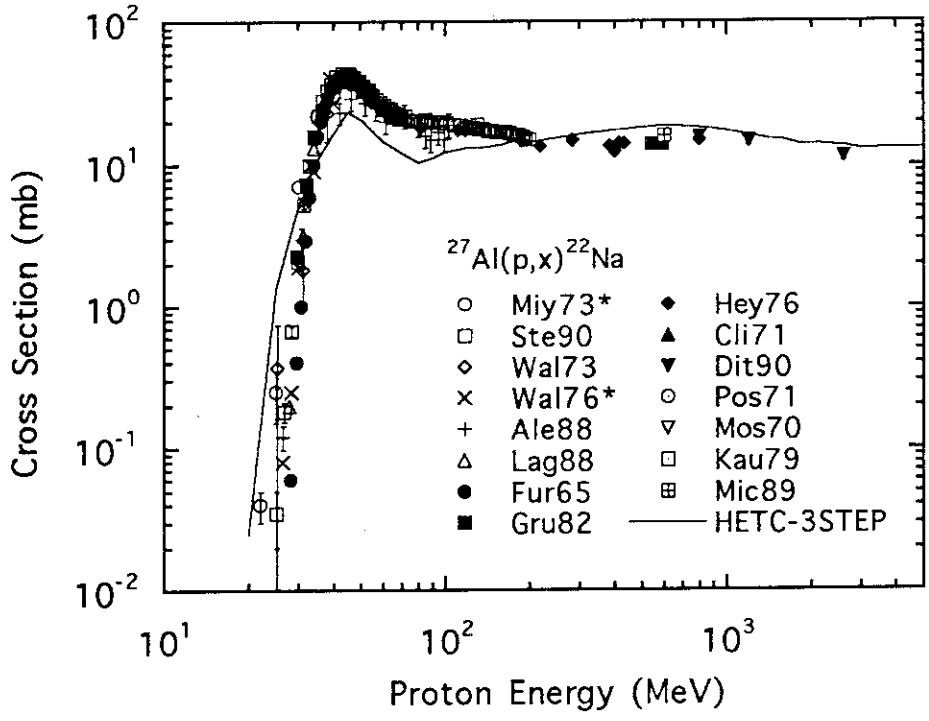

Fig. 29 Cross section of the ^{27}Al(p, x)^{22}Na reaction. The notes to the marks and line are the same as for Fig. 23.

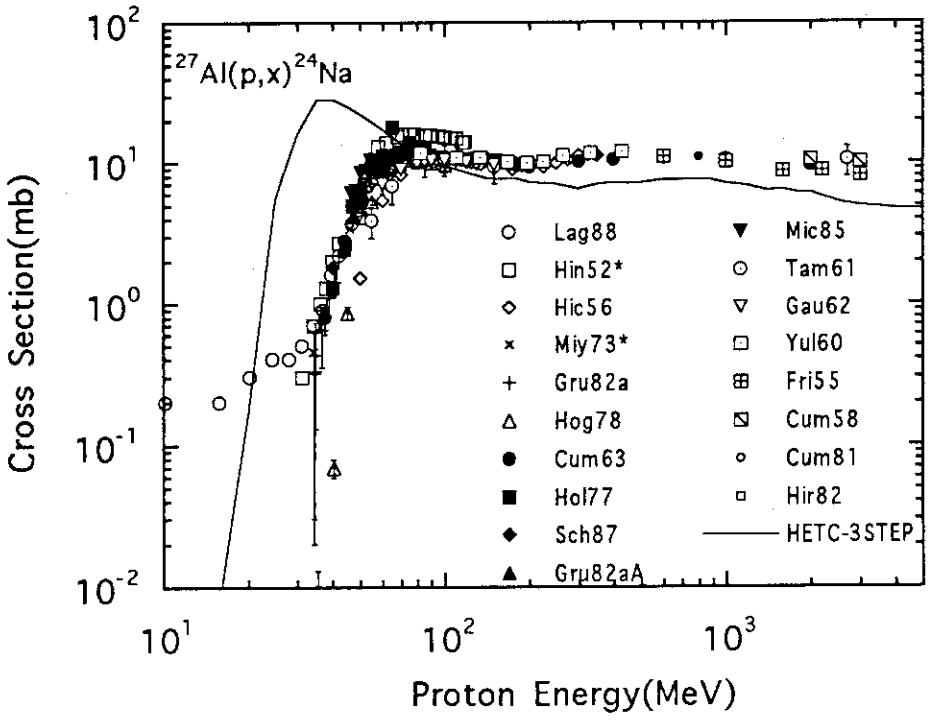

Fig. 30 Cross section of the ^{27}Al(p, x)^{24}Na reaction. The notes to the marks and line are the same as for Fig. 23.

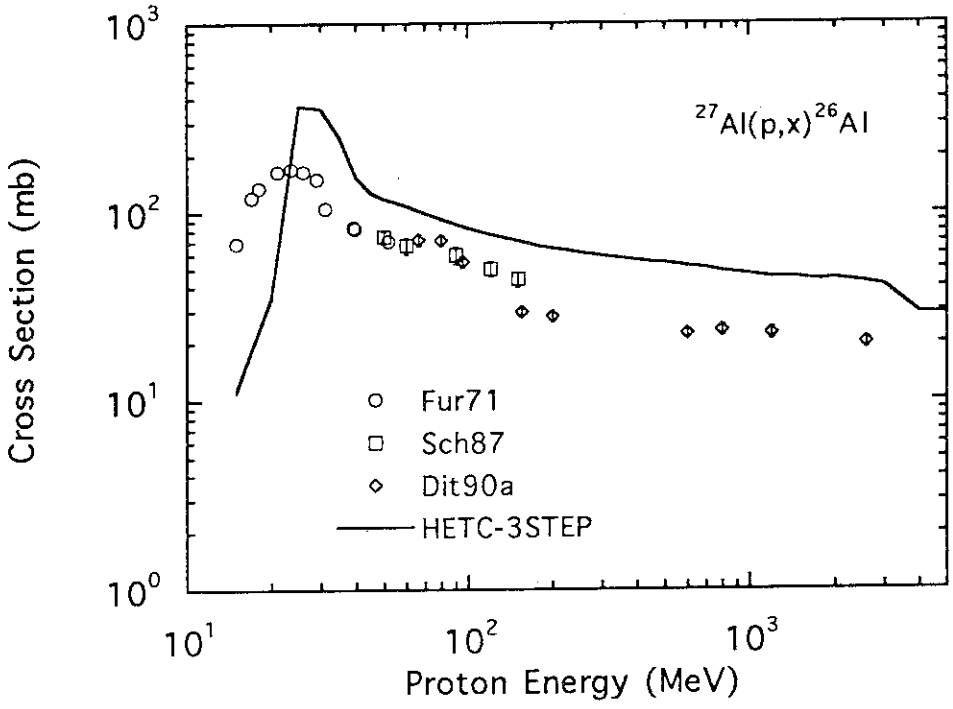

Fig. 31 Cross section of the ^{27}Al(p, x)^{26}Al reaction. The notes to the marks and line are the same as for Fig. 23.

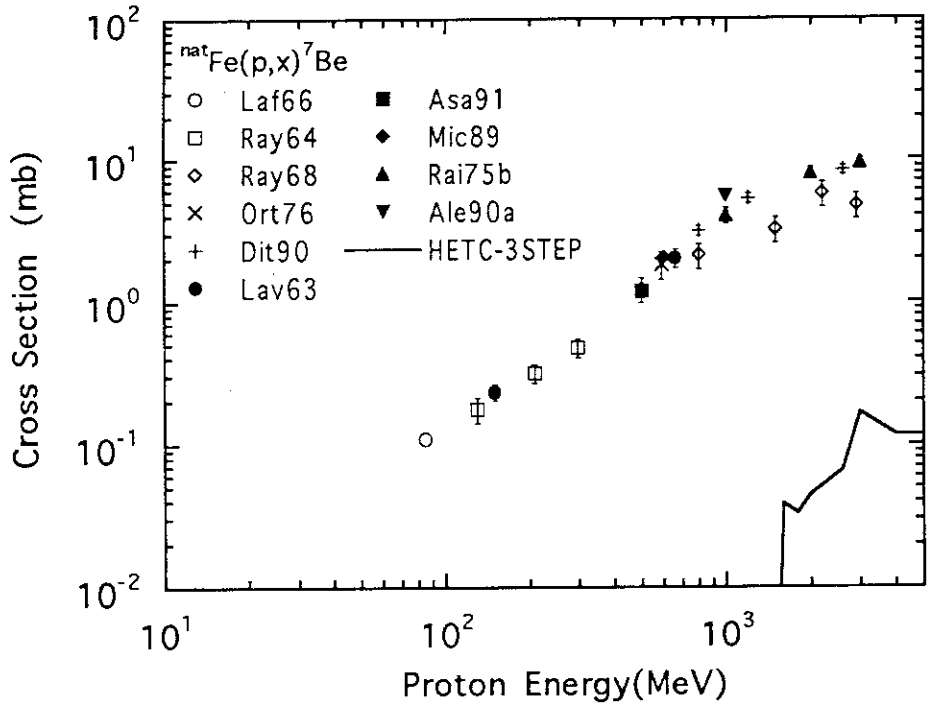

Fig. 32 Cross section of the ^{nat}Fe(p, x)^{7}Be reaction. The notes to the marks and line are the same as for Fig. 23.

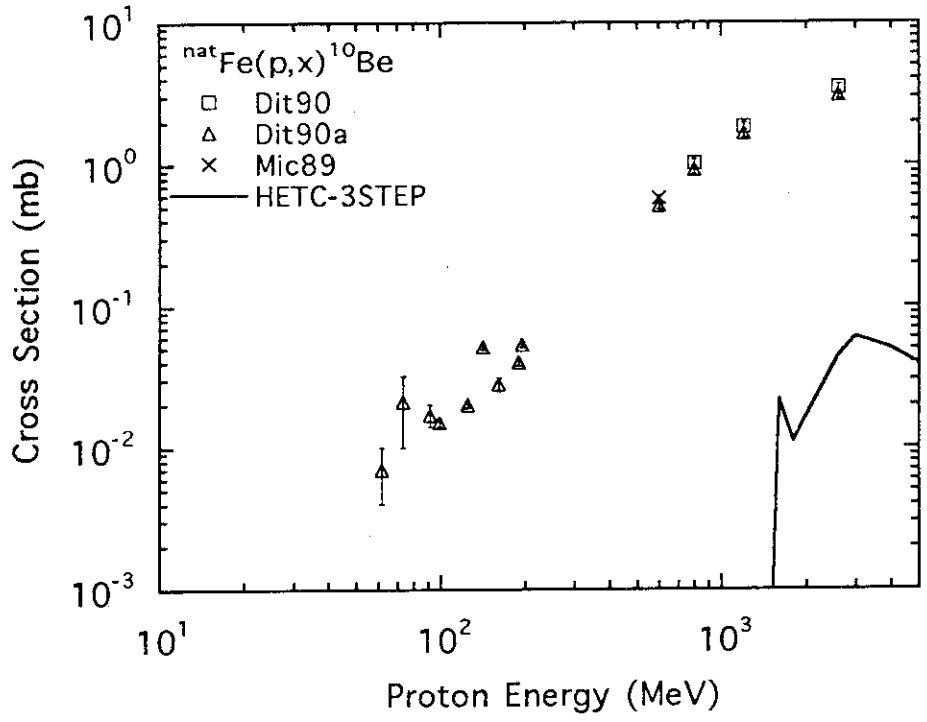

Fig. 33 Cross section of the ^{nat}Fe(p, x)^{10}Be reaction. The notes to the marks and line are the same as for Fig. 23.

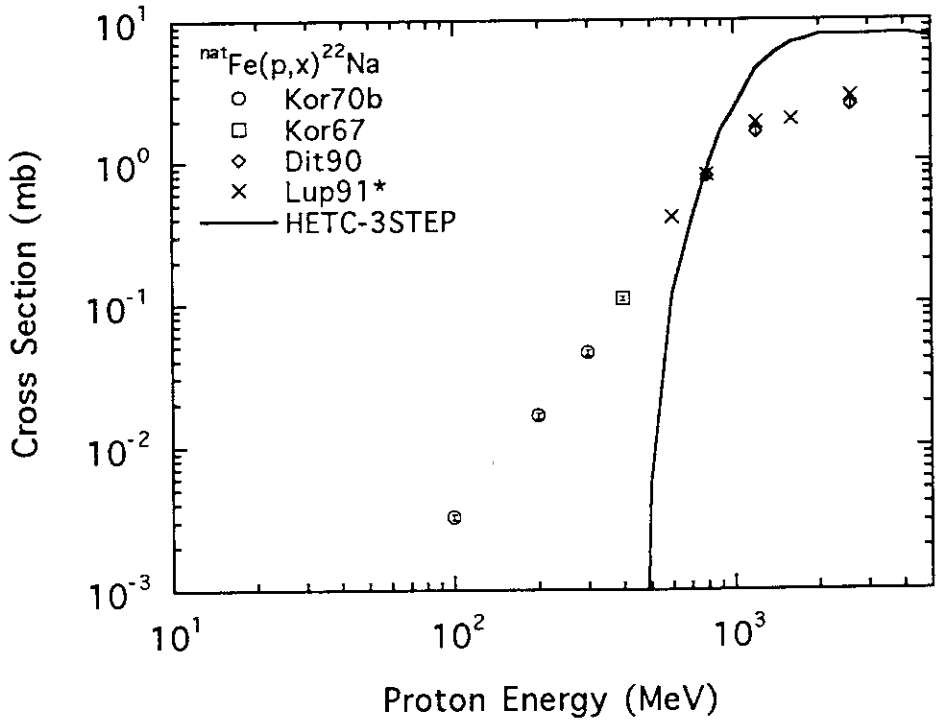

Fig. 34 Cross section of the ^{nat}Fe(p, x)^{22}Na reaction. The notes to the marks and line are the same as for Fig. 23.

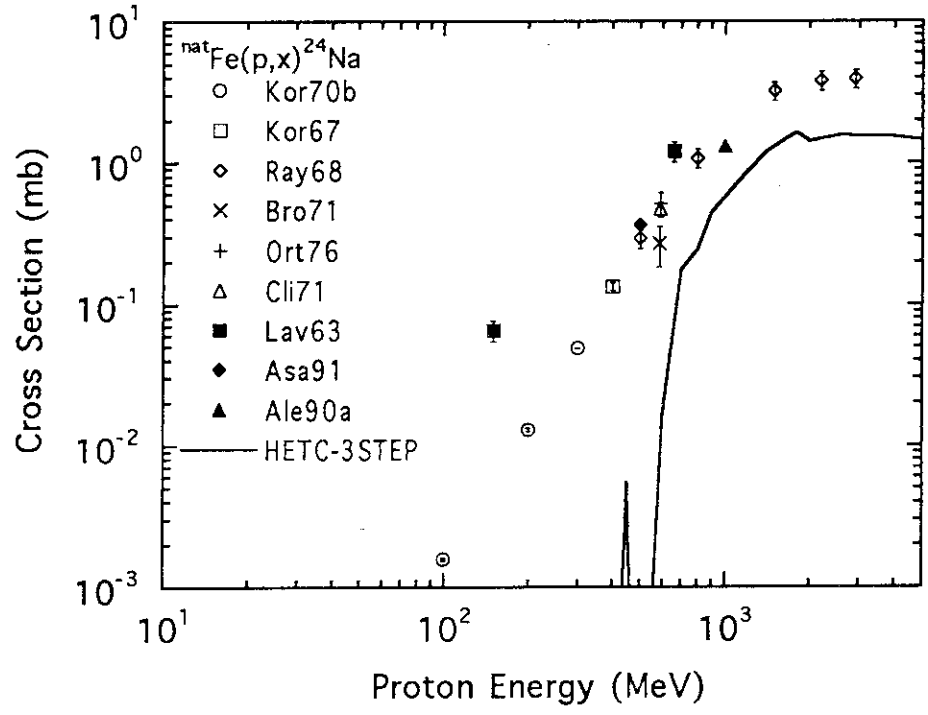

Fig. 35 Cross section of the ^{nat}Fe(p, x)^{24}Na reaction. The notes to the marks and line are the same as for Fig. 23.

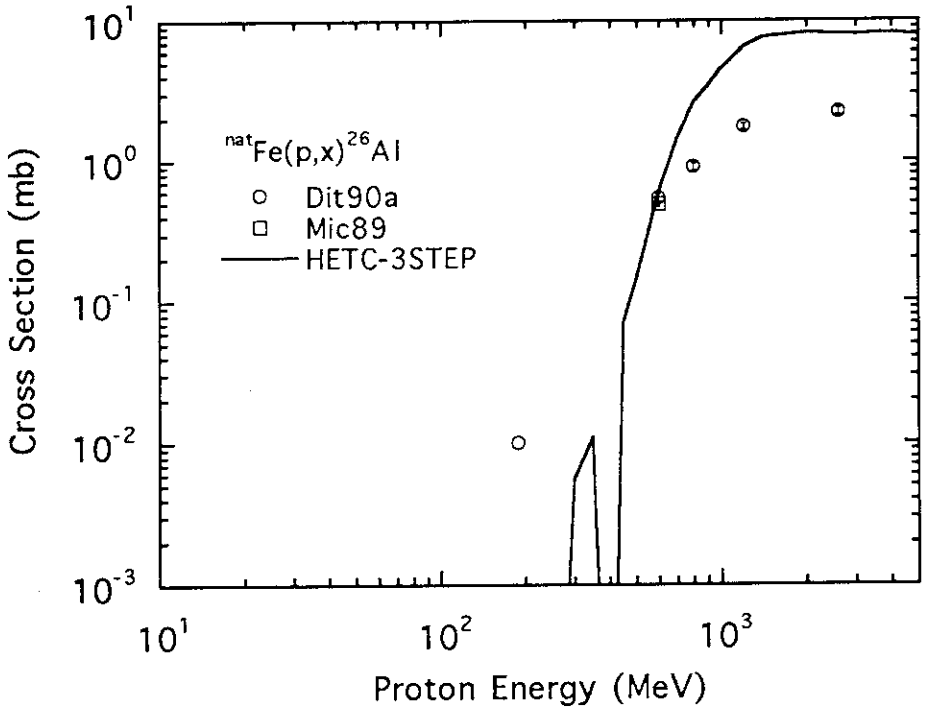

Fig. 36 Cross section of the ^{nat}Fe(p, x)^{26}Al reaction. The notes to the marks and line are the same as for Fig. 23.

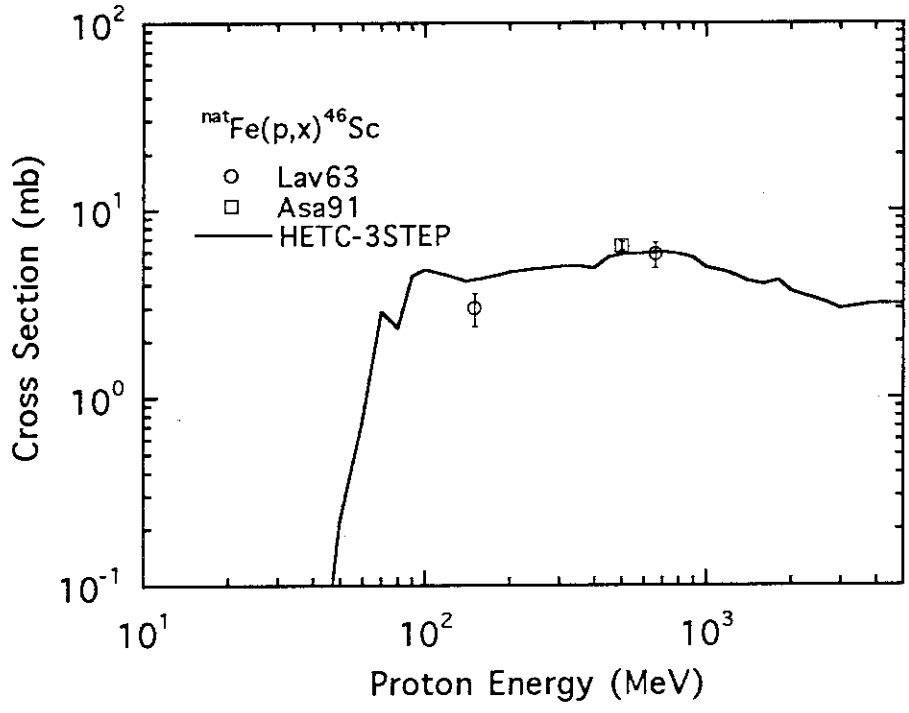

Fig. 37 Cross section of the ^{nat}Fe(p, x)^{46}Sc reaction. The notes to the marks and line are the same as for Fig. 23.

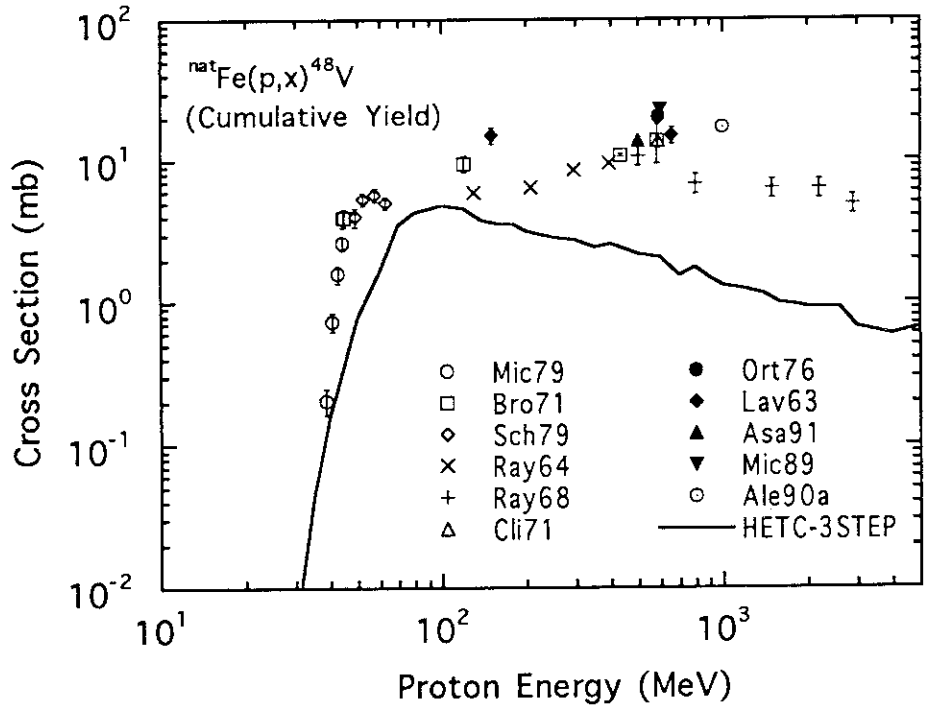

Fig. 38 Cumulative cross section of the ^{nat}Fe(p, x)^{48}V reaction. The notes to the marks and line are the same as for Fig. 23.

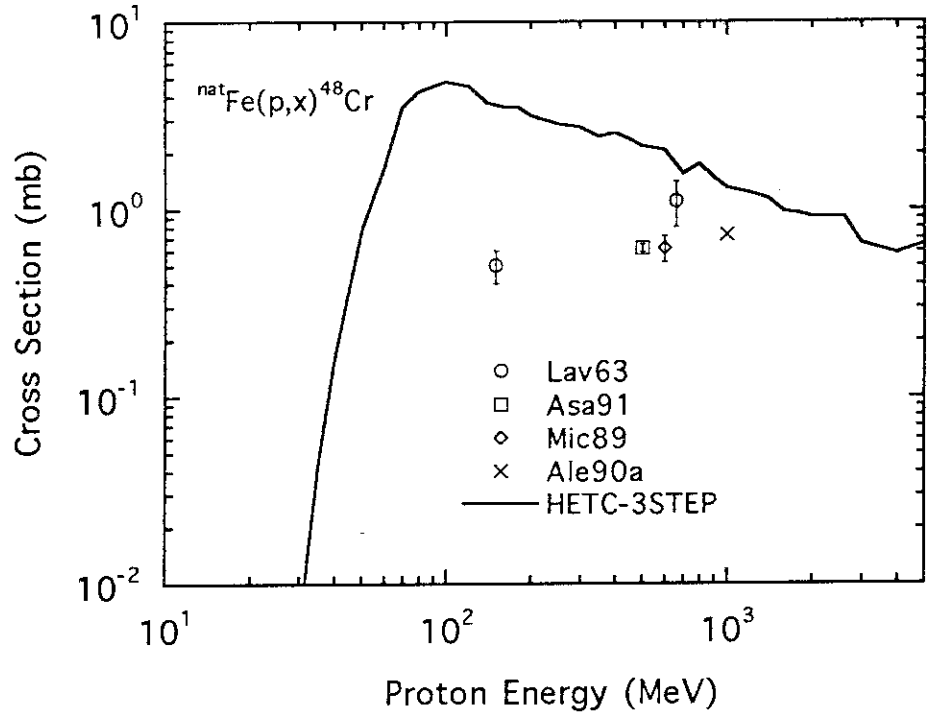

Fig. 39 Cross section of the ^{nat}Fe(p, x)^{48}Cr reaction. The notes to the marks and line are the same as for Fig. 23.

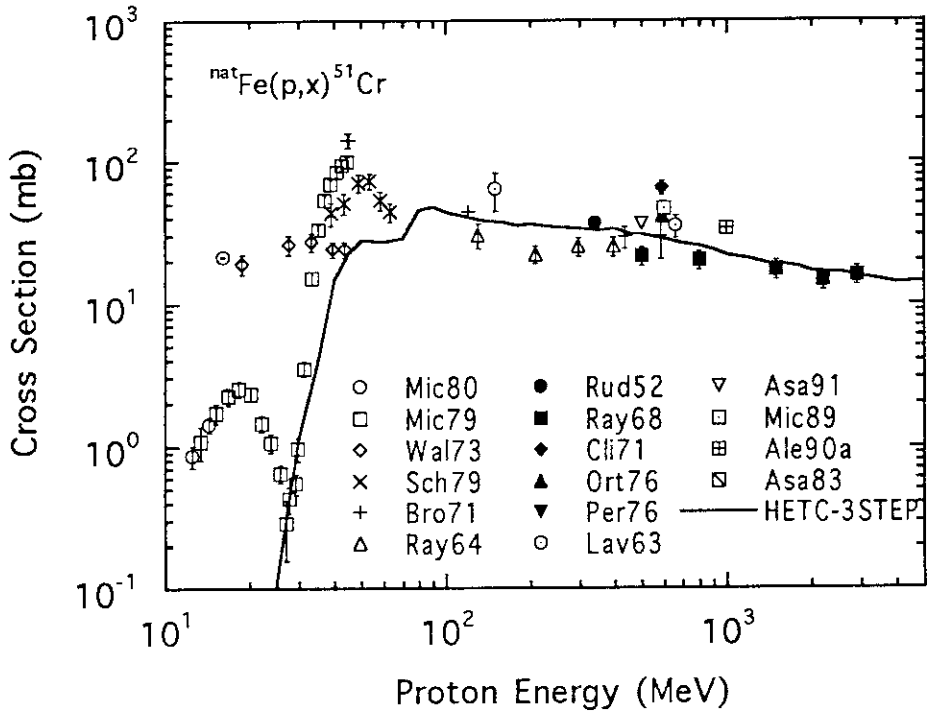

Fig. 40 Cross section of the ^{nat}Fe(p, x)^{51}Cr reaction. The notes to the marks and line are the same as for Fig. 23.

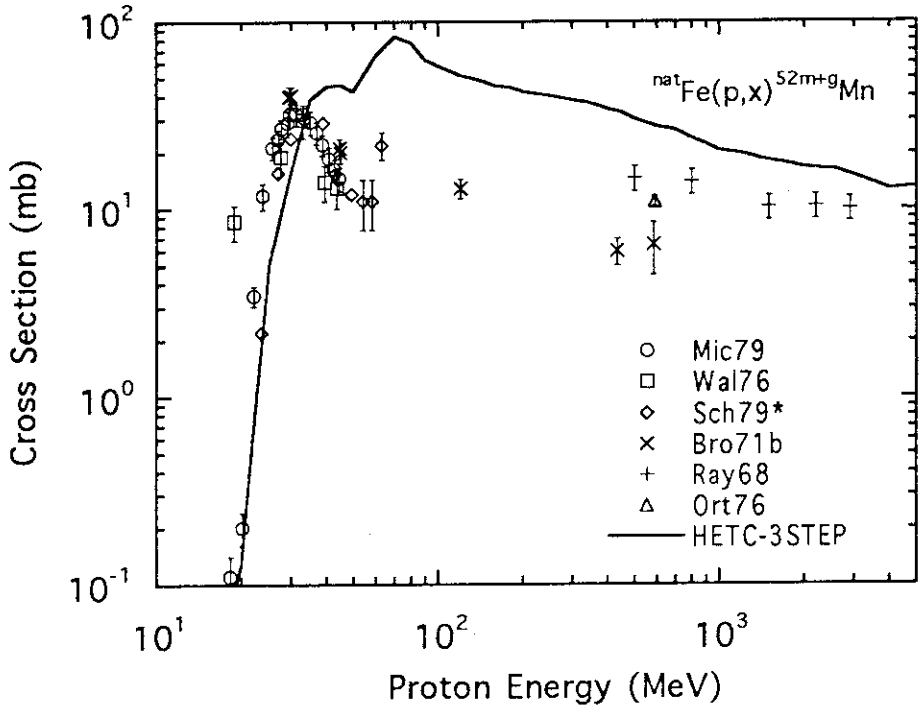

Fig. 41 Cross section of the $^{nat}Fe(p,x)^{52m+g}Mn$ reaction. The notes to the marks and line are the same as for Fig. 23.

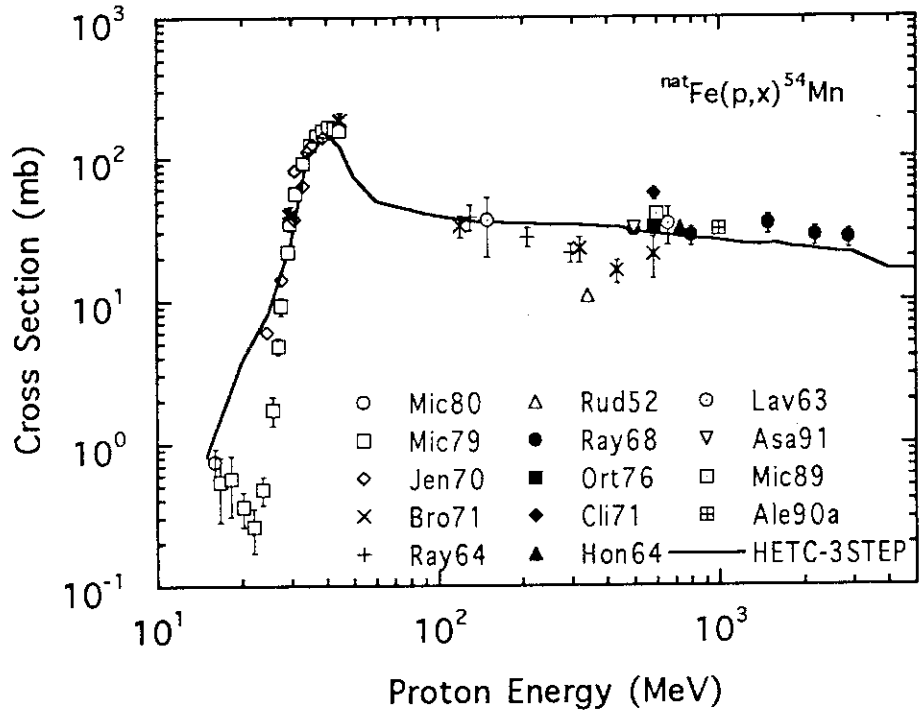

Fig. 42 Cross section of the $^{nat}Fe(p,x)^{54}Mn$ reaction. The notes to the marks and line are the same as for Fig. 23.

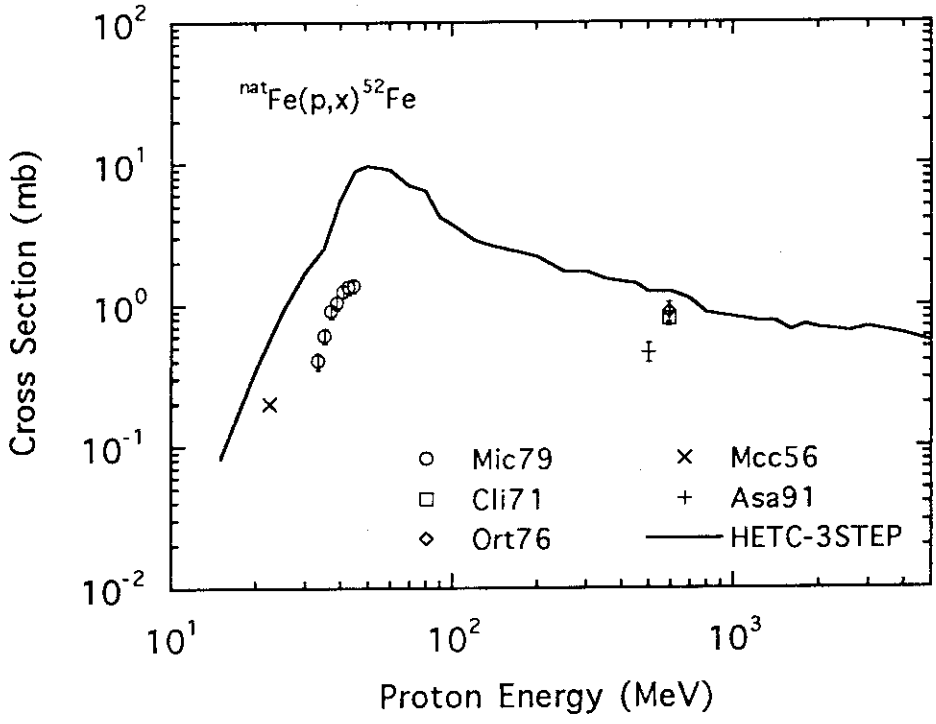

Fig. 43 Cross section of the $^{nat}Fe(p,x)^{52}Fe$ reaction. The notes to the marks and line are the same as for Fig. 23.

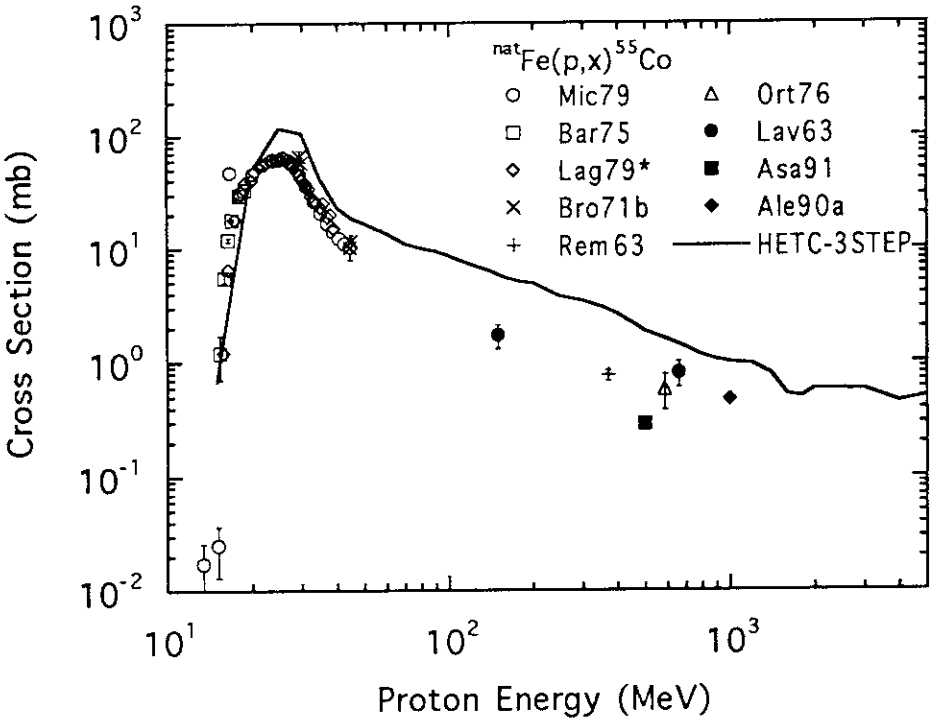

Fig. 44 Cross section of the $^{nat}Fe(p,x)^{55}Co$ reaction. The notes to the marks and line are the same as for Fig. 23.

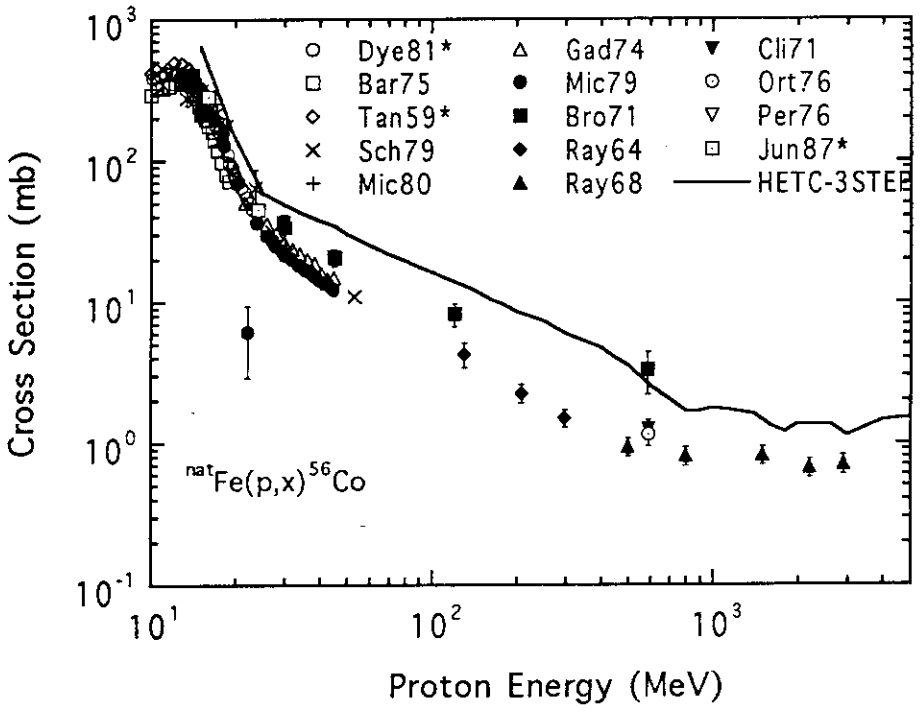

Fig. 45 Cross section of the $^{nat}Fe(p,x)^{56}Co$ reaction. The notes to the marks and line are the same as for Fig. 23.

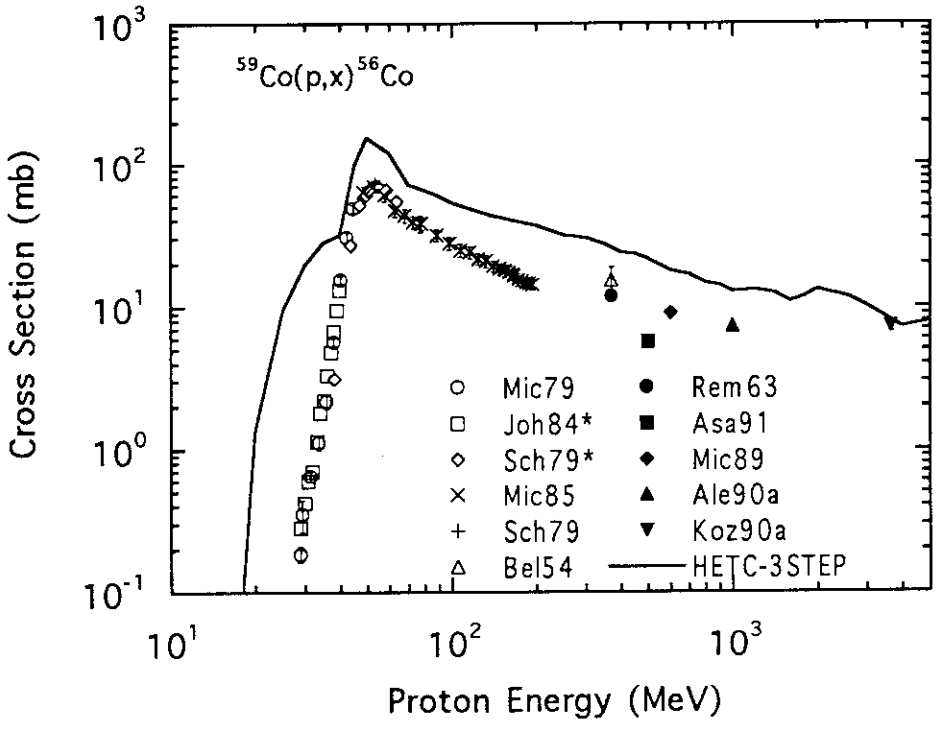

Fig. 46 Cross section of the $^{59}Co(p,x)^{56}Co$ reaction. The notes to the marks and line are the same as for Fig. 23.

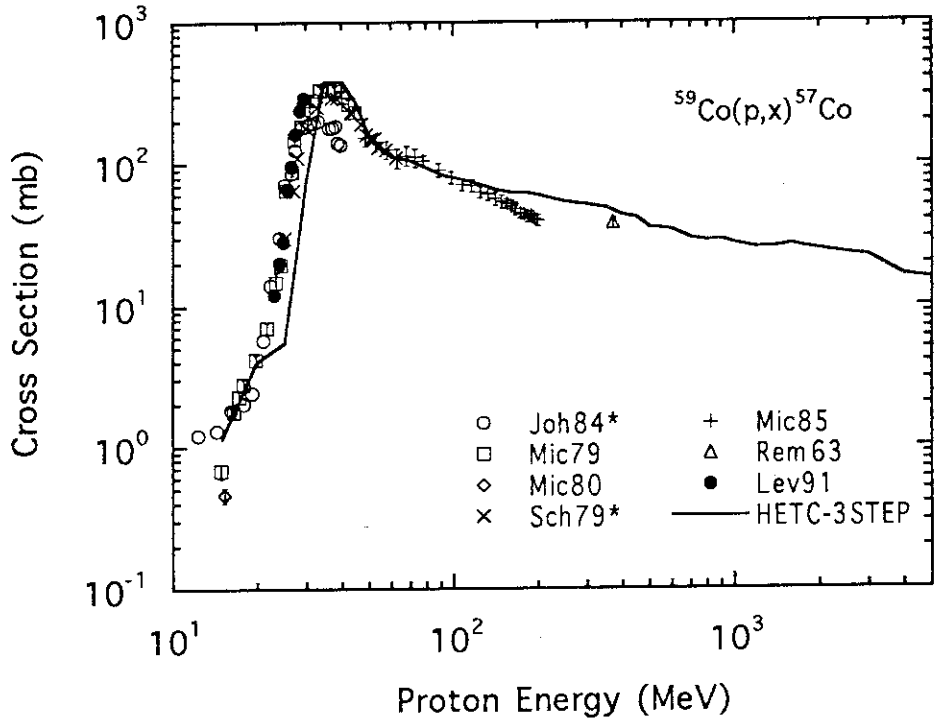

Fig. 47 Cross section of the ^{59}Co(p, x)^{57}Co reaction. The notes to the marks and line are the same as for Fig. 23.

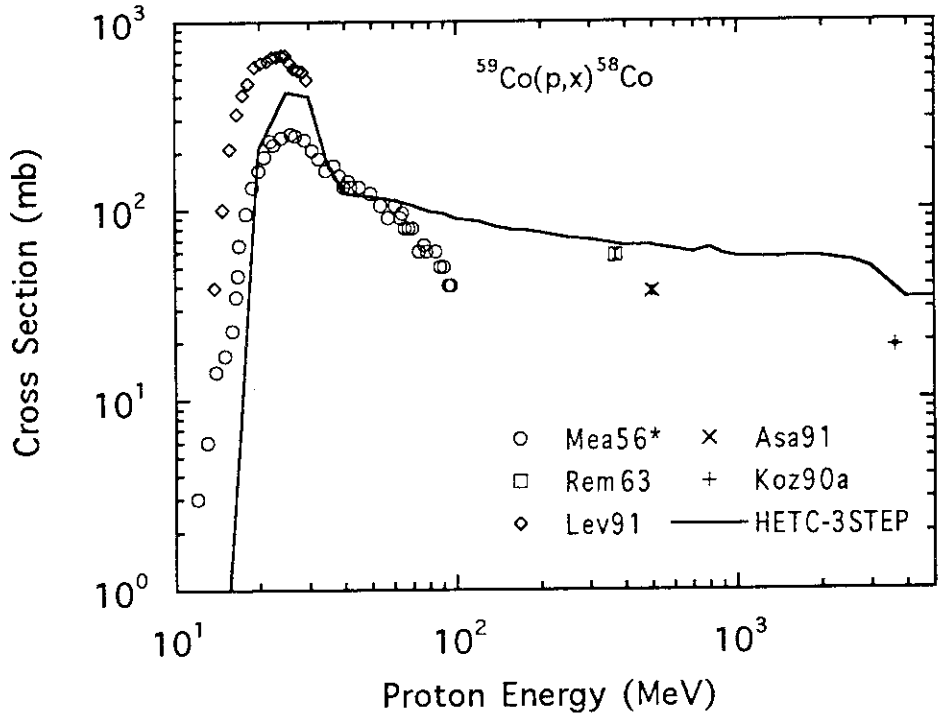

Fig. 48 Cross section of the ^{59}Co(p, x)^{58}Co reaction. The notes to the marks and line are the same as for Fig. 23.

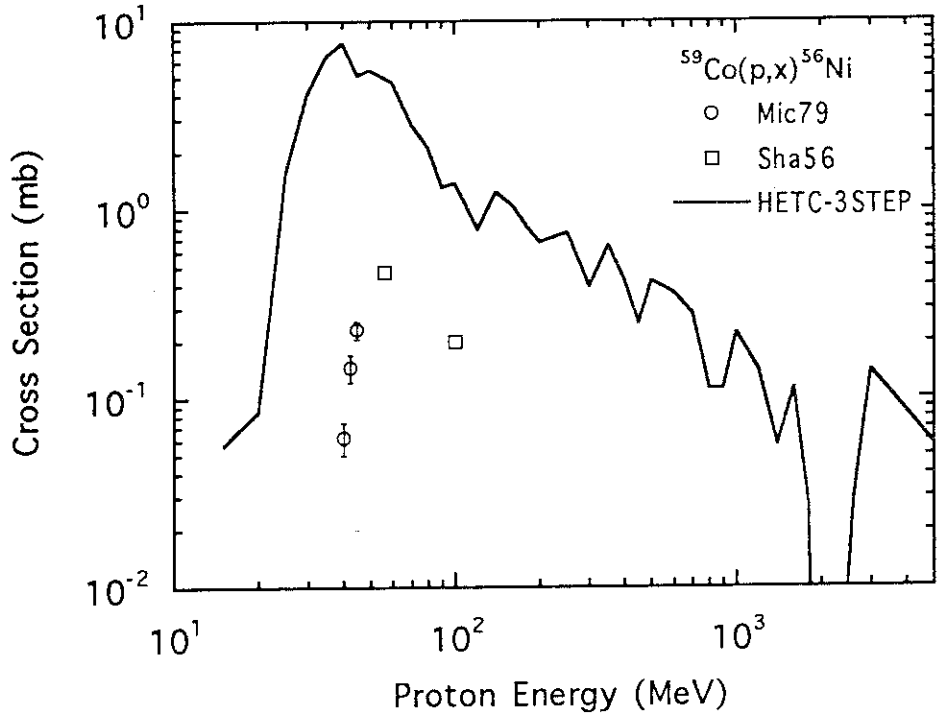

Fig. 49 Cross section of the ^{59}Co(p, x)^{56}Ni reaction. The notes to the marks and line are the same as for Fig. 23.

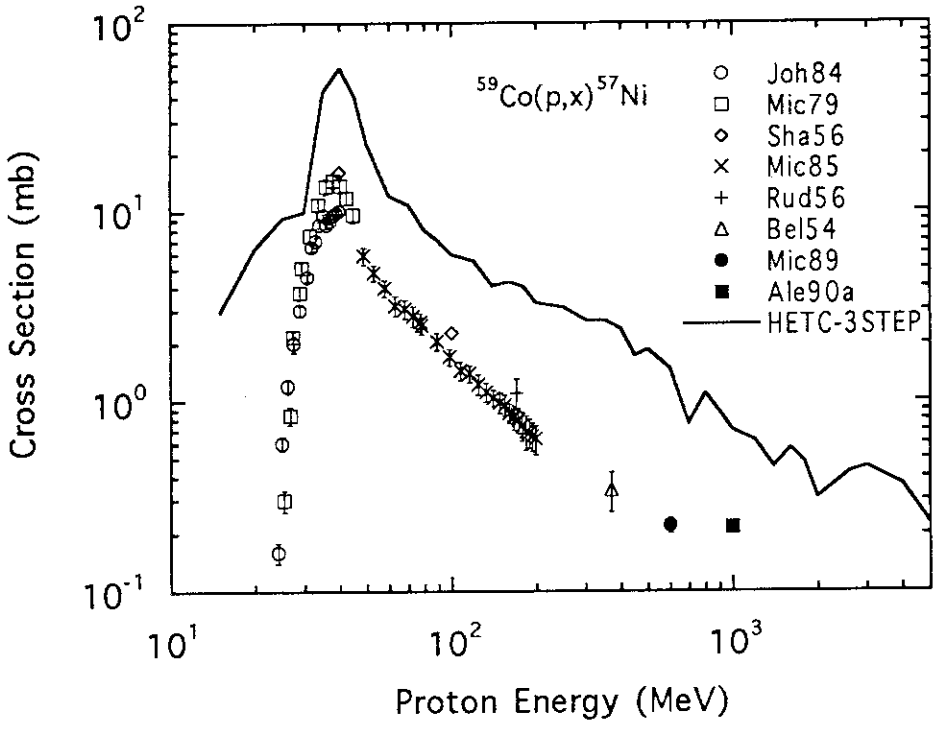

Fig. 50 Cross section of the ^{59}Co(p, x)^{57}Ni reaction. The notes to the marks and line are the same as for Fig. 23.

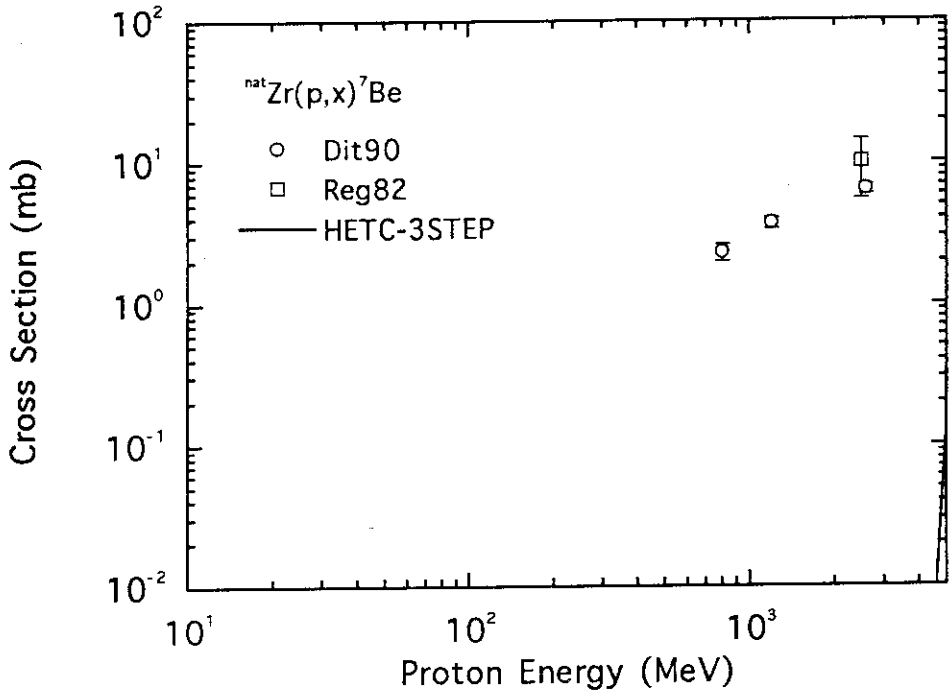

Fig. 51 Cross section of the ^{nat}Zr(p, x)^{7}Be reaction. The notes to the marks and line are the same as for Fig. 23.

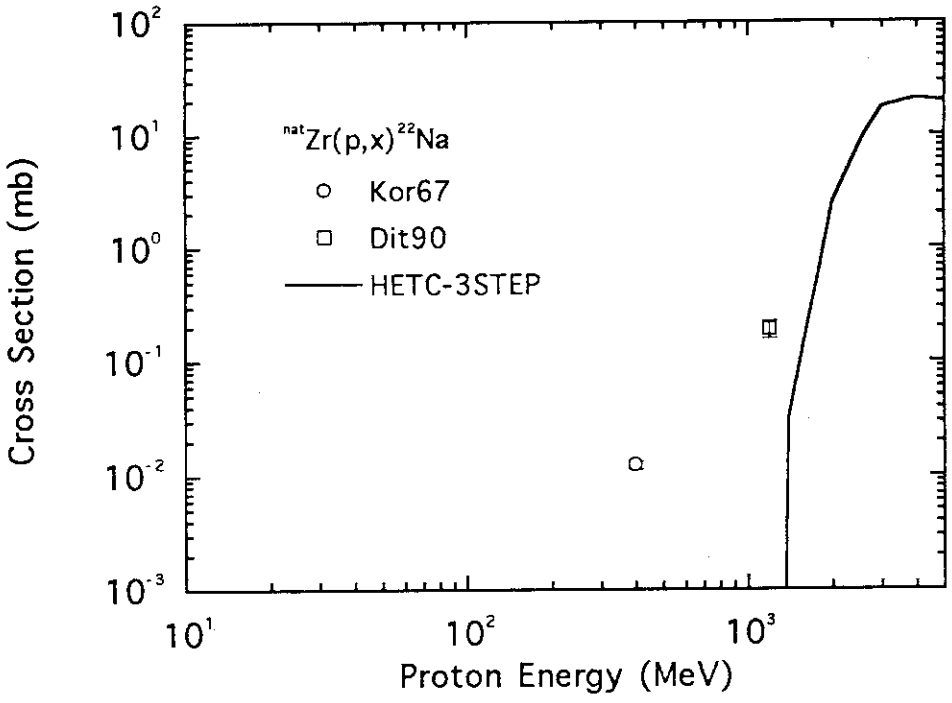

Fig. 52 Cross section of the ^{nat}Zr(p, x)^{22}Na reaction. The notes to the marks and line are the same as for Fig. 23.

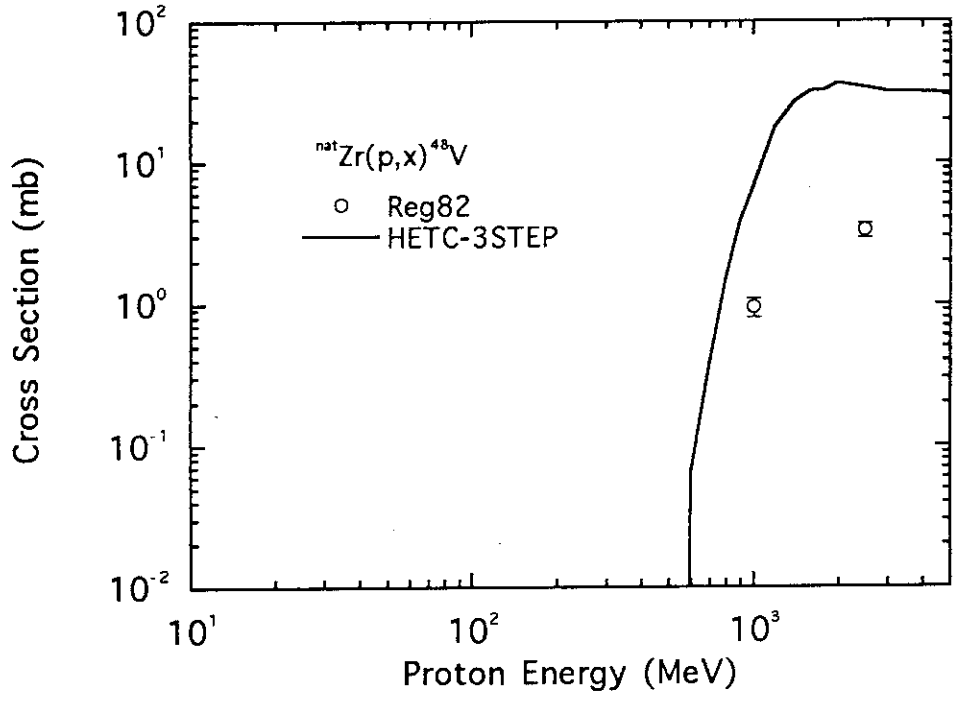

Fig. 53 Cross section of the $^{nat}Zr(p,x)^{48}V$ reaction. The notes to the marks and line are the same as for Fig. 23.

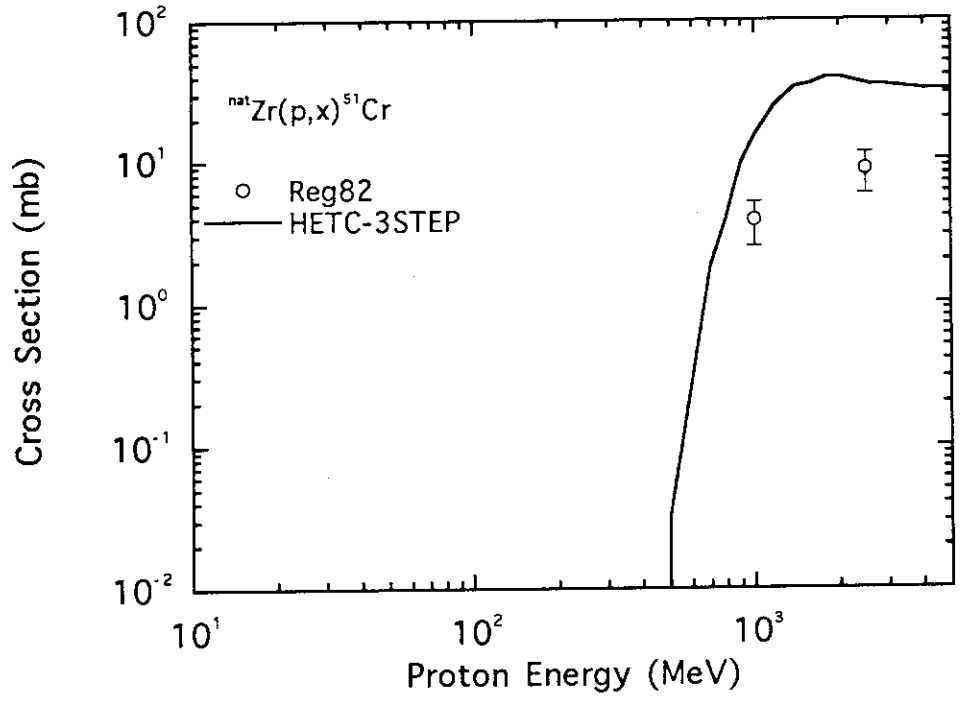

Fig. 54 Cross section of the $^{nat}Zr(p,x)^{51}Cr$ reaction. The notes to the marks and line are the same as for Fig. 23.

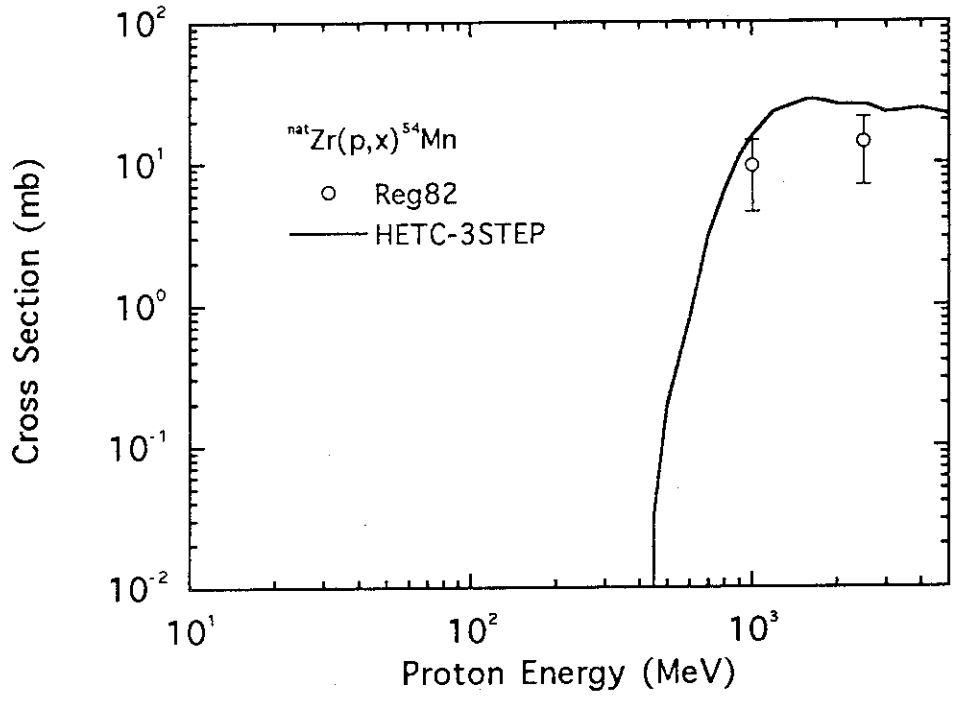

Fig. 55 Cross section of the ^{nat}Zr(p, x)^{54}Mn reaction. The notes to the marks and line are the same as for Fig. 23.

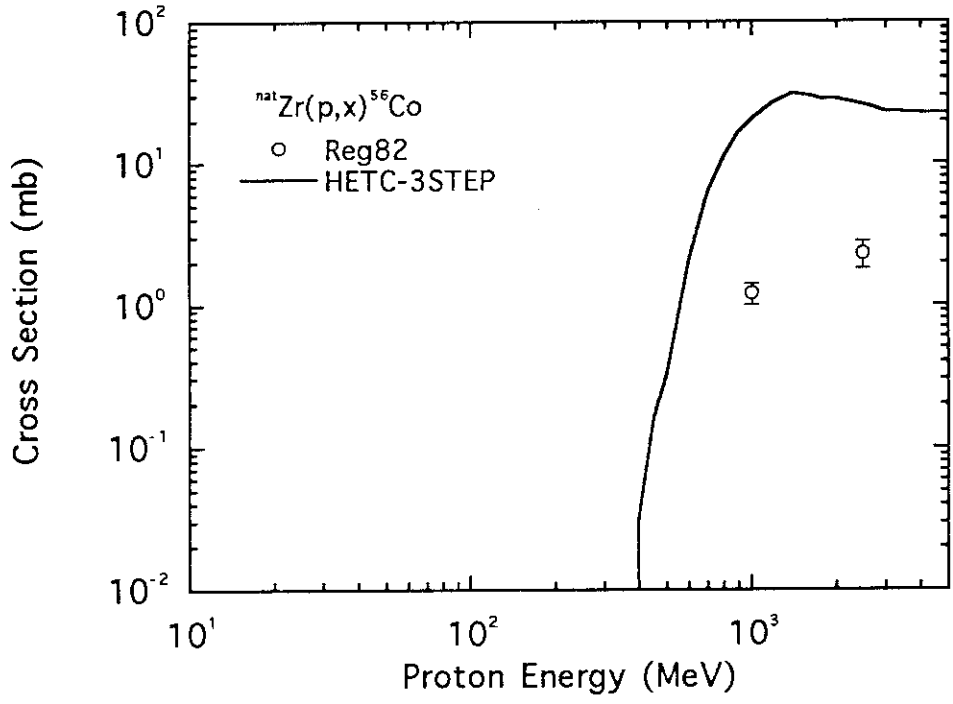

Fig. 56 Cross section of the ^{nat}Zr(p, x)^{56}Co reaction. The notes to the marks and line are the same as for Fig. 23.

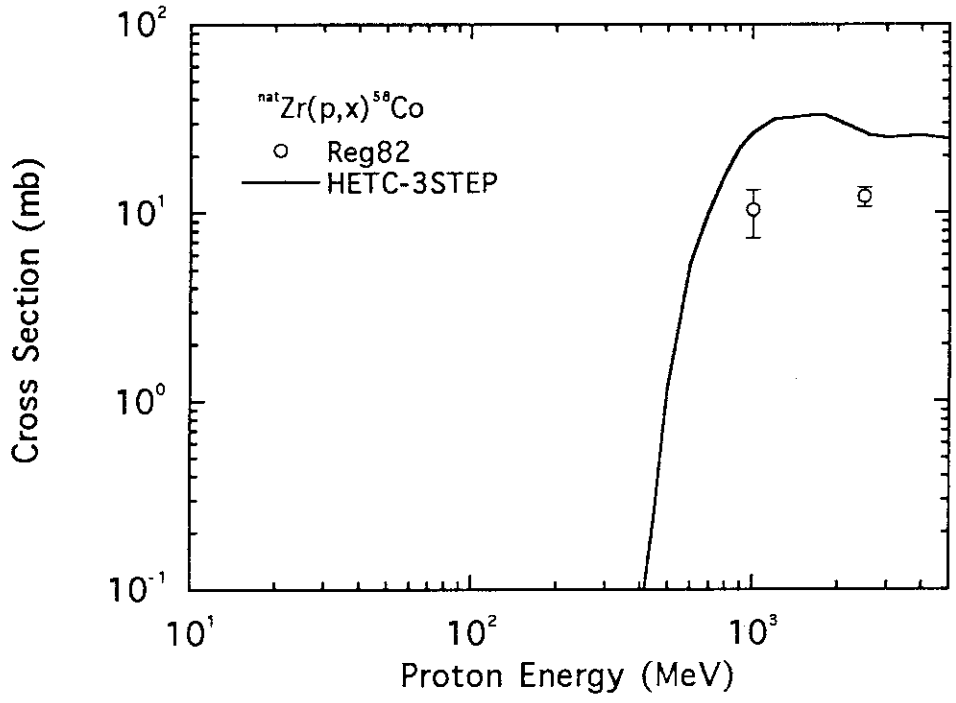

Fig. 57 Cross section of the ^{nat}Zr(p, x)^{58}Co reaction. The notes to the marks and line are the same as for Fig. 23.

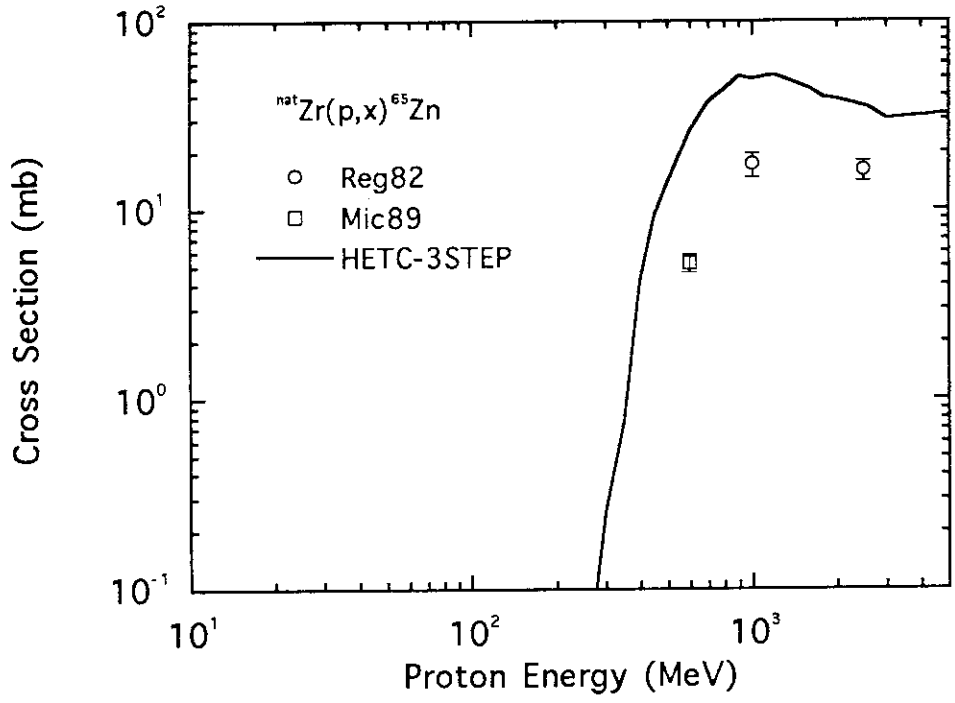

Fig. 58 Cross section of the ^{nat}Zr(p, x)^{65}Zn reaction. The notes to the marks and line are the same as for Fig. 23.

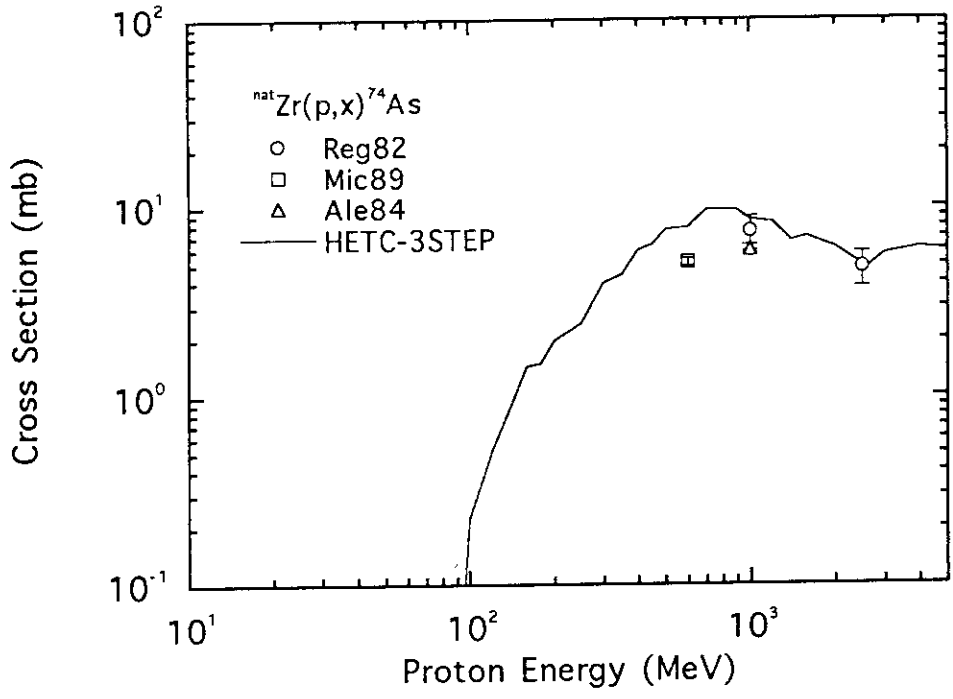

Fig. 59 Cross section of the $^{nat}Zr(p,x)^{74}As$ reaction. The notes to the marks and line are the same as for Fig. 23.

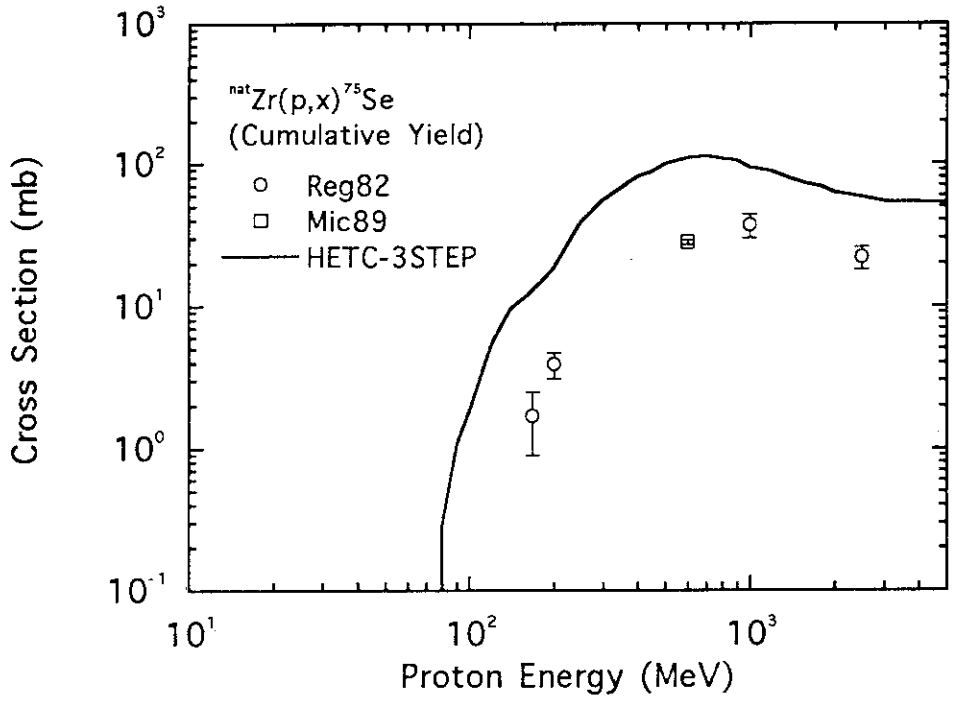

Fig. 60 Cumulative cross section of the $^{nat}Zr(p,x)^{75}Se$ reaction. The notes to the marks and line are the same as for Fig. 23.

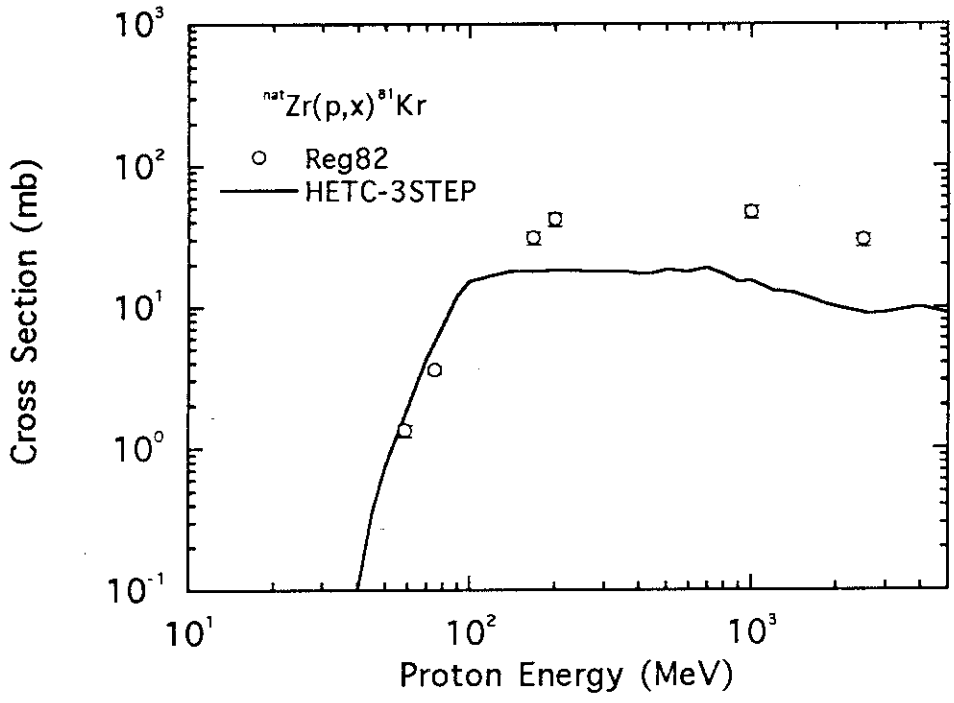

Fig. 61 Cross section of the $^{nat}Zr(p,x)^{81}Kr$ reaction. The notes to the marks and line are the same as for Fig. 23.

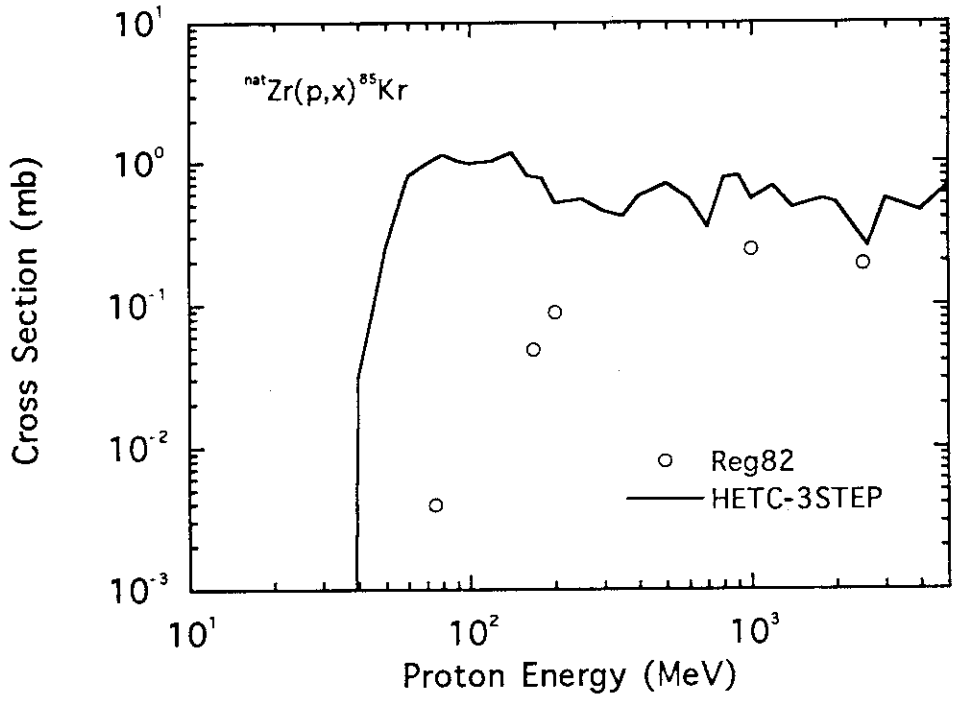

Fig. 62 Cross section of the $^{nat}Zr(p,x)^{85}Kr$ reaction. The notes to the marks and line are the same as for Fig. 23.

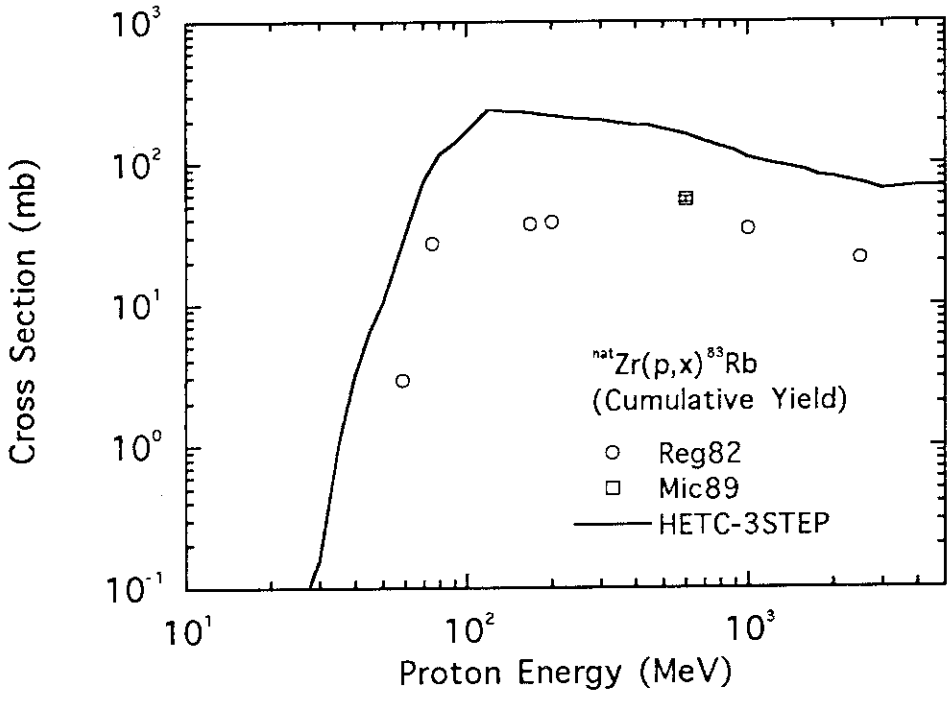

Fig. 63 Cumulative cross section of the ^{nat}Zr(p, x)^{83}Rb reaction. The notes to the marks and line are the same as for Fig. 23.

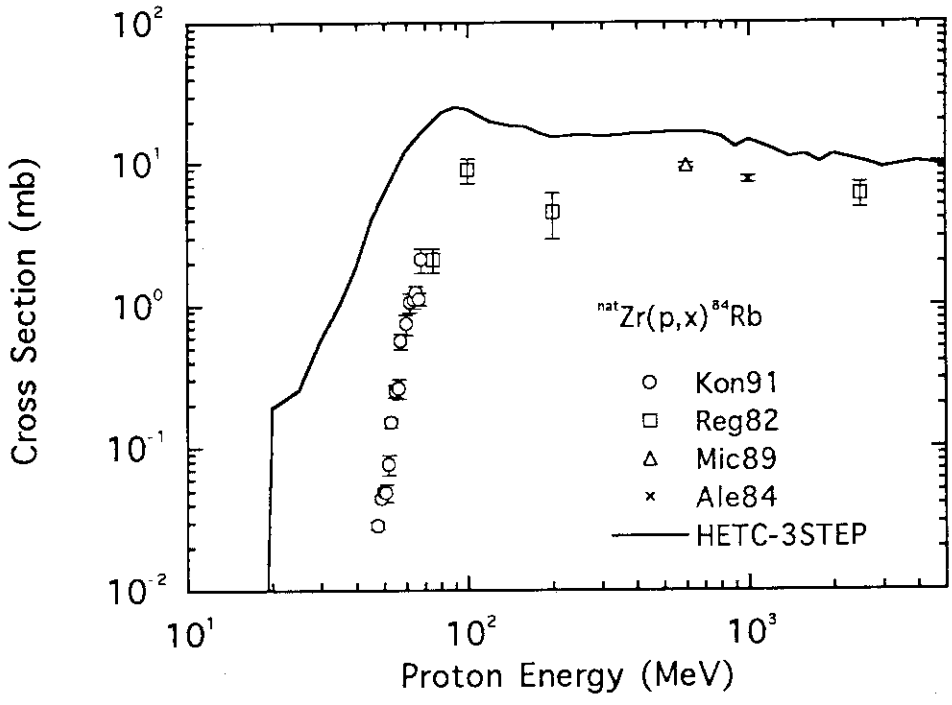

Fig. 64 Cross section of the ^{nat}Zr(p, x)^{84}Rb reaction. The notes to the marks and line are the same as for Fig. 23.

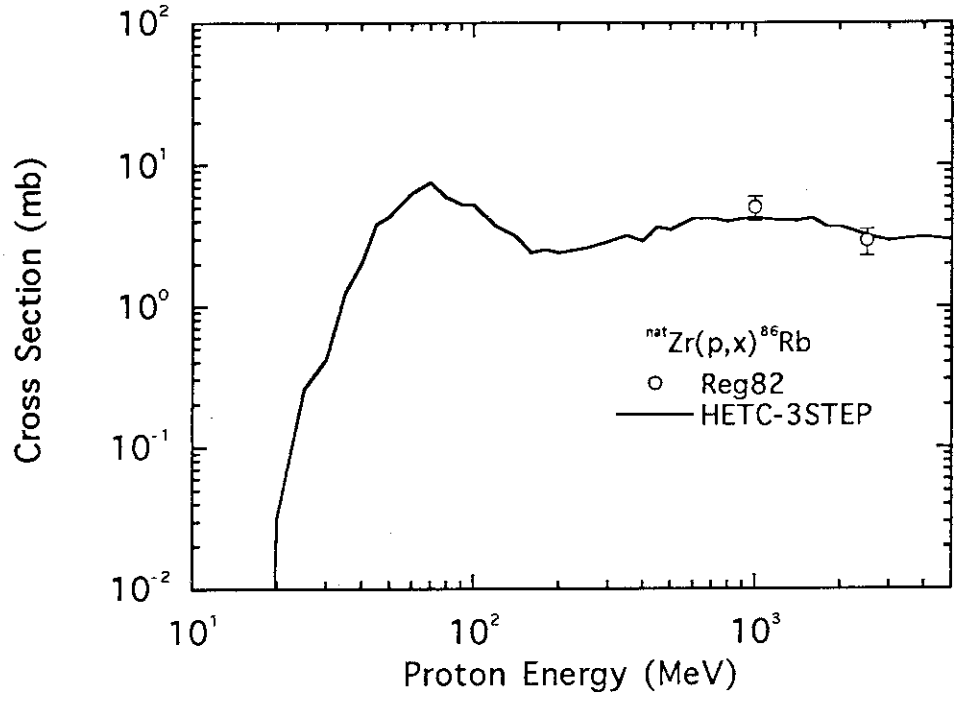

Fig. 65 Cross section of the ^{nat}Zr(p, x)^{86}Rb reaction. The notes to the marks and line are the same as for Fig. 23.

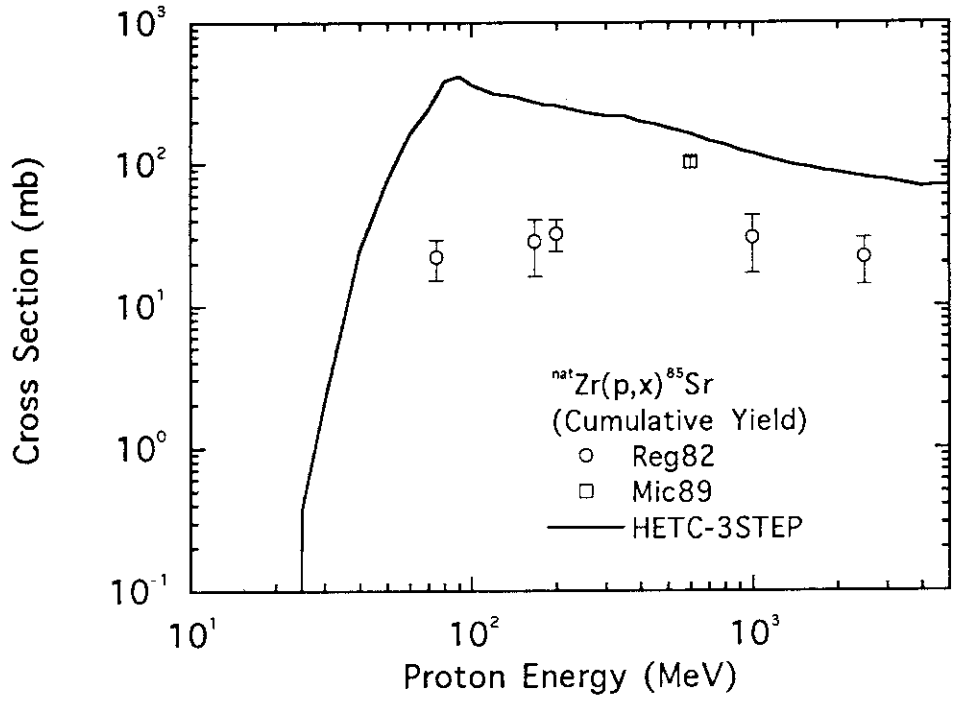

Fig. 66 Cumulative cross section of the ^{nat}Zr(p, x)^{85}Sr reaction. The notes to the marks and line are the same as for Fig. 23.

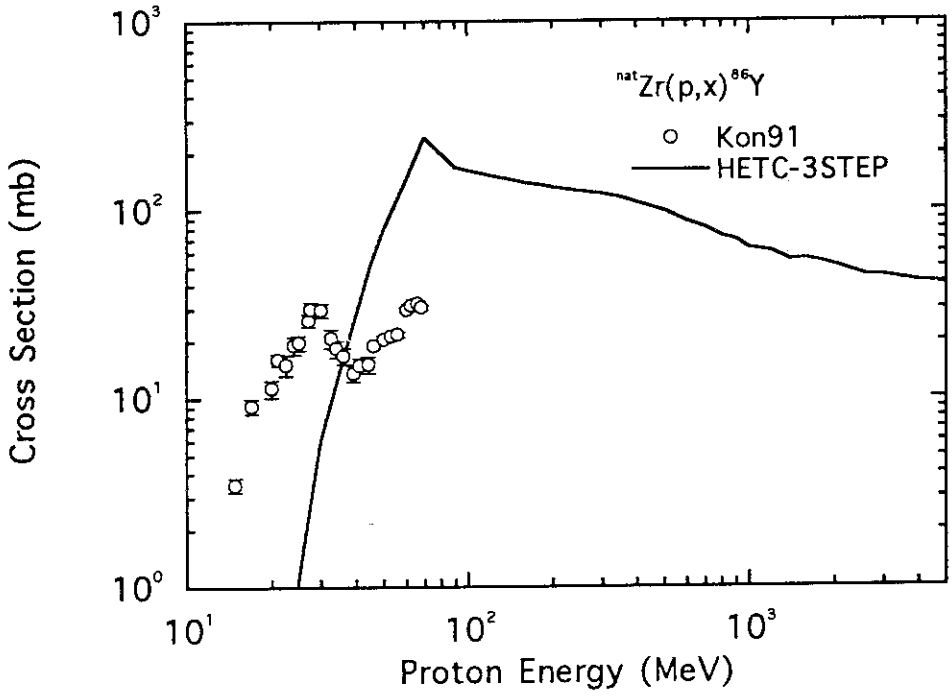

Fig. 67 Cross section of the $^{nat}Zr(p,x)^{86}Y$ reaction. The notes to the marks and line are the same as for Fig. 23.

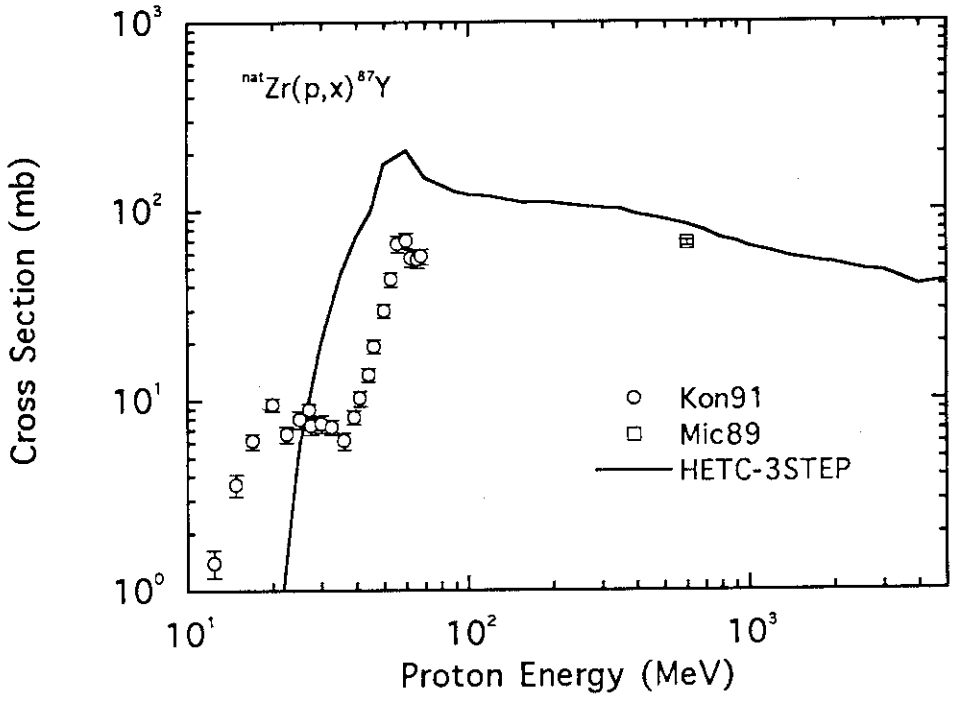

Fig. 68 Cross section of the $^{nat}Zr(p,x)^{87}Y$ reaction. The notes to the marks and line are the same as for Fig. 23.

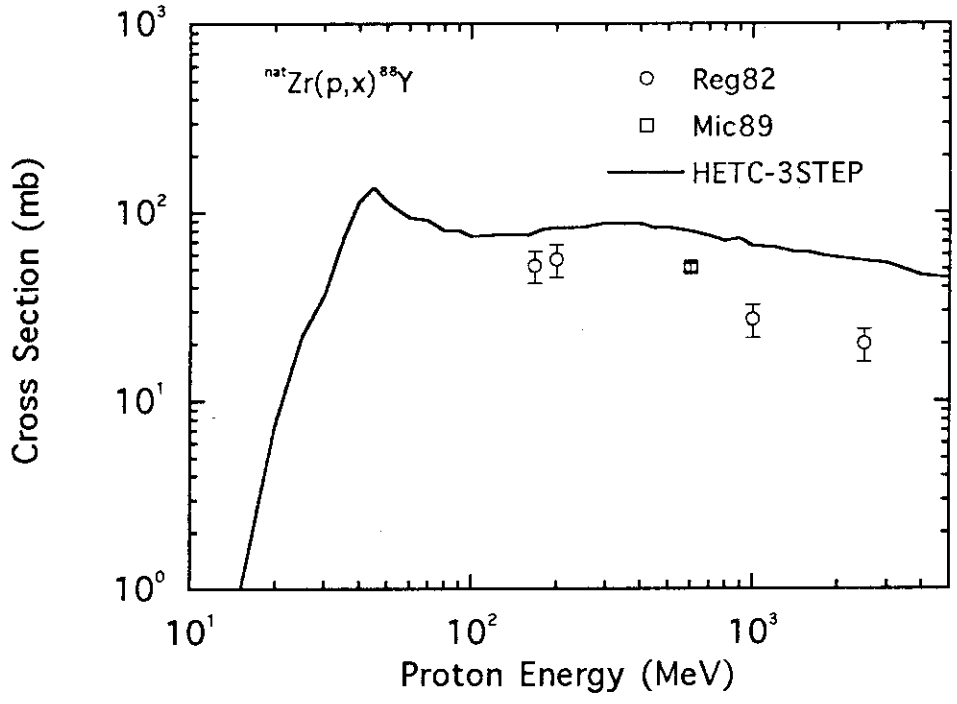

Fig. 69 Cross section of the ^{nat}Zr(p, x)^{88}Y reaction. The notes to the marks and line are the same as for Fig. 23.

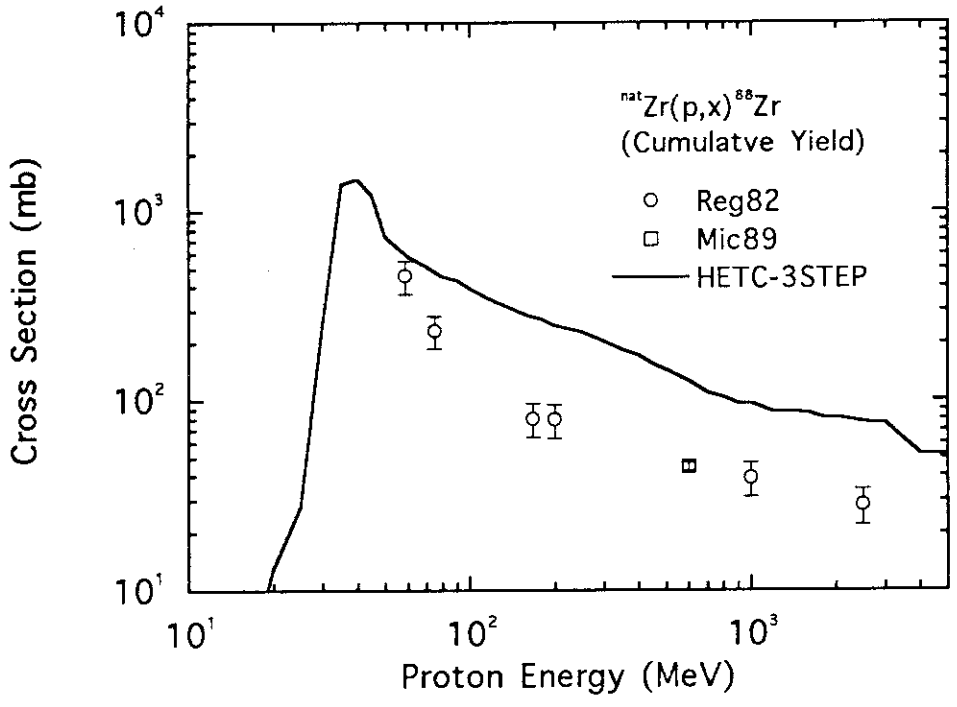

Fig. 70 Cumulative cross section of the ^{nat}Zr(p, x)^{88}Zr reaction. The notes to the marks and line are the same as for Fig. 23.

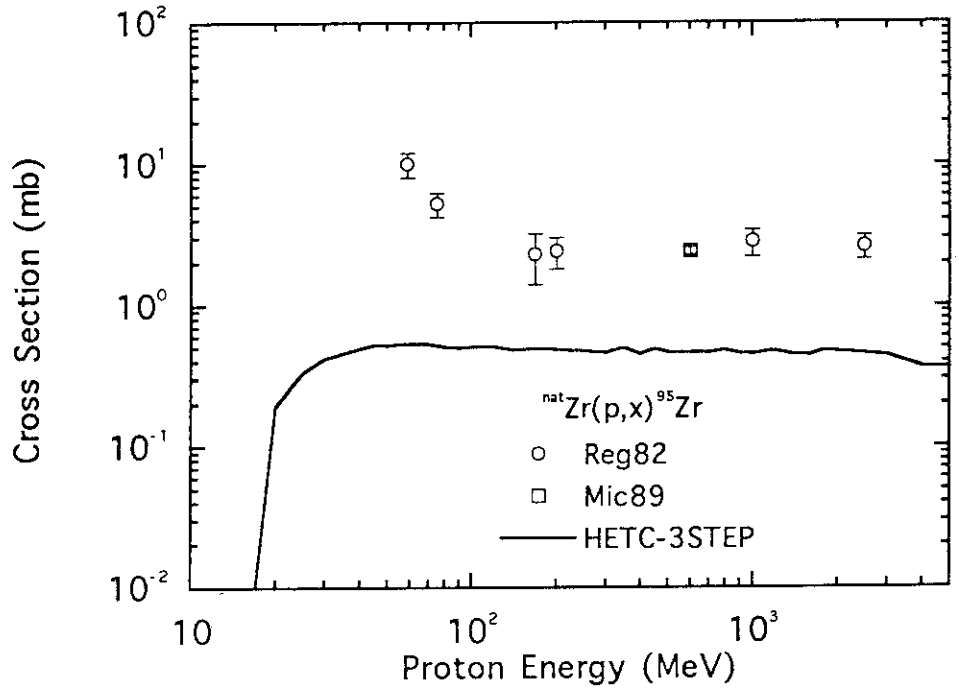

Fig. 71 Cross section of the ^{nat}Zr(p, x)^{95}Zr reaction. The notes to the marks and line are the same as for Fig. 23.

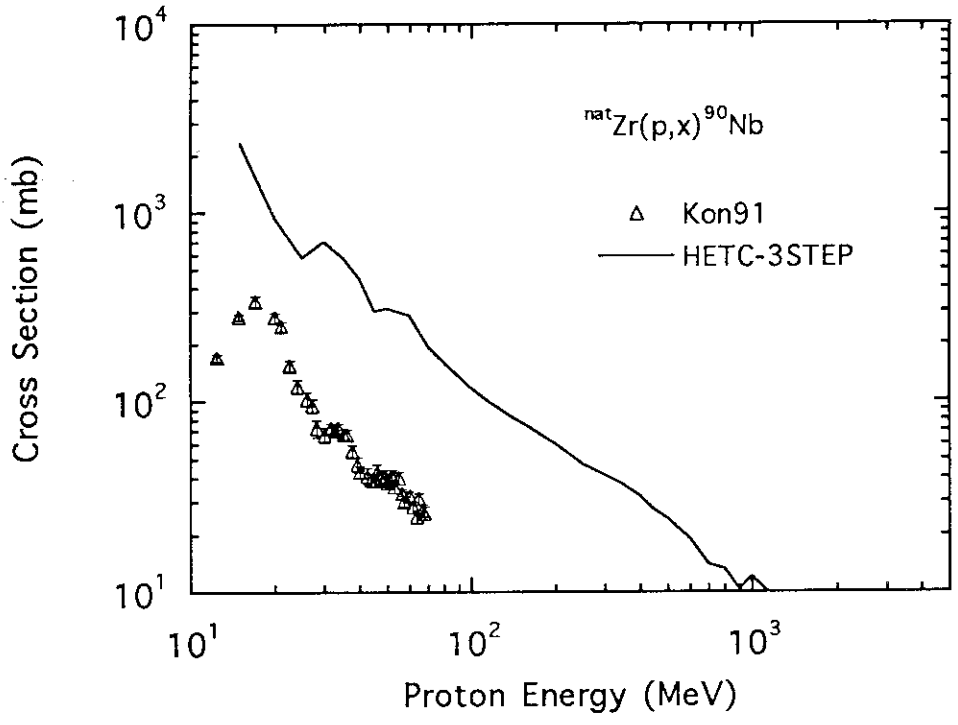

Fig. 72 Cross section of the ^{nat}Zr(p, x)^{90}Nb reaction. The notes to the marks and line are the same as for Fig. 23.

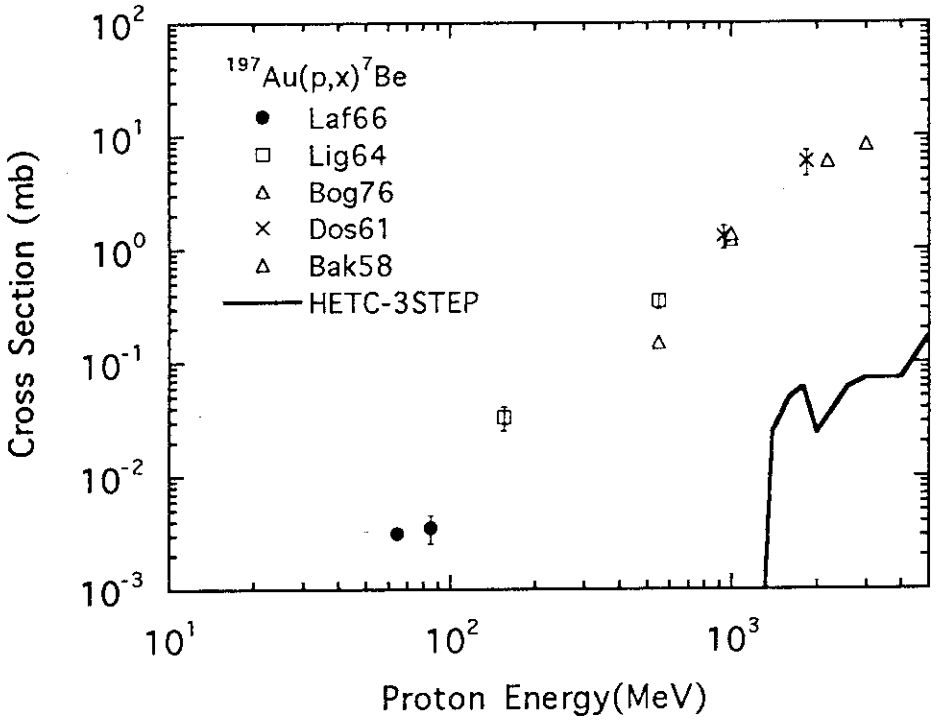

Fig. 73 Cross section of the ^{197}Au(p, x)^{7}Be reaction. The notes to the marks and line are the same as for Fig. 23.

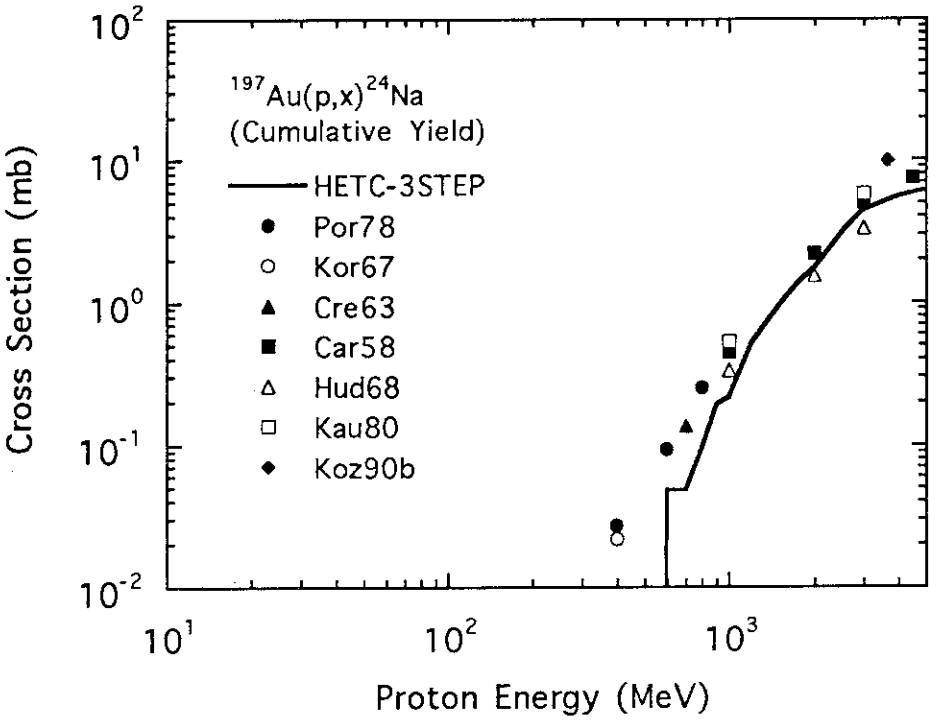

Fig. 74 Cross section of the ^{197}Au(p, x)^{24}Na reaction. The notes to the marks and line are the same as for Fig. 23.

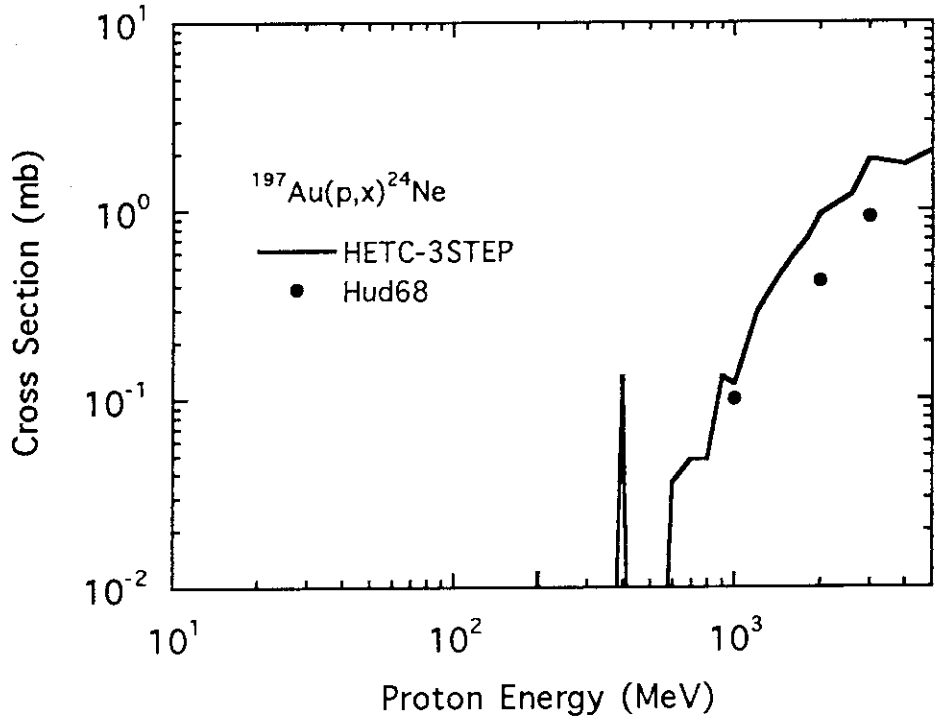

Fig. 75 Cumulative cross section of the ^{197}Au(p, x)^{24}Ne reaction. The notes to the marks and line are the same as for Fig. 23.

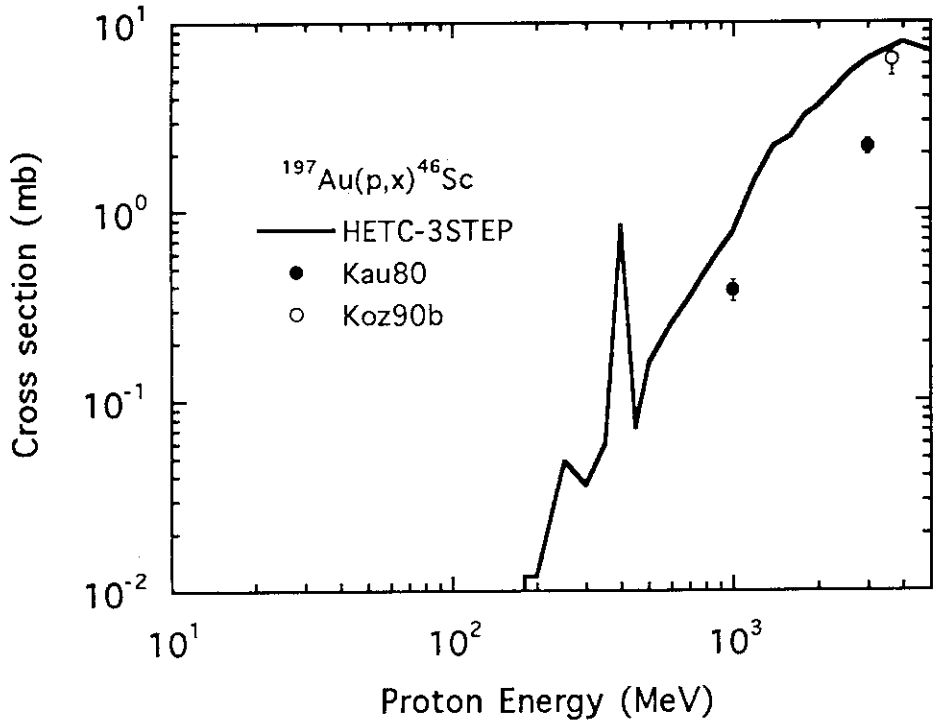

Fig. 76 Cross section of the ^{197}Au(p, x)^{46}Sc reaction. The notes to the marks and line are the same as for Fig. 23.

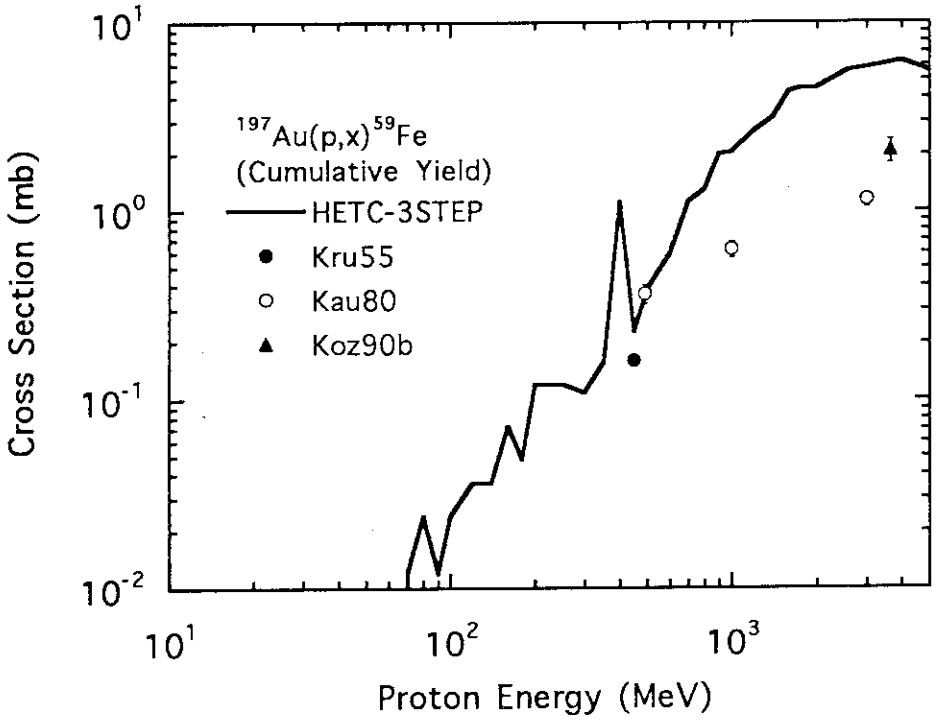

Fig. 77 Cross section of the ^{197}Au(p, x)^{59}Fe reaction. The notes to the marks and line are the same as for Fig. 23.

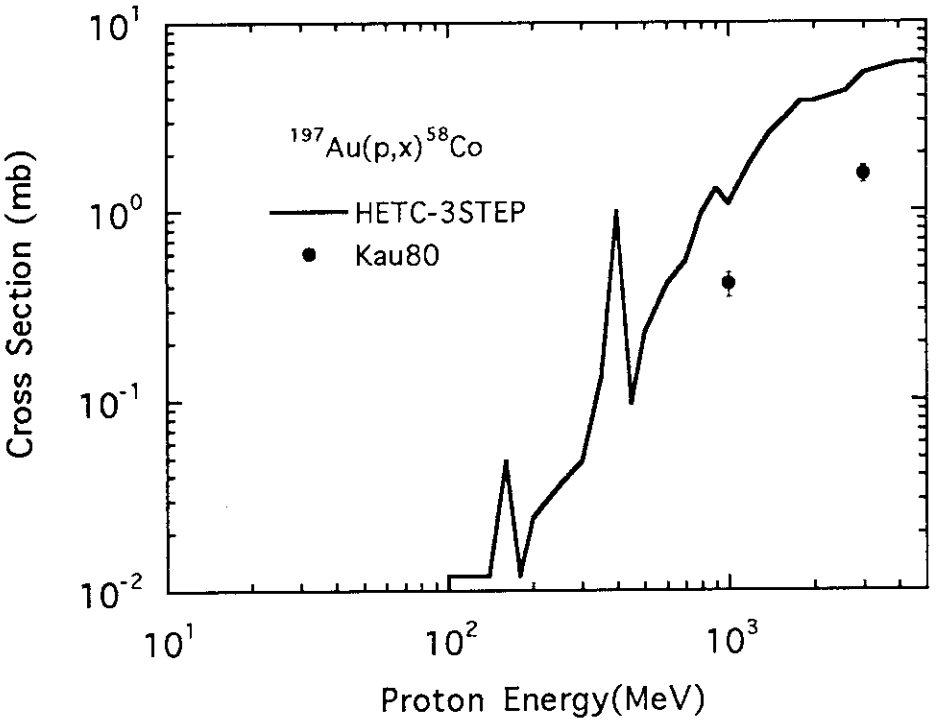

Fig. 78 Cross section of the ^{197}Au(p, x)^{58}Co reaction. The notes to the marks and line are the same as for Fig. 23.

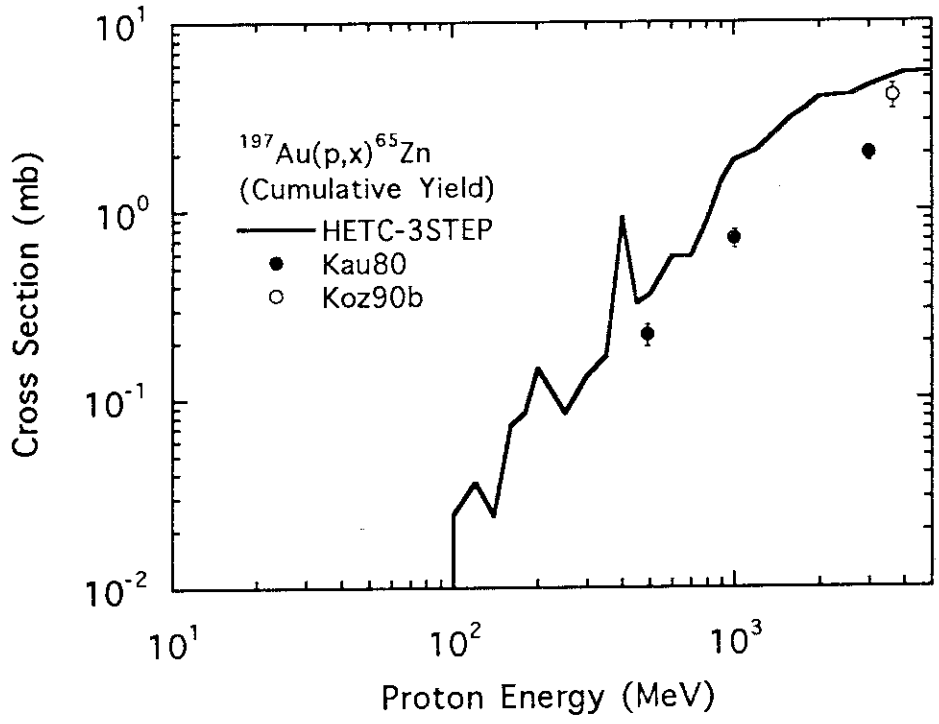

Fig. 79 Cumulative cross section of the ^{197}Au(p, x)^{65}Zn reaction. The notes to the marks and line are the same as for Fig. 23.

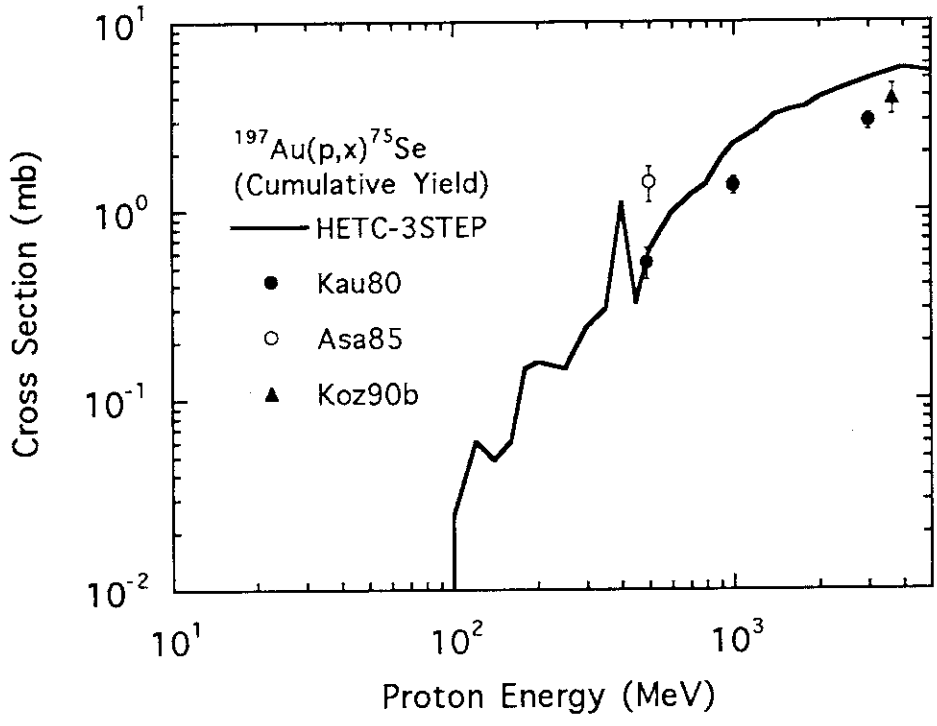

Fig. 80 Cumulative cross section of the ^{197}Au(p, x)^{75}Se reaction. The notes to the marks and line are the same as for Fig. 23.

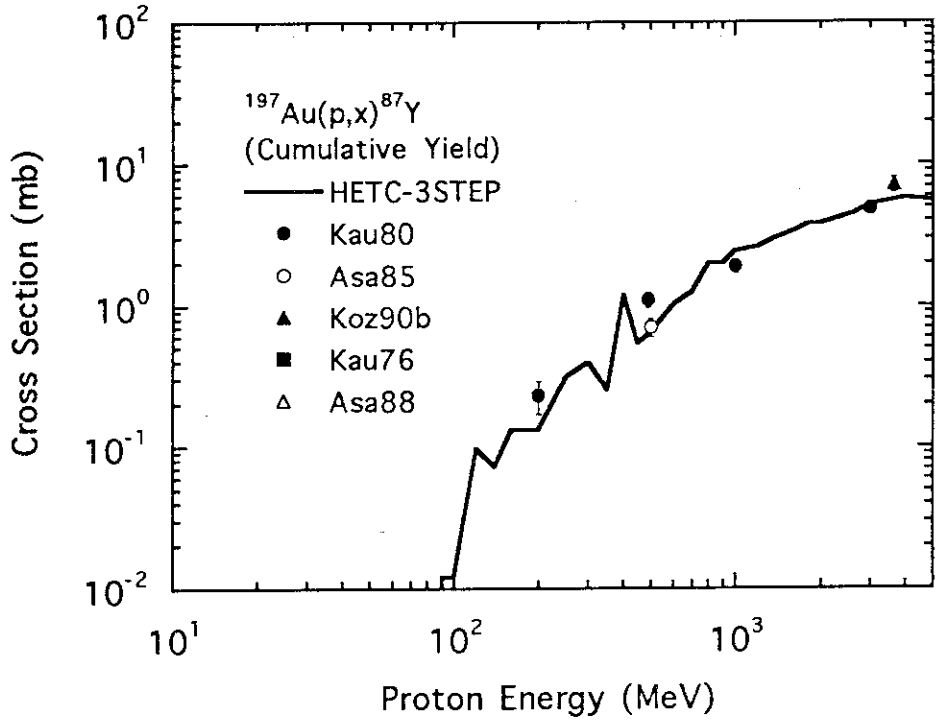

Fig. 81 Cumulative cross section of the ^{197}Au(p, x)^{87}Y reaction. The notes to the marks and line are the same as for Fig. 23.

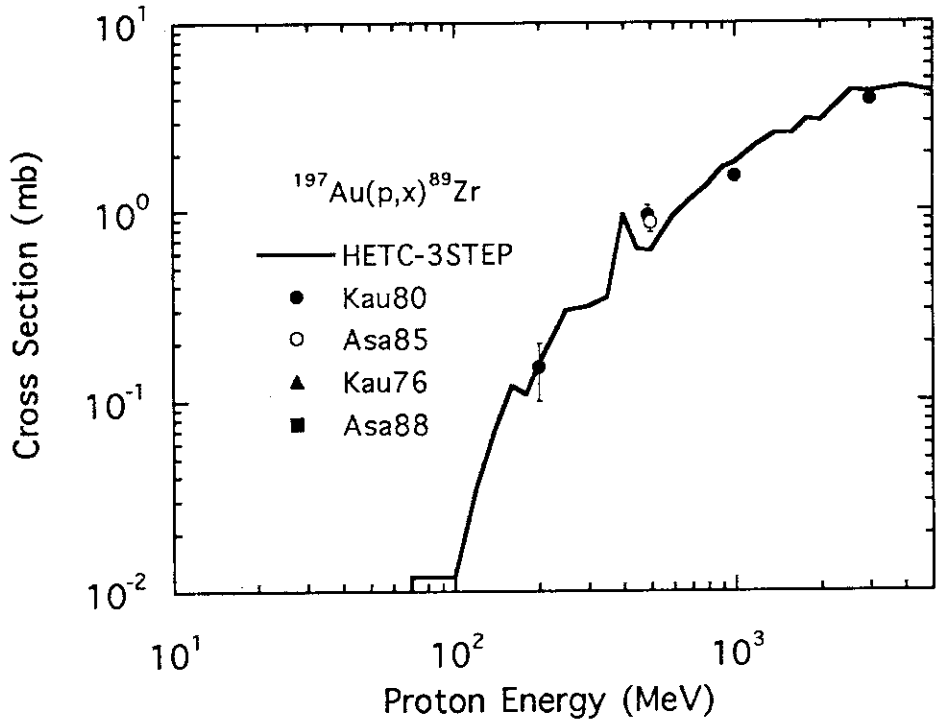

Fig. 82 Cumulative cross section of the ^{197}Au(p, x)^{89}Zr reaction. The notes to the marks and line are the same as for Fig. 23.

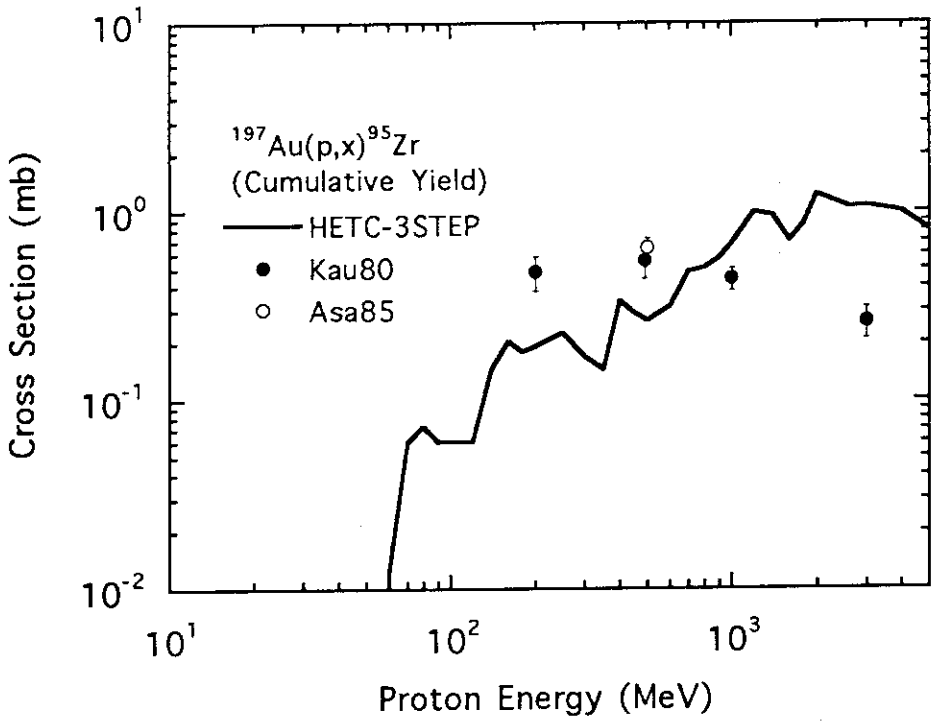

Fig. 83 Cumulative cross section of the ^{197}Au(p, x)^{95}Zr reaction. The notes to the marks and line are the same as for Fig. 23.

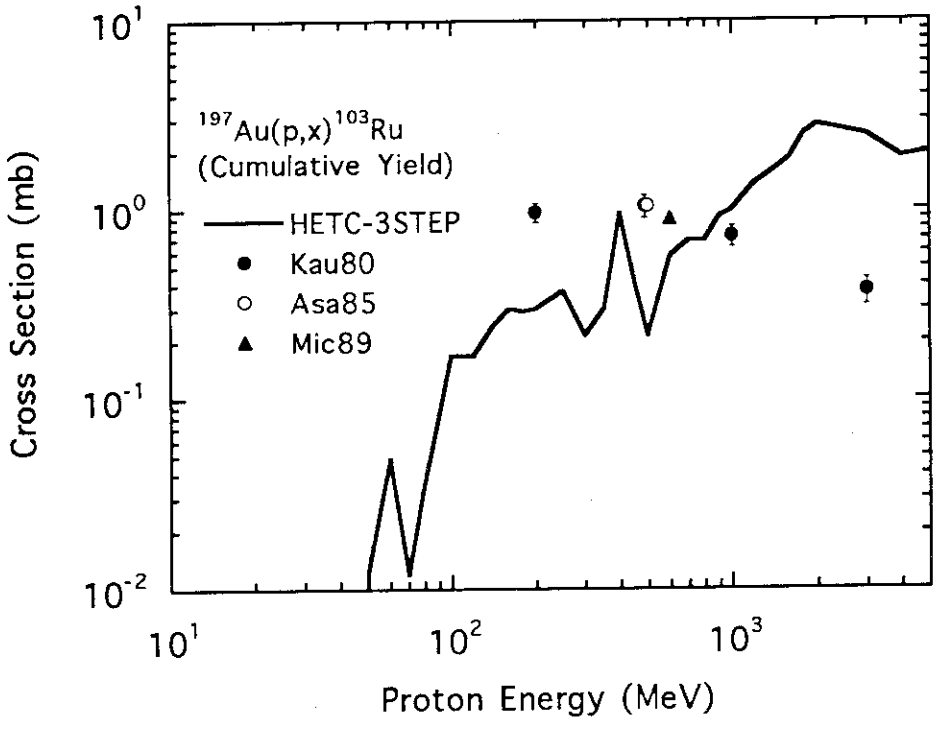

Fig. 84 Cumulative cross section of the ^{197}Au(p, x)^{103}Ru reaction. The notes to the marks and line are the same as for Fig. 23.

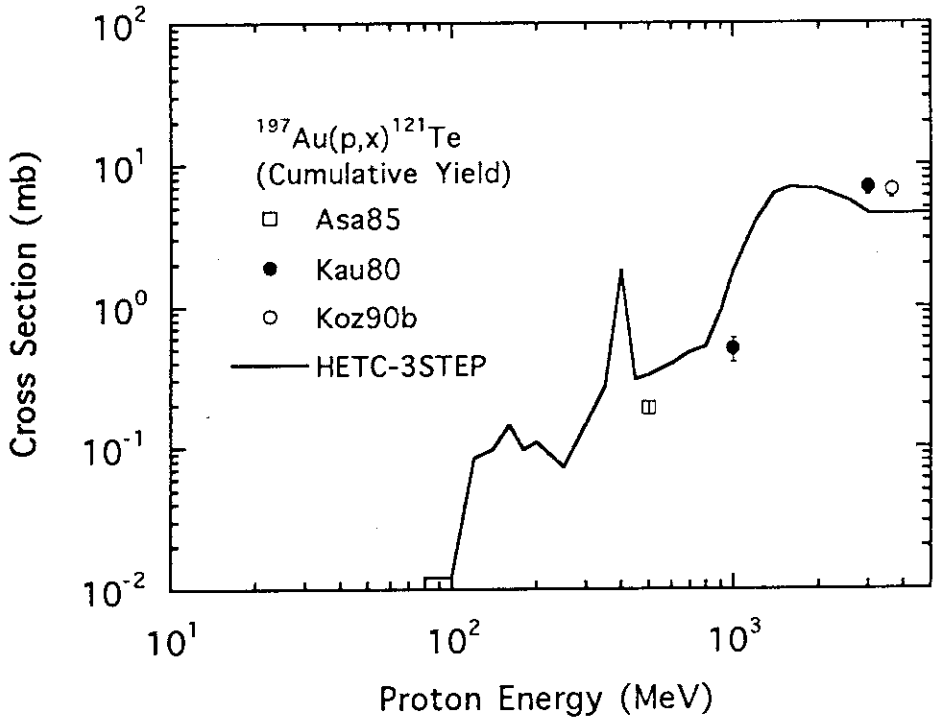

Fig. 85 Cumulative cross section of the ^{197}Au(p, x)^{121}Te reaction. The notes to the marks and line are the same as for Fig. 23.

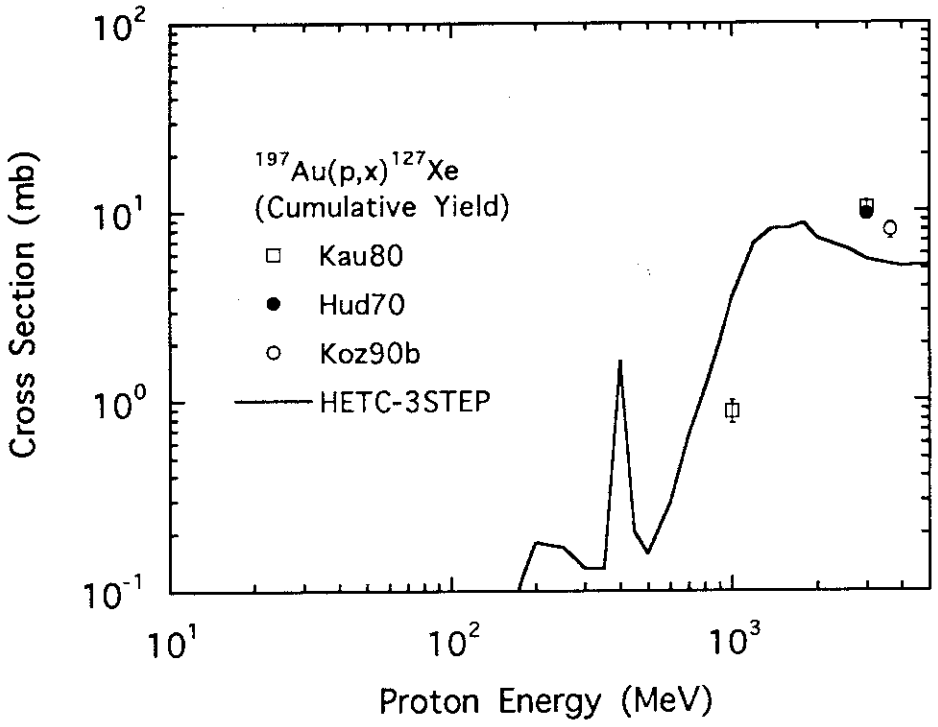

Fig. 86 Cumulative cross section of the ^{197}Au(p, x)^{127}Xe reaction. The notes to the marks and line are the same as for Fig. 23.

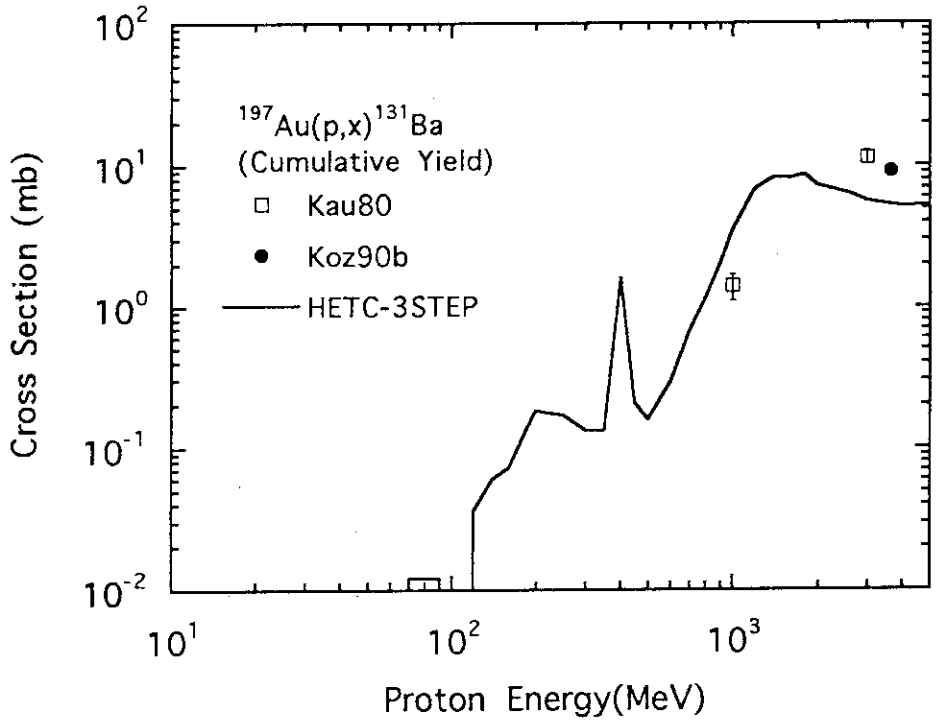

Fig. 87 Cumulative cross section of the ^{197}Au(p, x)^{131}Ba reaction. The notes to the marks and line are the same as for Fig. 23.

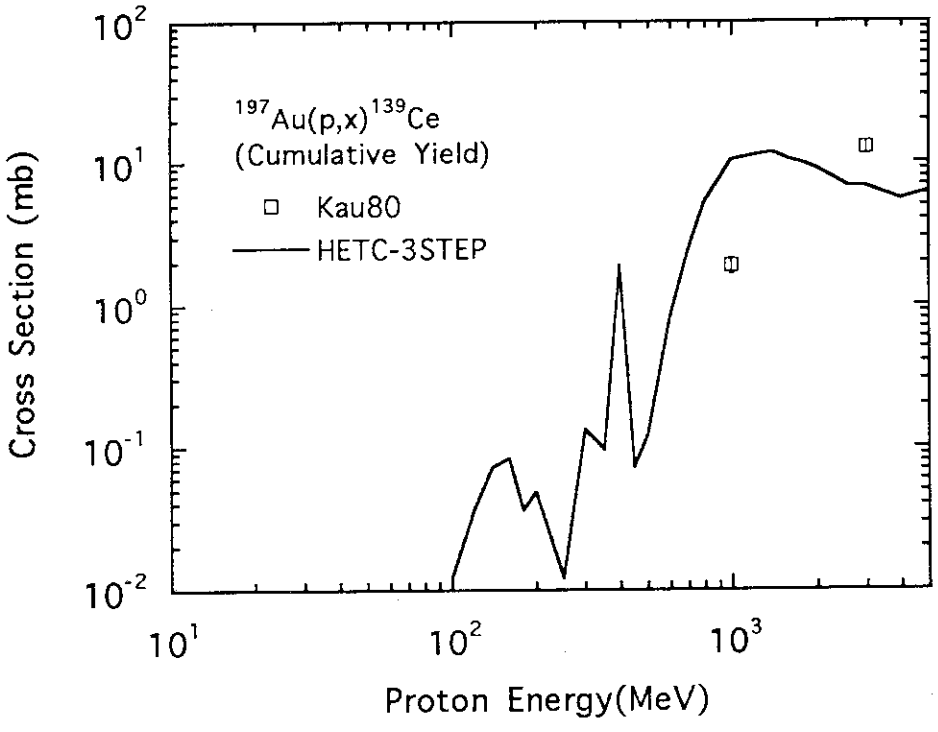

Fig. 88 Cumulative cross section of the ^{197}Au(p, x)^{139}Ce reaction. The notes to the marks and line are the same as for Fig. 23.

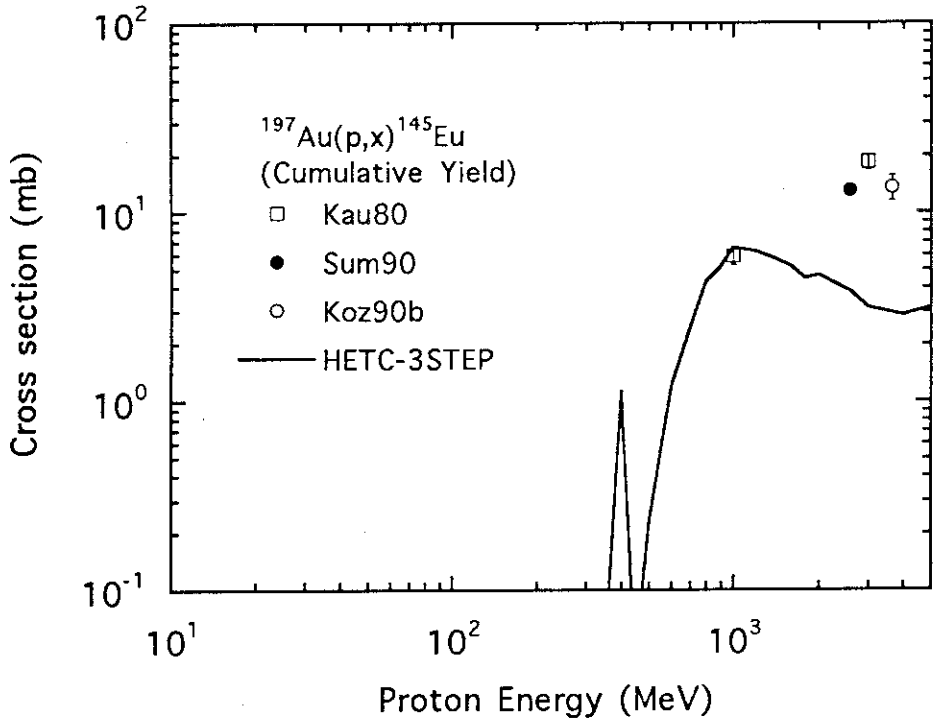

Fig. 89 Cumulative cross section of the ^{197}Au(p, x)^{145}Eu reaction. The notes to the marks and line are the same as for Fig. 23.

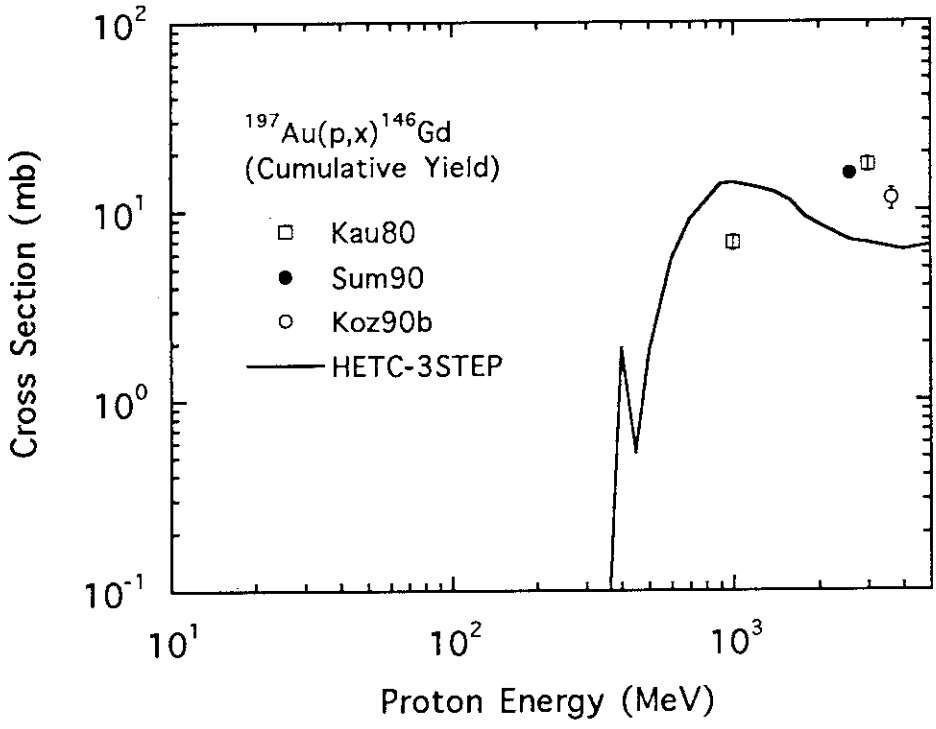

Fig. 90 Cumulative cross section of the ^{197}Au(p, x)^{146}Gd reaction. The notes to the marks and line are the same as for Fig. 23.

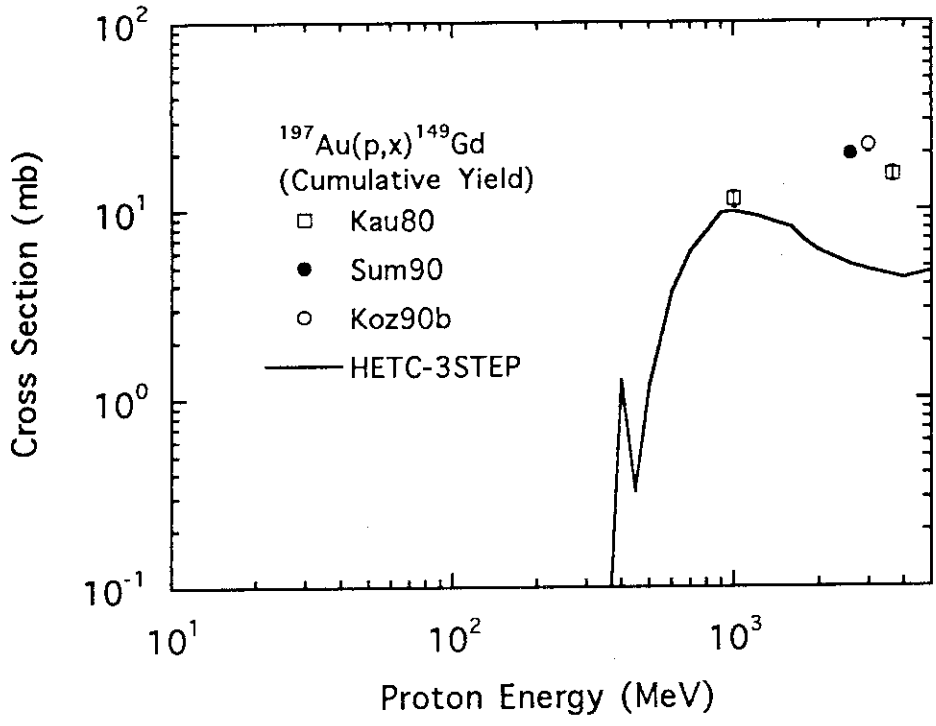

Fig. 91 Cumulative cross section of the ^{197}Au(p, x)^{149}Gd reaction. The notes to the marks and line are the same as for Fig. 23.

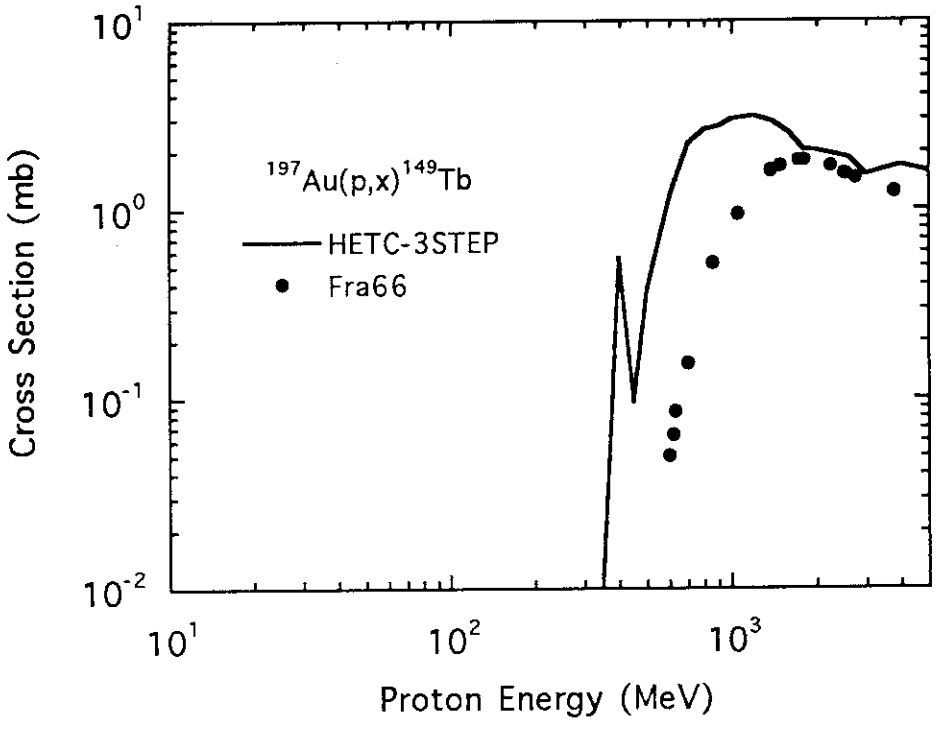

Fig. 92 Cross section of the ^{197}Au(p, x)^{149}Tb reaction. The notes to the marks and line are the same as for Fig. 23.

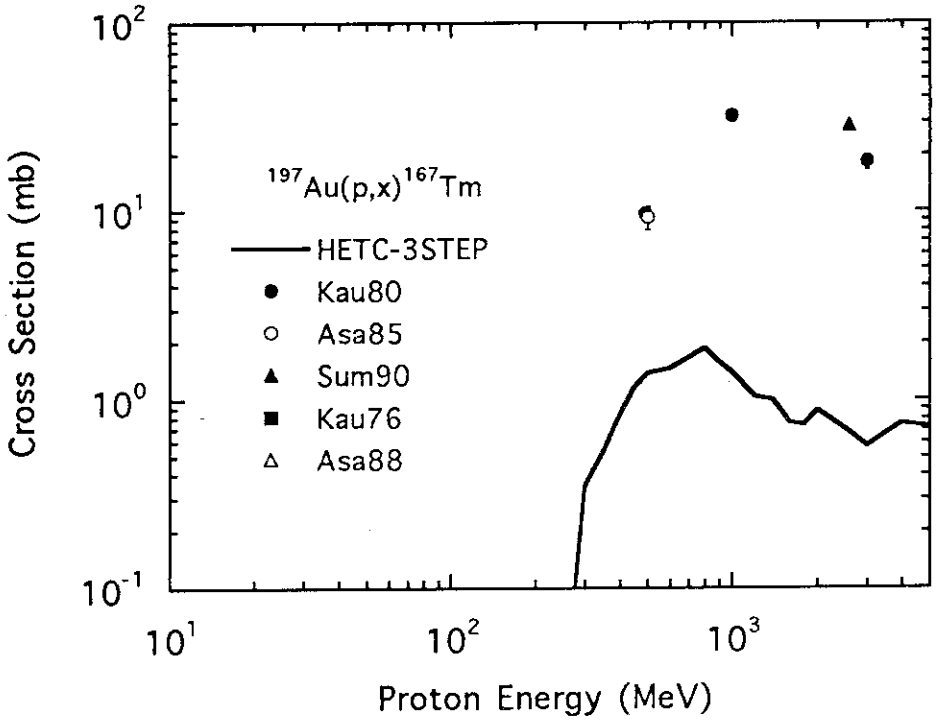

Fig. 93 Cumulative cross section of the ^{197}Au(p, x)^{167}Tm reaction. The notes to the marks and line are the same as for Fig. 23.

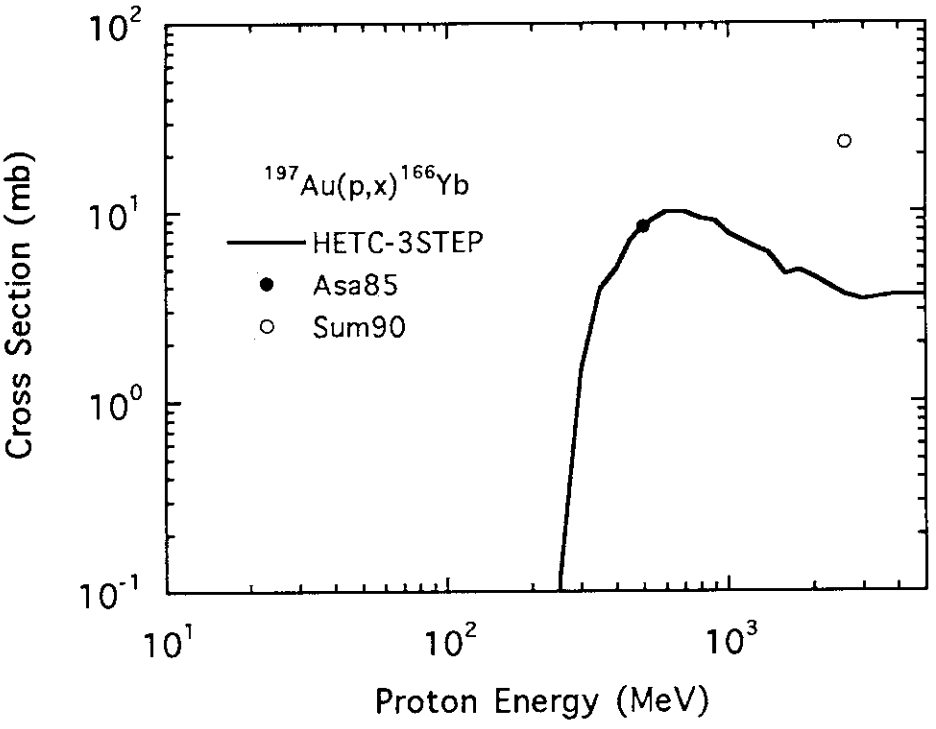

Fig. 94 Cumulative cross section of the ^{197}Au(p, x)^{166}Yb reaction. The notes to the marks and line are the same as for Fig. 23.

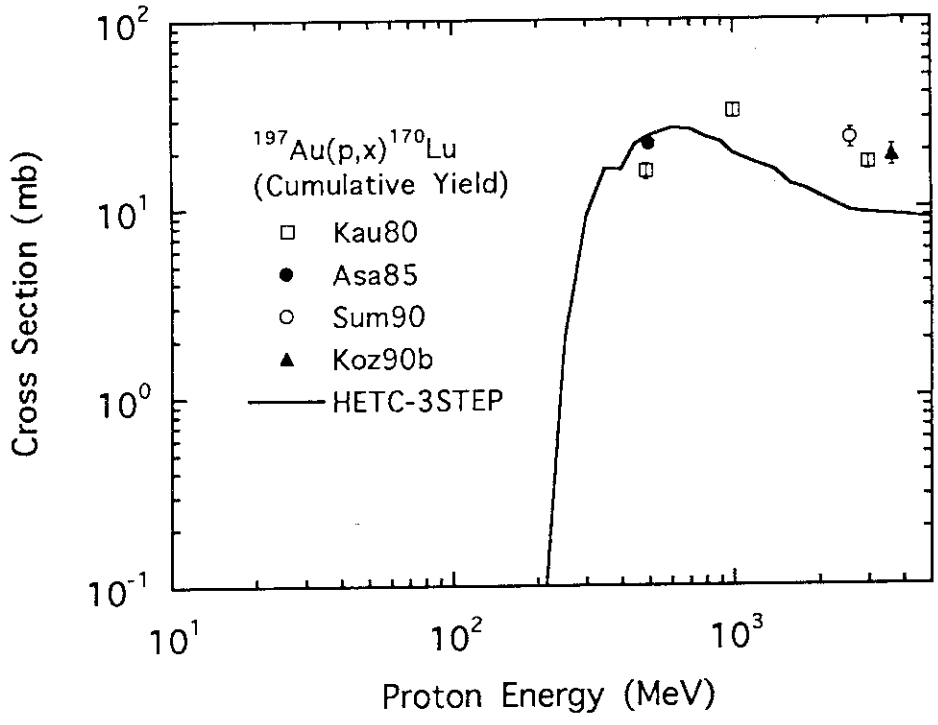

Fig. 95 Cumulative cross section of the ^{197}Au(p, x)^{170}Lu reaction. The notes to the marks and line are the same as for Fig. 23.

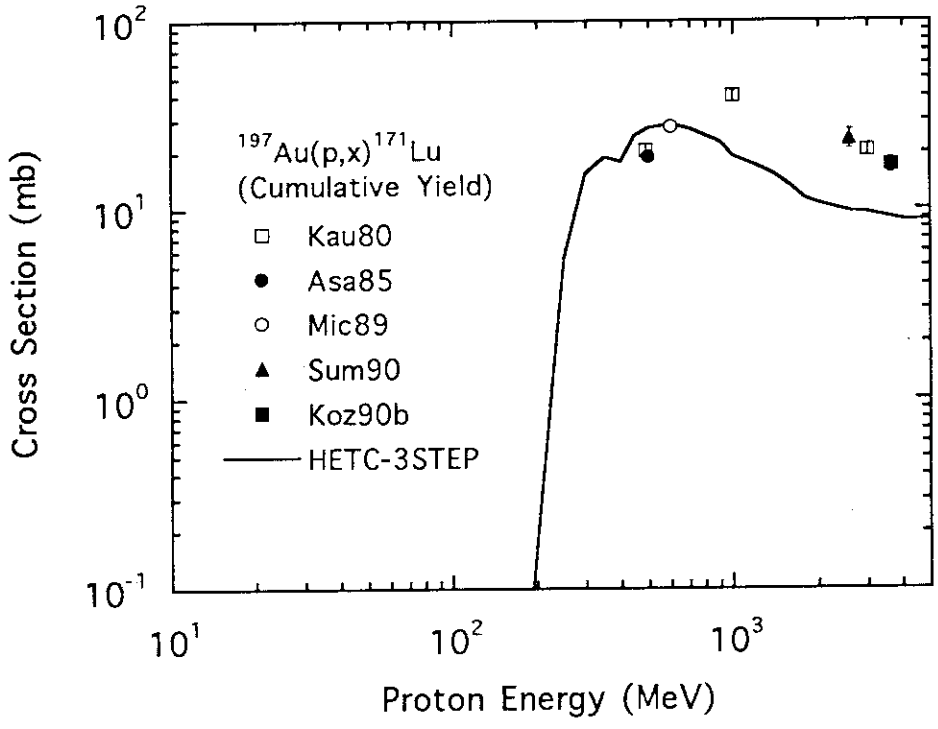

Fig. 96 Cumulative cross section of the ^{197}Au(p, x)^{171}Lu reaction. The notes to the marks and line are the same as for Fig. 23.

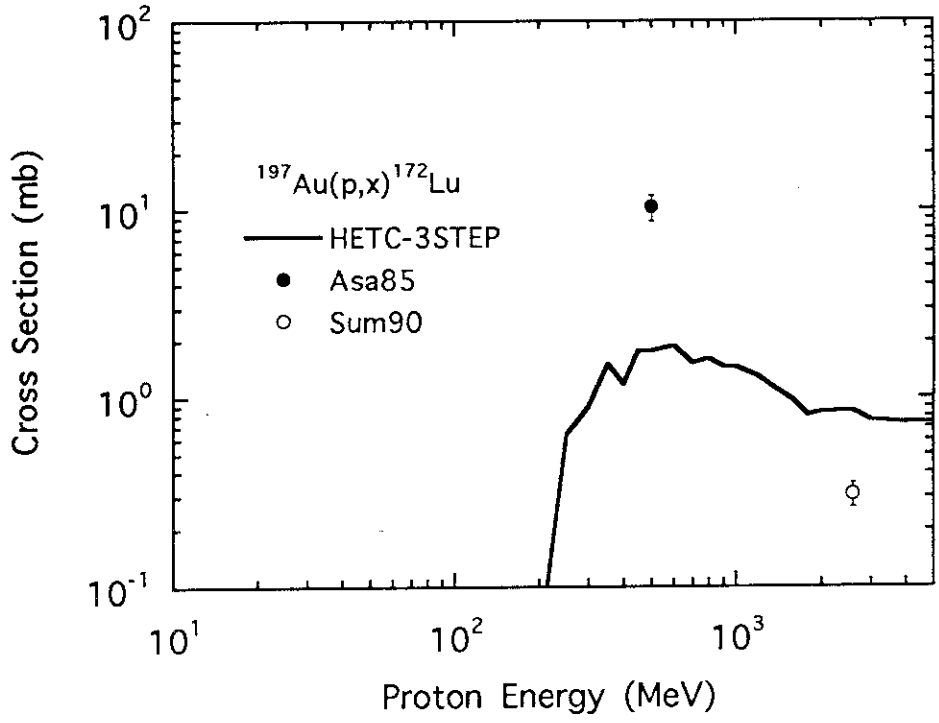

Fig. 97 Cumulative cross section of the ^{197}Au(p, x)^{172}Lu reaction. The notes to the marks and line are the same as for Fig. 23.

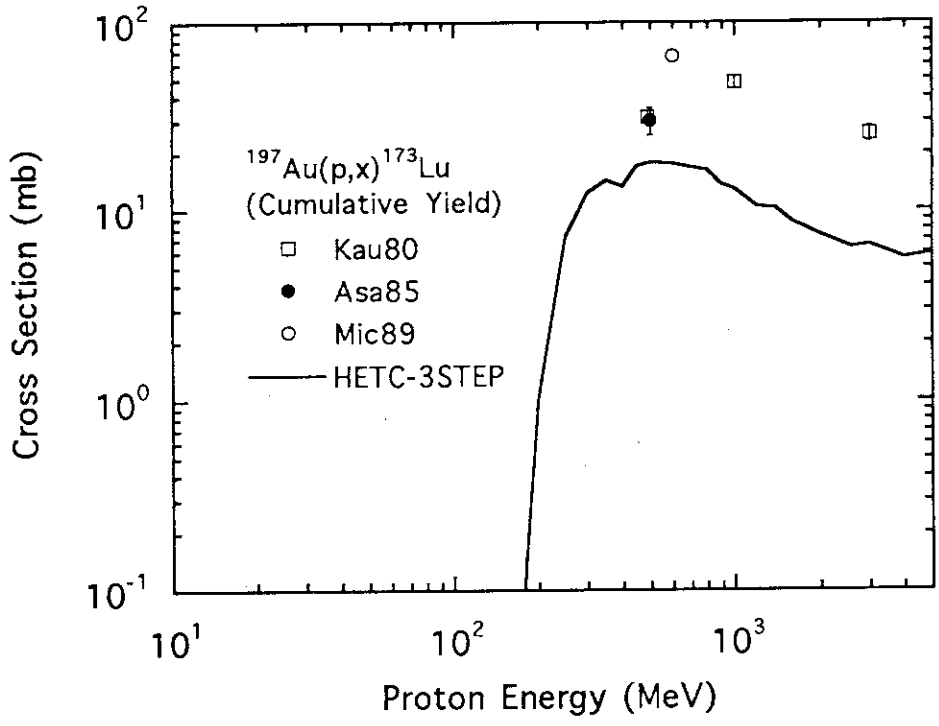

Fig. 98 Cumulative cross section of the ^{197}Au(p, x)^{173}Lu reaction. The notes to the marks and line are the same as for Fig. 23.

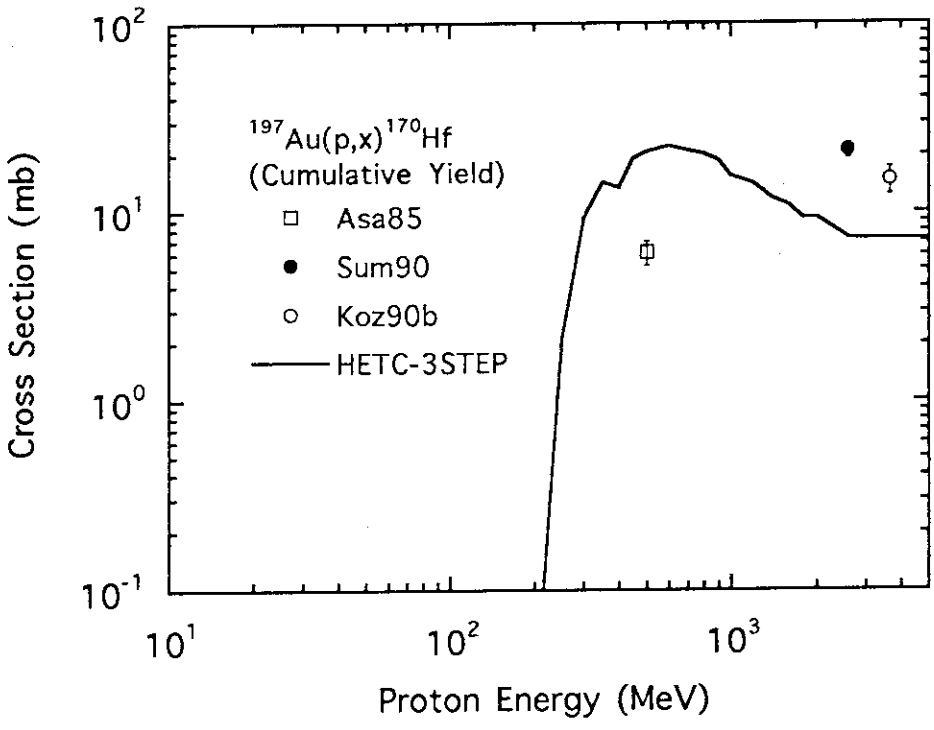

Fig. 99 Cumulative cross section of the ^{197}Au(p, x)^{170}Hf reaction. The notes to the marks and line are the same as for Fig. 23.

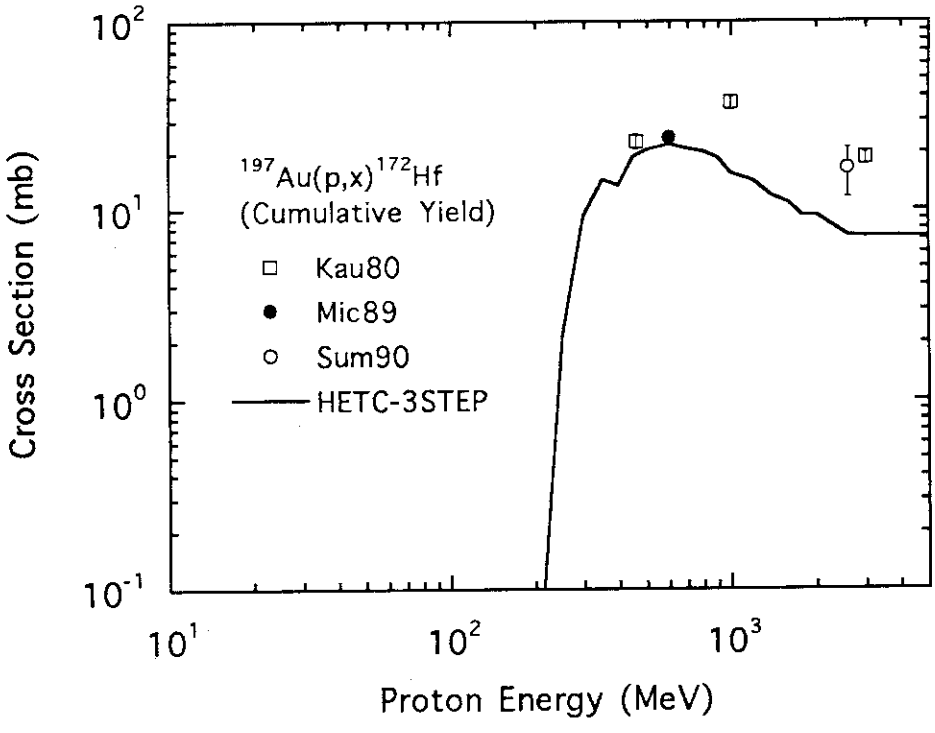

Fig. 100 Cumulative cross section of the ^{197}Au(p, x)^{172}Hf reaction. The notes to the marks and line are the same as for Fig. 23.

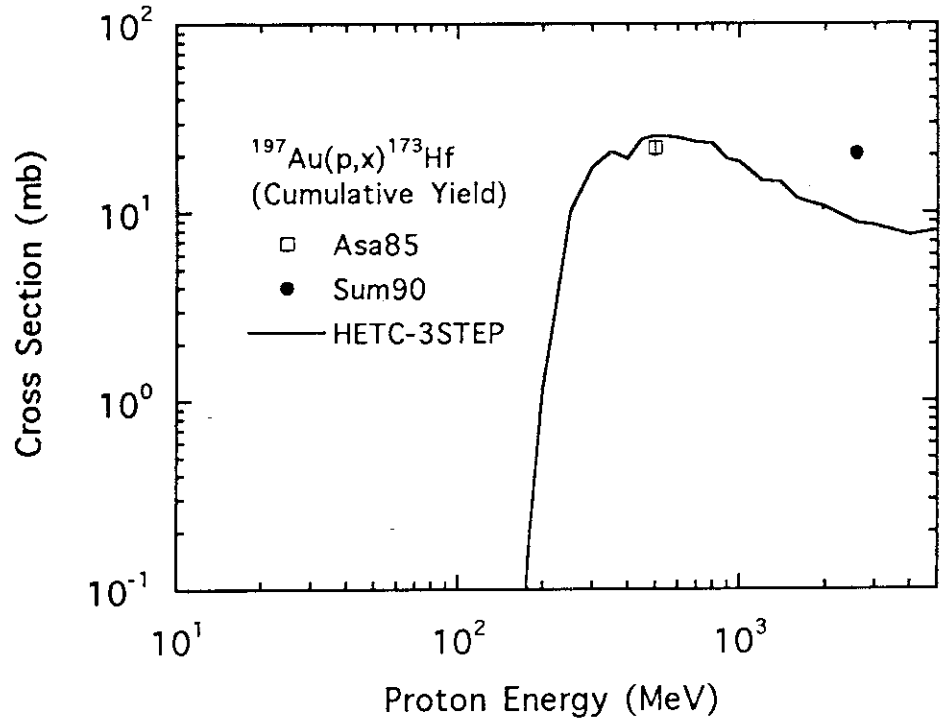

Fig. 101 Cumulative cross section of the ^{197}Au(p, x)^{173}Hf reaction. The notes to the marks and line are the same as for Fig. 23.

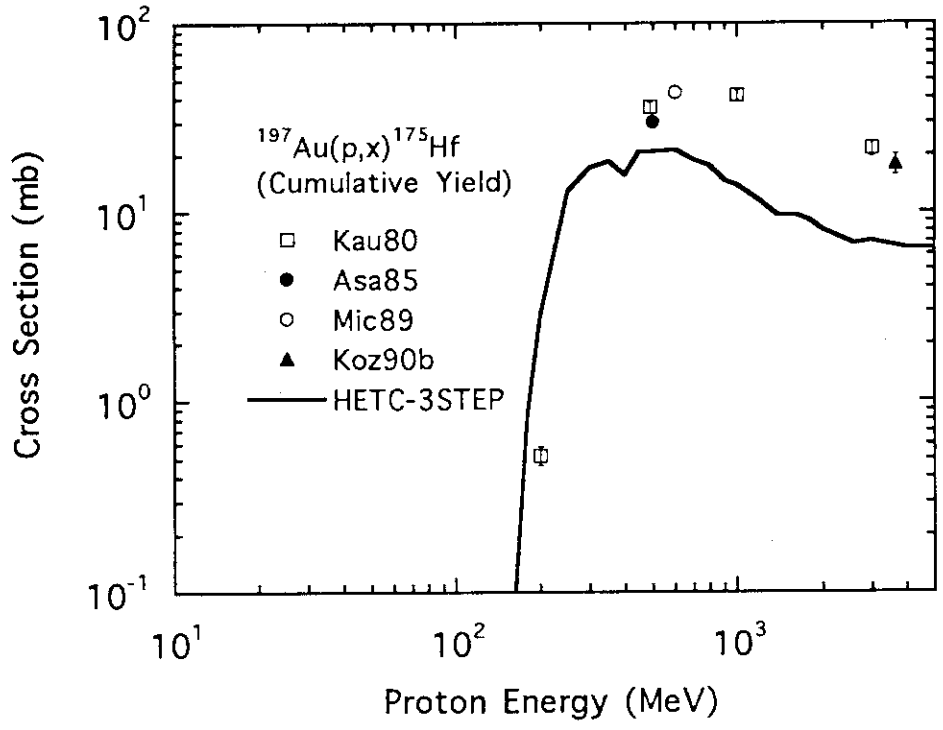

Fig. 102 Cumulative cross section of the ^{197}Au(p, x)^{175}Hf reaction. The notes to the marks and line are the same as for Fig. 23.

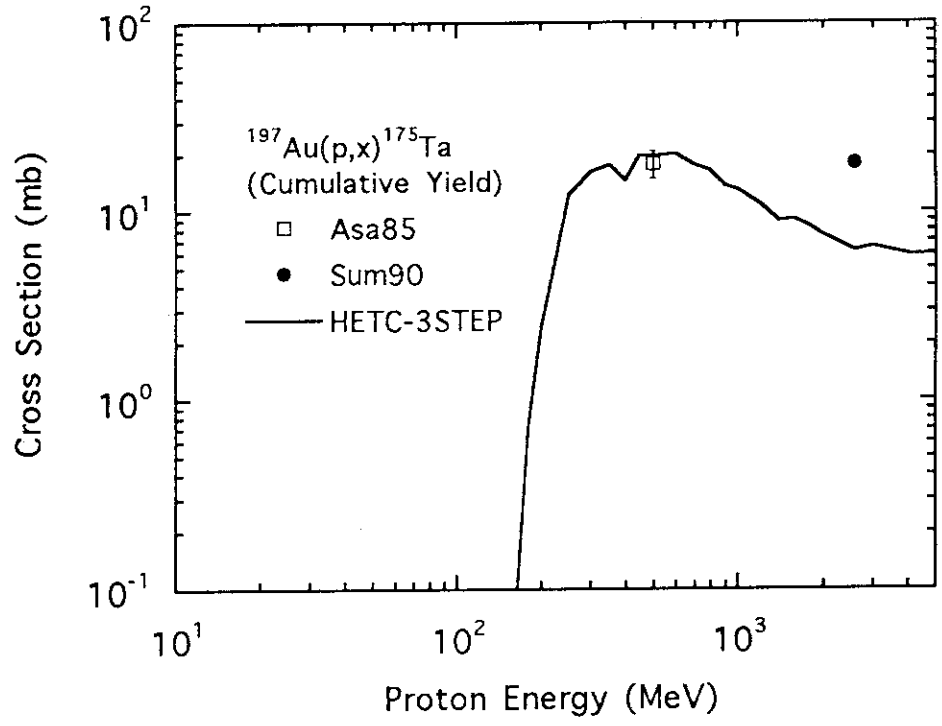

Fig. 103 Cumulative cross section of the ^{197}Au(p, x)^{175}Ta reaction. The notes to the marks and line are the same as for Fig. 23.

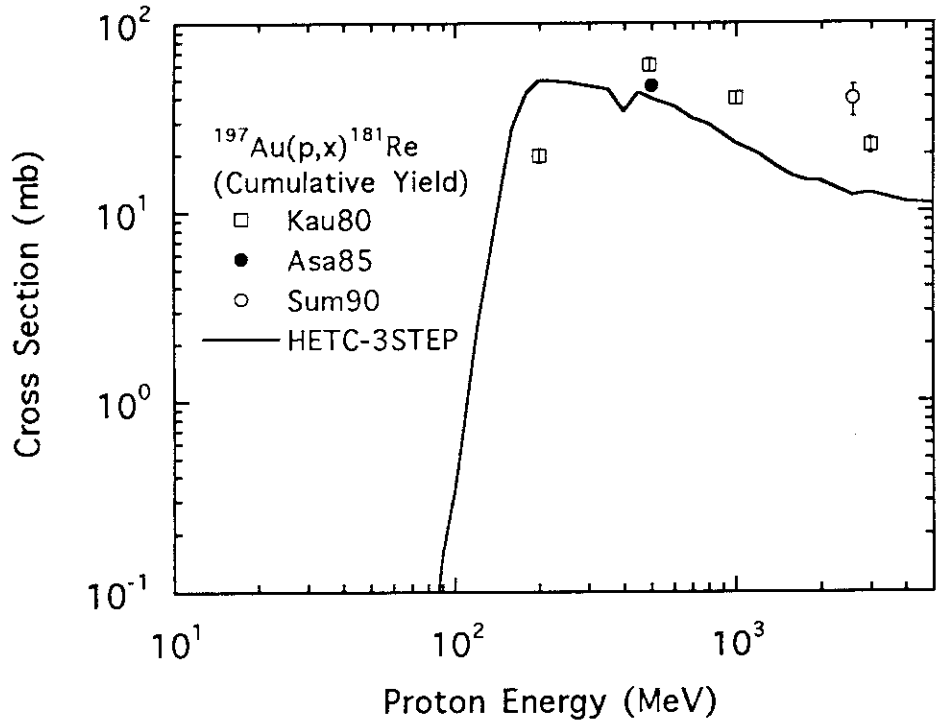

Fig. 104 Cumulative cross section of the ^{197}Au(p, x)^{181}Re reaction. The notes to the marks and line are the same as for Fig. 23.

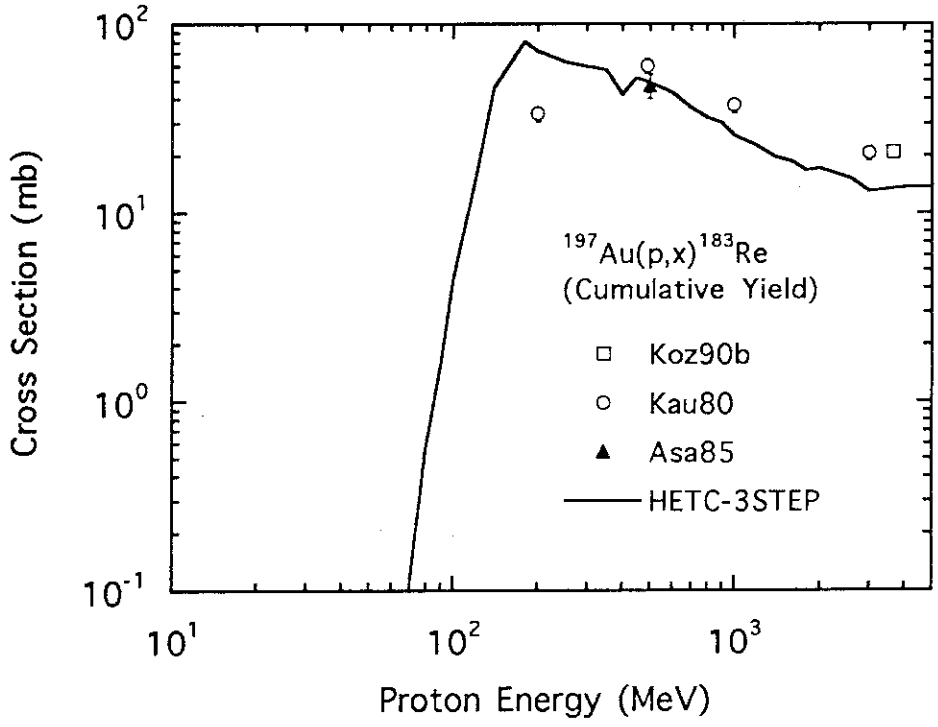

Fig. 105 Cumulative cross section of the $^{197}Au(p, x)^{183}Re$ reaction. The notes to the marks and line are the same as for Fig. 23.

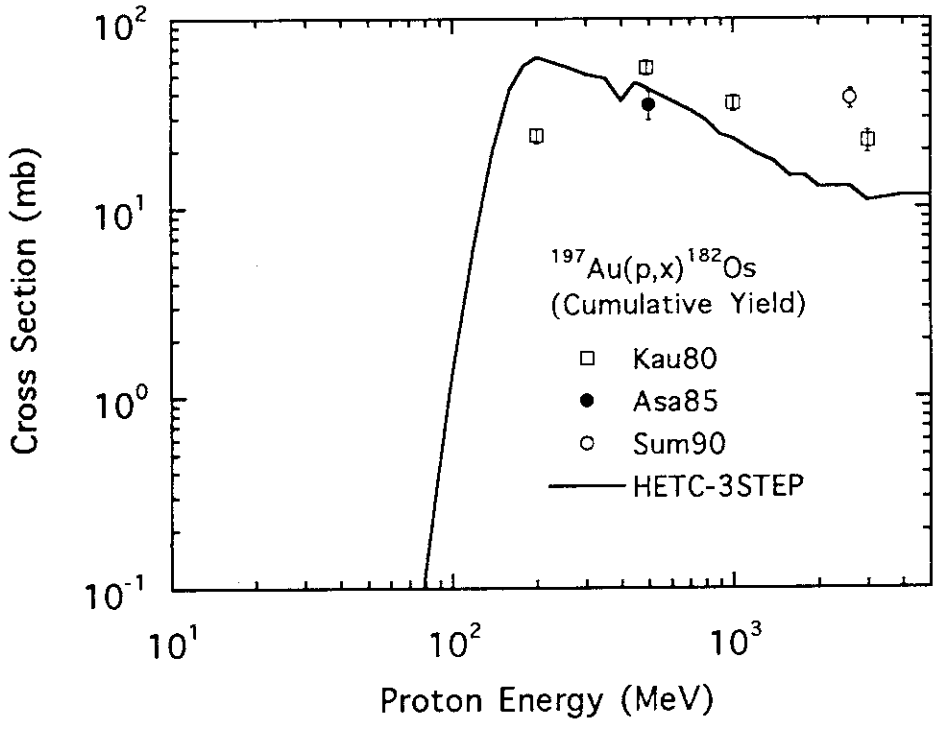

Fig. 106 Cumulative cross section of the $^{197}Au(p, x)^{182}Os$ reaction. The notes to the marks and line are the same as for Fig. 23.

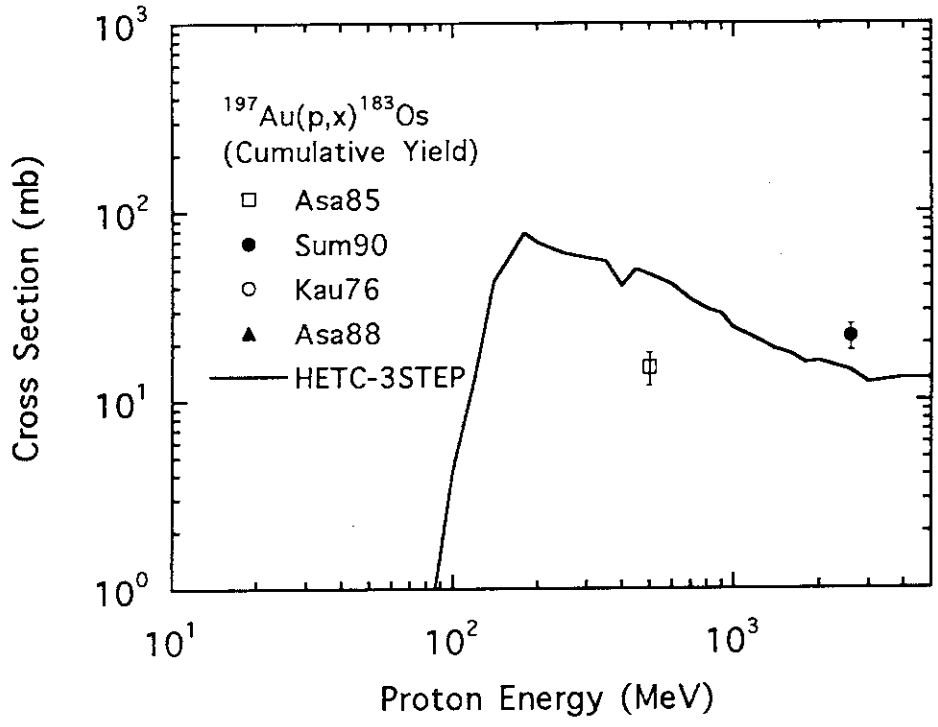

Fig. 107 Cumulative cross section of the ^{197}Au(p, x)^{183}Os reaction. The notes to the marks and line are the same as for Fig. 23.

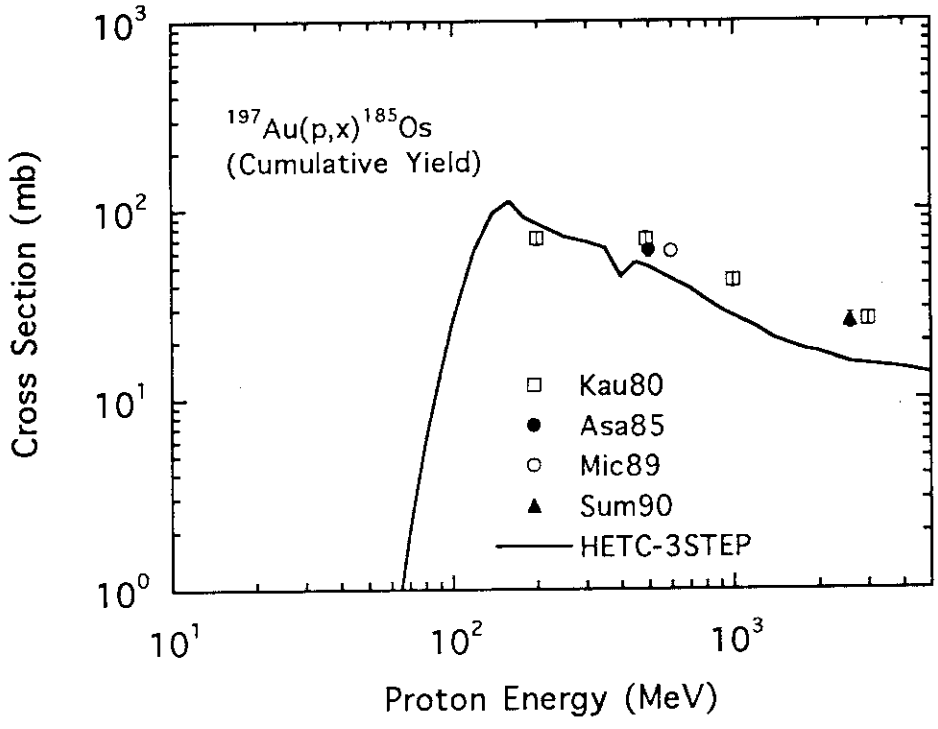

Fig. 108 Cumulative cross section of the ^{197}Au(p, x)^{185}Os reaction. The notes to the marks and line are the same as for Fig. 23.

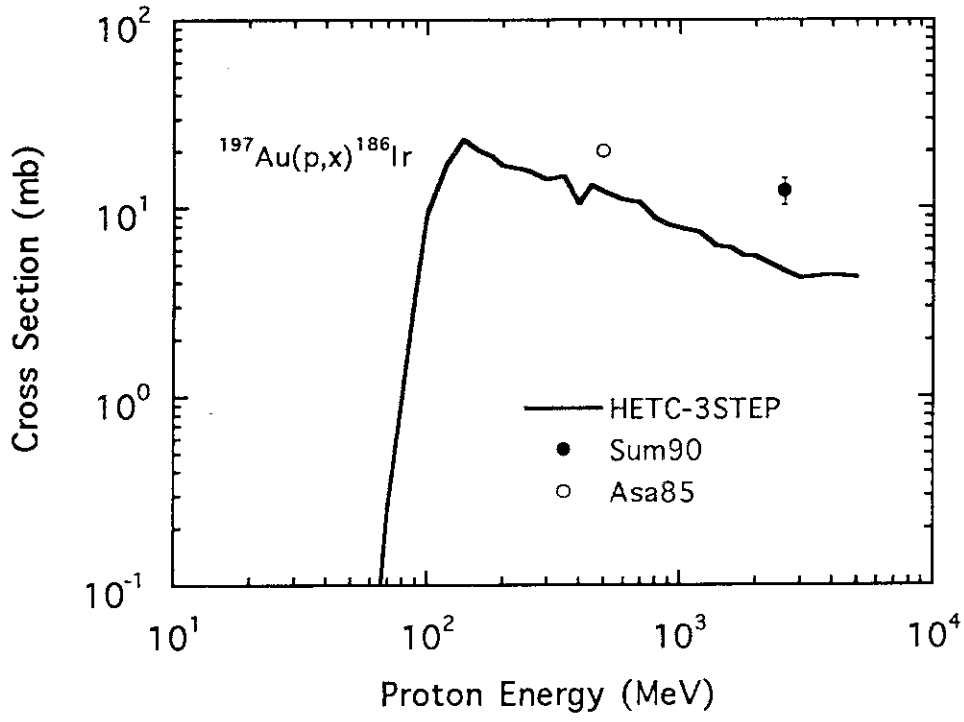

Fig. 109 Cumulative cross section of the ^{197}Au(p, x)^{186}Ir reaction. The notes to the marks and line are the same as for Fig. 23.

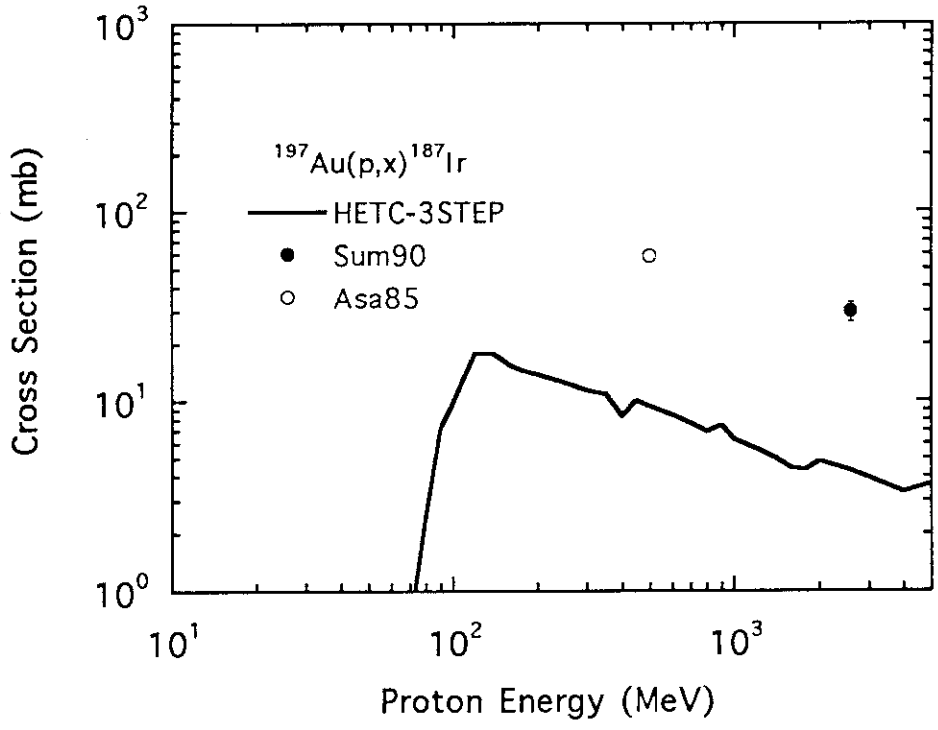

Fig. 110 Cumulative cross section of the ^{197}Au(p, x)^{187}Ir reaction. The notes to the marks and line are the same as for Fig. 23.

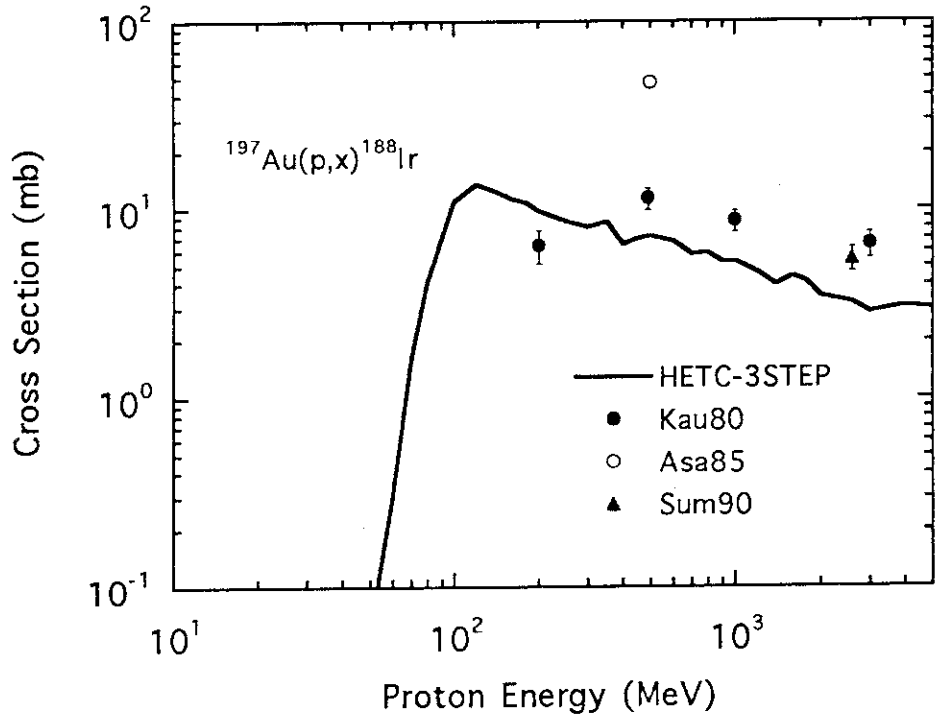

Fig. 111 Cross section of the ^{197}Au(p, x)^{188}Ir reaction. The notes to the marks and line are the same as for Fig. 23.

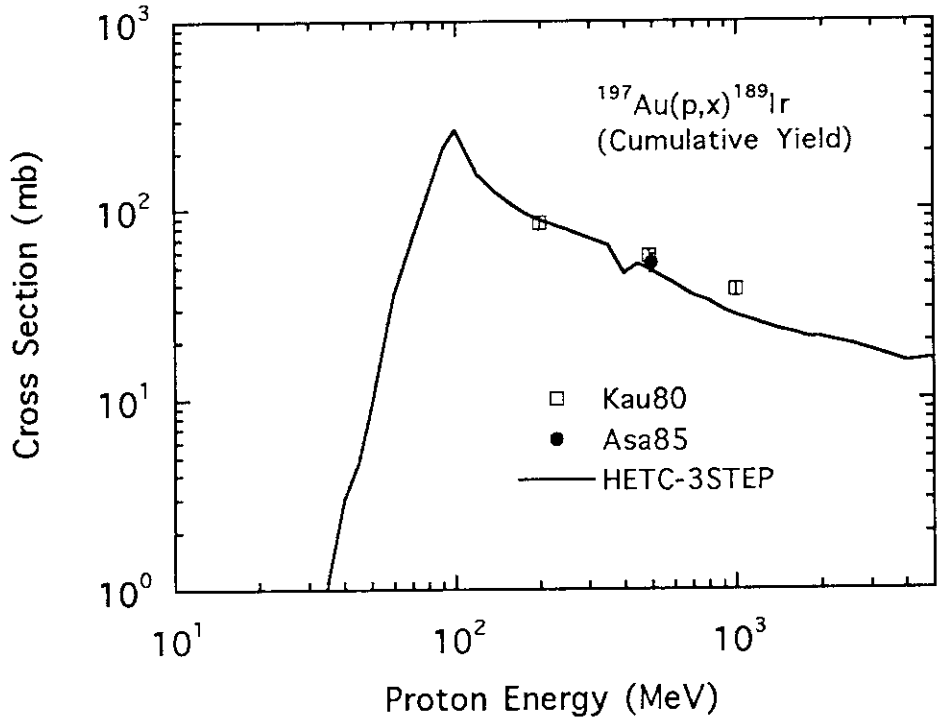

Fig. 112 Cumulative cross section of the ^{197}Au(p, x)^{189}Ir reaction. The notes to the marks and line are the same as for Fig. 23.

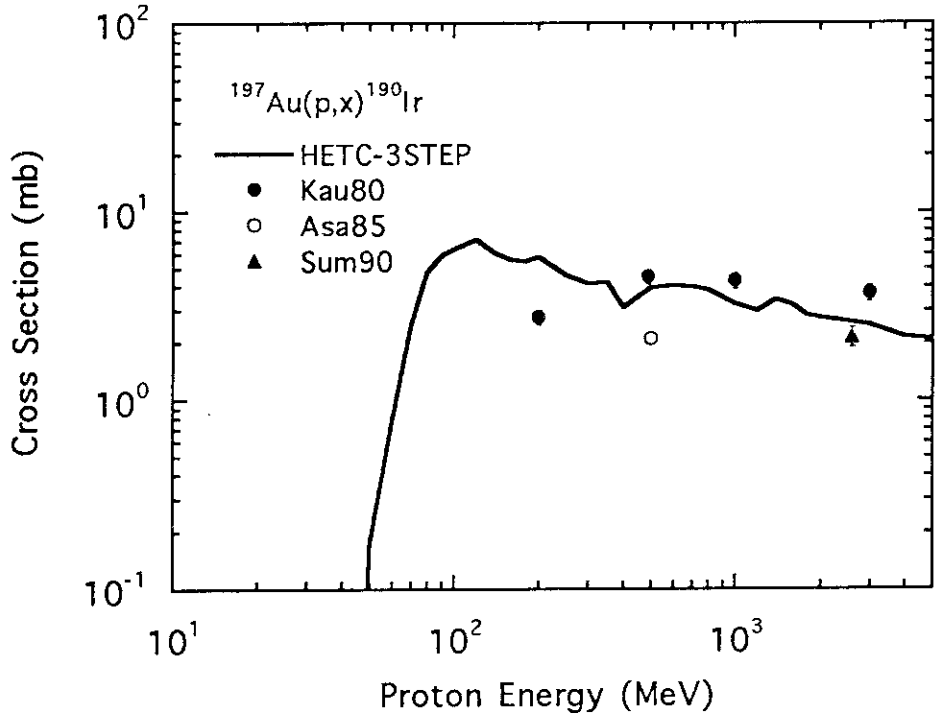

Fig. 113 Cross section of the ^{197}Au(p, x)^{190}Ir reaction. The notes to the marks and line are the same as for Fig. 23.

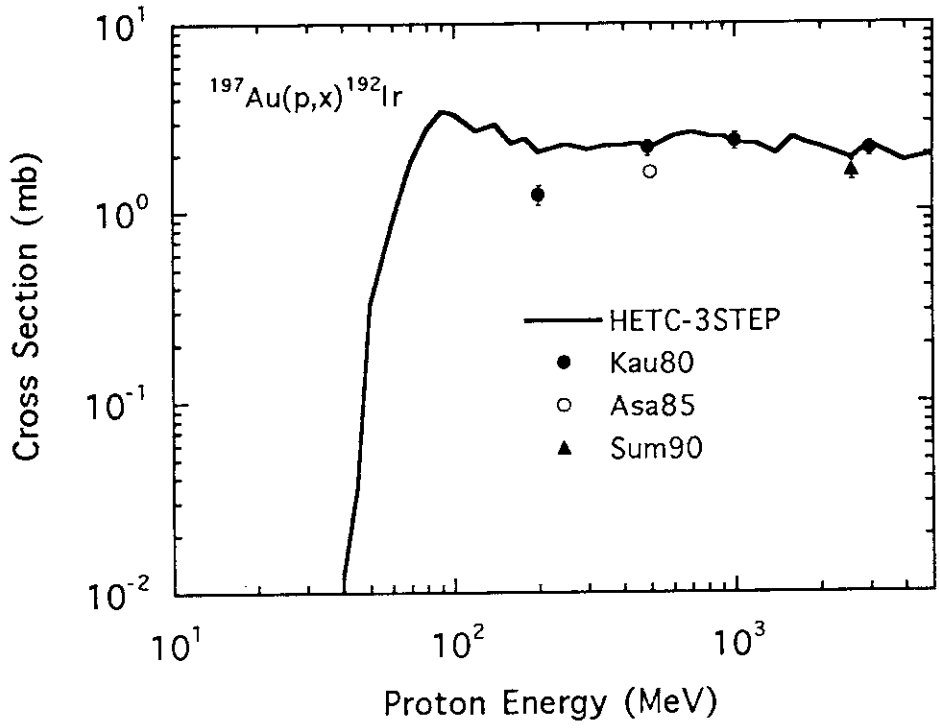

Fig. 114 Cross section of the ^{197}Au(p, x)^{192}Ir reaction. The notes to the marks and line are the same as for Fig. 23.

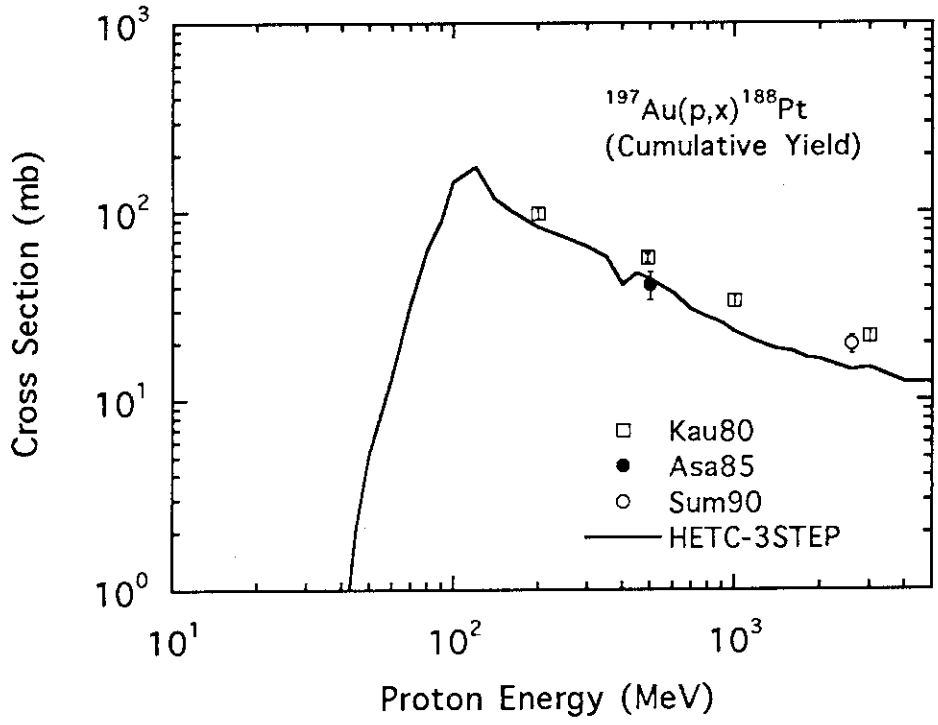

Fig. 115 Cumulative cross section of the ^{197}Au(p, x)^{188}Pt reaction. The notes to the marks and line are the same as for Fig. 23.

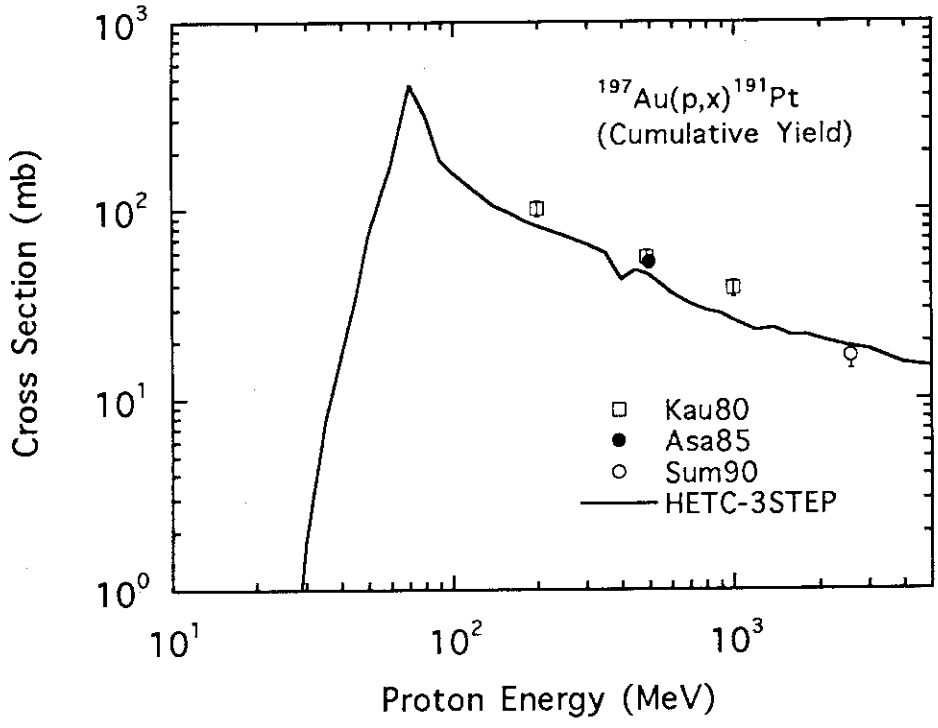

Fig. 116 Cumulative cross section of the ^{197}Au(p, x)^{191}Pt reaction. The notes to the marks and line are the same as for Fig. 23.

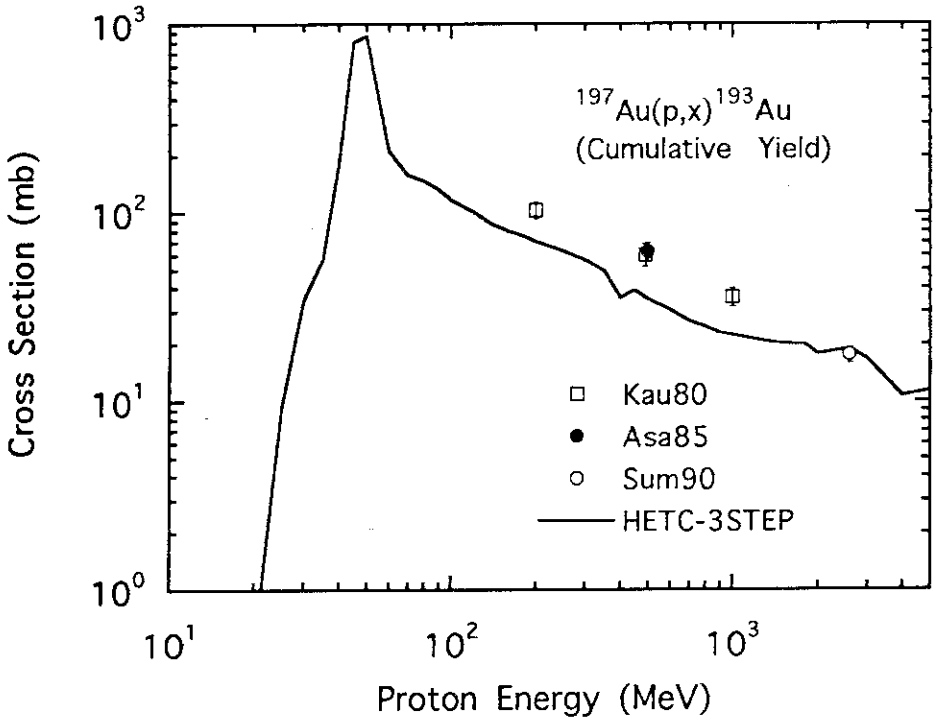

Fig. 117 Cumulative cross section of the ^{197}Au(p, x)^{193}Au reaction. The notes to the marks and line are the same as for Fig. 23.

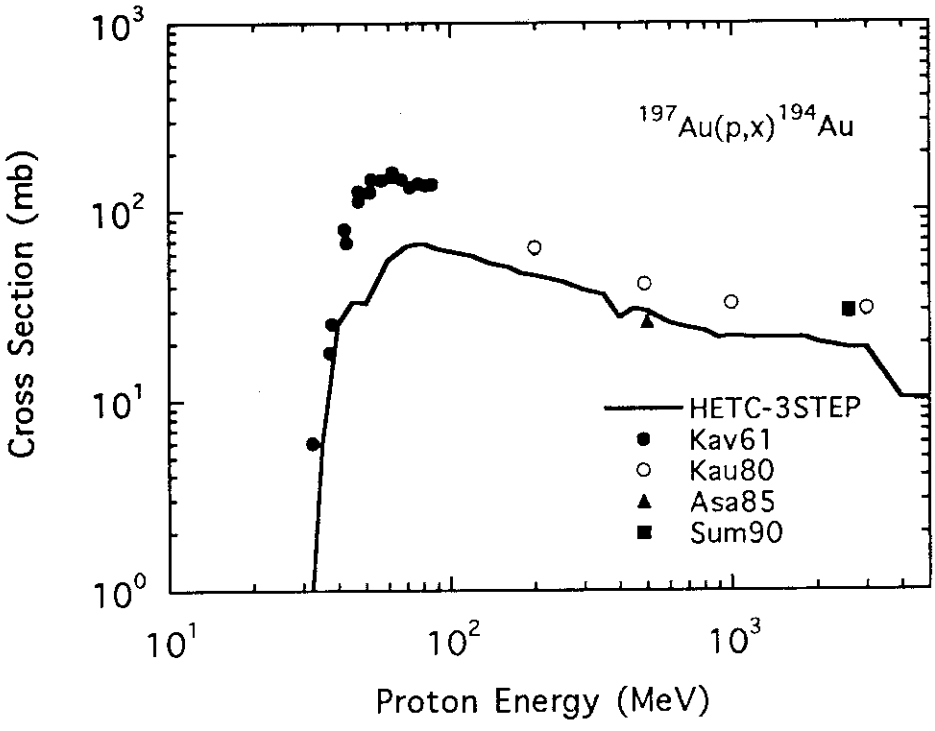

Fig. 118 Cross section of the ^{197}Au(p, x)^{194}Au reaction. The notes to the marks and line are the same as for Fig. 23.

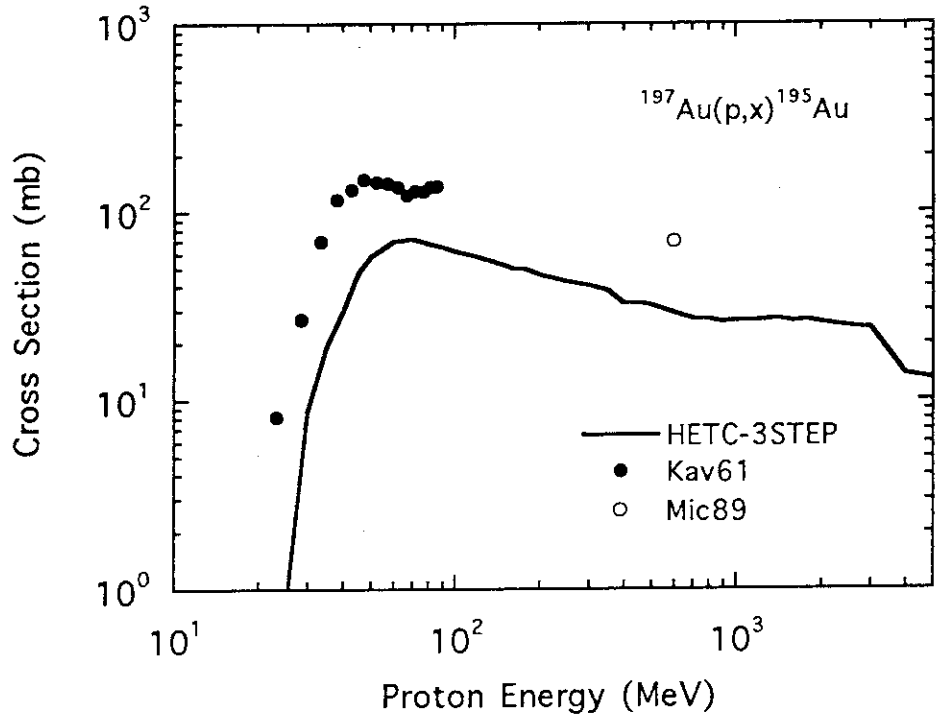

Fig. 119 Cross section of the ^{197}Au(p, x)^{195}Au reaction. The notes to the marks and line are the same as for Fig. 23.

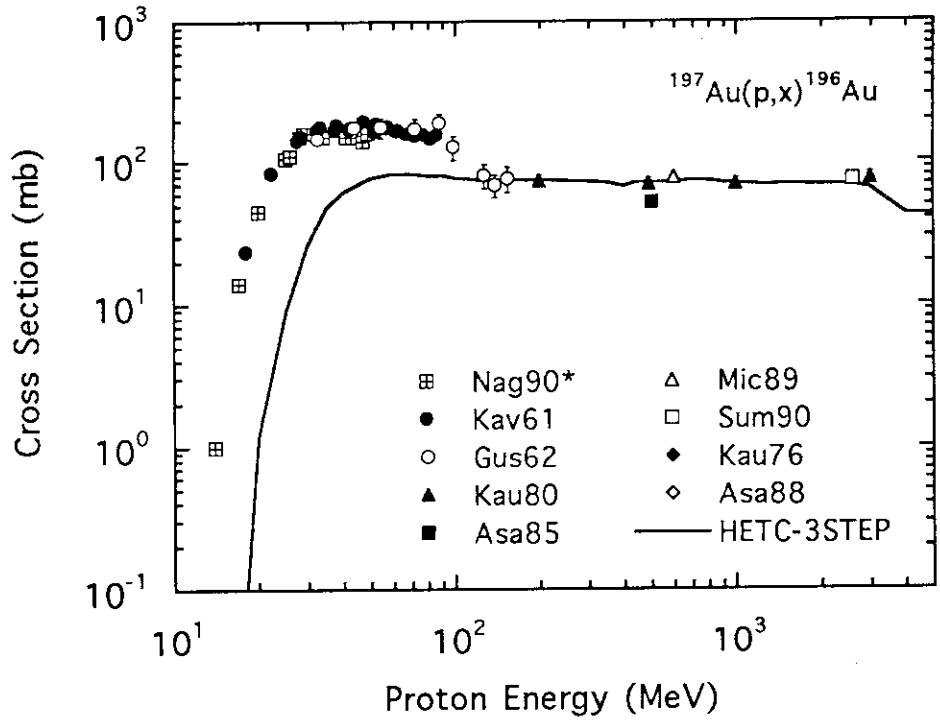

Fig. 120 Cross section of the ^{197}Au(p, x)^{196}Au reaction. The notes to the marks and line are the same as for Fig. 23.

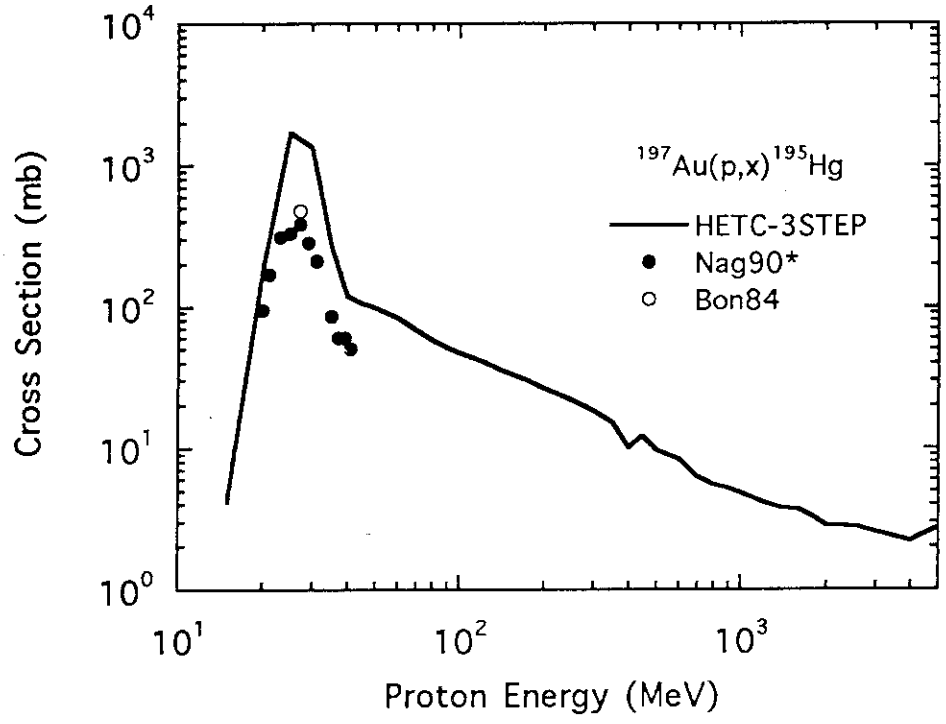

Fig. 121 Cross section of the ^{197}Au(p, x)^{195}Hg reaction. The notes to the marks and line are the same as for Fig. 23.

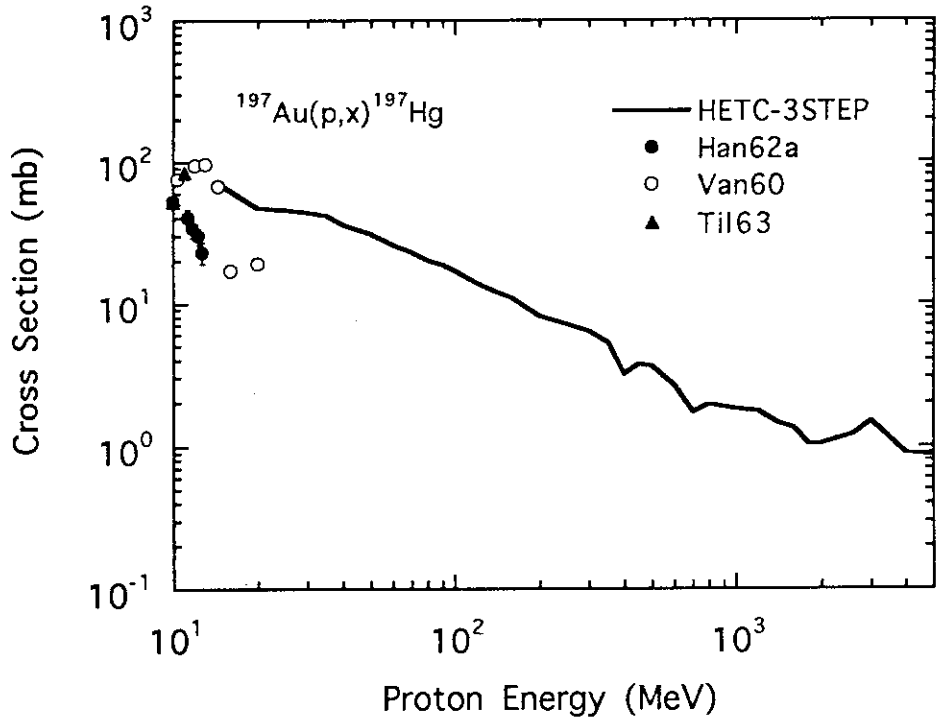

Fig. 122 Cross section of the ^{197}Au(p, x)^{197}Hg reaction. The notes to the marks and line are the same as for Fig. 23.